Prognostic Ozone for ICON: Enabling UV Forecasts

Zur Erlangung des akademischen Grades eines

Doktors der Naturwissenschaften

von der KIT-Fakultät für Physik des
Karlsruher Instituts für Technologie (KIT)

genehmigte

Dissertation

von

Valentin Hanft

Tag der mündlichen Prüfung: 06.02.2026
1. Referent: Prof. Dr. Peter Braesicke
2. Korreferent: PD Dr. Michael Höpfner

Abstract

Solar ultraviolet (UV) radiation at Earth's surface poses a well-documented risk for human health. The World Health Organization has defined the UV-Index to quantify the amount of UV radiation as integers in a range of 1 to 10+. It depends on a variety of quantities, including the overhead ozone column. The UV-Index is typically forecasted on the time scale of days to warn the public of health risks. In Germany this is done by the Deutscher Wetterdienst (DWD) who use their weather model ICON (ICOsahedral Nonhydrostatic model) in combination with external datasets for ozone forecasts and UV radiation calculations. This thesis presents a novel setup to make the UV-Index forecast self-consistent by using ozone calculations via the LINearized OZone (LINOZ) scheme and UV radiation calculations via the Cloud-J scheme from within ICON and the coupled Aerosols and Reactive Trace gases (ART) module. The result is a setup that can forecast ozone and UV-Index fields. For a time frame of January to April 2025, it shows a precision of ±1 units of UV-Index for 94.9% of the data points in comparison to ground measurement stations. Ozone columns stay within 5% agreement for a time period of four months in the northern hemisphere in comparison to Ozonewatch satellite data. The solar zenith angle is found to be the quantity that introduces most variability (9.2 ± 1.9) on the UV-Index. Aerosol optical depth (4.1 ± 2.9), cloud cover (4.7 ± 2.1) and overhead ozone (4.9 ± 1.9) introduce smaller variabilities while the effect of surface albedo (3.3 ± 2.9) and altitude (2.5 ± 2.5) is even less pronounced. A comparison of the new setup to the operational forecast by the DWD agrees within ±2 units of UV-Index for almost all data points with the exception of mountainous areas, where larger differences occur.

Zusammenfassung

Ultraviolette (UV) Strahlung der Sonne stellt ein gut belegtes Risiko für die Gesundheit von Menschen dar. Um die Gefahr zu quantifizieren hat die Weltgesundheitsorganisation (WHO) den UV-Index definiert der die UV-Strahlung als ganzzahlige Werte, typischerweise zwischen 1 und 10, darstellt. Der UV-Index hängt von mehreren Einflussgrößen ab, unter Anderem von der atmosphärischen Ozonsäule. Er wird auf einer Zeitskala von Tagen vorhergesagt, um die Öffentlichkeit auf Gesundheitsrisiken durch UV-Strahlung hinzuweisen. Diese Aufgabe übernimmt in Deutschland der Deutsche Wetterdienst (DWD), der dafür sein Wettermodell ICON (ICOsahedral Nonhydrostatic model) in Kombination mit externen Ozonvorhersagen und UV-Strahlungsberechnungen verwendet. In dieser Arbeit wird eine neue Berechnungsmethode vorgestellt, die Ozonvorhersagen mit dem LINearisierten OZonprogramm (LINOZ) und UV-Strahlungsberechnungen mit dem Programm Cloud-J verwendet, um UV-Indizes selbstkonsistenter zu berechnen. Beide Programme sind in dem "Aerosols and Reactive Trace gases"-Modul (ART) enthalten, das Teil von ICON ist. Das Ergebnis ist ein Modellaufbau, der für einen Testzeitraum von Januar bis April 2025 den UV-Index im Vergleich zu Bodenmessstationen mit einer Genauigkeit von ±1 UV-Indexeinheiten für 94.9% der Daten vorhersagen kann. Ozonsäulen können im Vergleich zu Ozonewatch-Satellitendaten auf der nördlichen Hemisphäre innerhalb einer 5%-Übereinstimmung für einen Vorhersagezeitraum von vier Monaten berechnet werden. Der Sonnenzenitwinkel ist dabei die Einflussgröße, die die größte Variabilität auf den UV-Index verursacht (9.2 ± 1.9). Die aerosoloptische Dicke (4.1 ± 2.9), Bewölkung (4.7 ± 2.1) und Ozonsäule (4.9 ± 1.9) haben einen schwächeren Effekt auf den UV-Index, noch

geringer ist der Effekt von Oberflächenalbedo (3.3 ± 2.9) und Höhe (2.5 ± 2.5). Ein Vergleich zu der operationellen DWD-Vorhersage des UV-Index zeigt eine Übereinstimmung von ±2 UV-Indexeinheiten für fast alle Datenpunkte mit der Ausnahme von Bergregionen, in denen auch höhere Abweichungen vorkommen.

Contents

List of Figures

List of Tables

1 Introduction

Ultraviolet (UV) radiation from the sun reaching Earth's surface is the main cause for cutaneous melanoma, a type of skin cancer with a reported mortality rate of 26.8% (Sadeq et al. 2023). 75.7% of all globally reported melanoma cases were attributed to UV radiation in 2012, representing 1.2% of all diagnosed cases of cancer worldwide (Arnold et al. 2018). 87% of those global cases of cutaneous melanoma occurred in Europe, Northern America and Oceania (Arnold et al. 2018). In the United Kingdom, 3.5% of all new cases of cancer among humans were attributed to excess solar radiation in the year 2010 (Parkin, Mesher, and Sasieni 2011).

In addition to that, UV radiation also has been found to cause eye cataracts (Taylor et al. 1988), and the World Health Organization (WHO) estimates that 10% of cases of blindness due to cataracts are caused by UV radiation exposure (*WHO: Ultraviolet radiation* 2025). These numbers demonstrate a clear need to understand and to act on the topic of UV radiation exposure and its quantification.

To mitigate the hazards of UV radiation exposure, the World Meteorological Organization (WMO) conducted a meeting together with the WHO in 1997 to standardize an international UV-Index (UVI) and to disseminate it to the public (*Report of the WMO-WHO Meeting of Experts on Standardization of UV Indices and their Dissemination to the Public*). The UVI is a dimensionless integer number on a scale from 0 to 10+ (the scale is not limited to higher values) that indicates the harmfulness of solar UV radiation to human health. Low values mean a lower risk of skin damage, higher values indicate a higher risk of skin or

eye damage. A practical guide was released by WHO to summarize information on the UVI (Rehfuess 2002).

For Germany, Deutscher Wetterdienst (DWD) is fulfilling the responsibility of forecasting the UVI (Staiger and Koepke 2005) and to communicate it to the public via its web page (*Wetter und Klima - Deutscher Wetterdienst - Leistungen - UV-Gefahrenindex* 2025). DWD combines meteorological output provided by its own weather model ICON (ICOsahedral Nonhydrostatic model) with external ozone data provided by the Royal Netherlands Meteorological Institute and matches the atmospheric state to a precalculated lookup table to create UVI forecast products.

DWD seeks to develop a more self-consistent UVI forecasting method that replaces external ozone and UV radiation calculations with methods that are contained within the ICON modeling framework. Therefore, DWD funded the project "Progonostic Ozone For ICON: Enabling UV-Forecasts (POF)" as part of its program "Extramurale Forschung" in 2020. This project aims to implement fast ozone and UV radiation forecasts in the Aerosols and Reactive Trace Gases (ART) module that is part of ICON and developed at Karlsruher Institut für Technologie (KIT). Here, fast means that the setup has the potential to be used in a continuously operational forecasting setup.

To do so, the LINearized OZone (LINOZ) forecasting scheme contained in ART is configured to provide prognostic ozone fields that are then used in the radiation scheme Cloud-J to calculate UV radiation. This setup is then applied in global and Germany-centered regional simulations and subsequently validated against reference data sets. These include satellite observations, ozone sonde data, ground station measurements and the operational DWD UVI forecast.

To better understand and to quantify the dependence of the UVI on the atmospheric parameters that influence it, this thesis gives an assessment of the UVI dependencies. The parameters that influence the UVI are the solar zenith angle, cloud cover, overhead ozone, albedo, aerosol optical depth and altitude. The dependency of the UVI on these quantities is expressed as the variability the

parameters can introduce on the UVI. This assessment is then used to determine the accuracy of the UVI forecast depending on location or atmospheric state.

First, this thesis gives the physical, chemical and meteorological background underlying atmospheric radiation transport, stratospheric dynamics and processes related to ozone formation and destruction. This is followed by a description of the atmospheric model setup used for the calculation of atmospheric ozone concentrations and UV radiation. After that, the results of this setup are presented and discussed using comparison data sets.

2 Theoretical Background

Atmospheric dynamics, and subsequently weather, is mainly driven by solar radiation and Earth's rotation. While the latter influences the atmosphere via pseudo forces and friction at the surface, the influence of radiation mainly originates from different amounts of irradiance at the Equator and the poles of Earth. This chapter will first treat the topic of radiation transport, then move on to the transport and reactions of chemical species in the stratosphere and the definition of the UV-Index. Finally the concept of transferring these components to a modeling framework will be explained.

Explanations in this chapter follow the books "Fundamentals of Atmospheric Radiation" by Bohren and Clothiaux 2006 and "Physik unserer Umwelt - Die Atmosphäre" by Roedel (2000). If not stated otherwise, information given in this chapter was drawn from these sources.

2.1 The Path of Solar Radiation to Earth's Surface

The stratospheric ozone concentration primarily depends on its interaction with UV radiation. Furthermore, stratospheric ozone has a prominent role in the UV radiation at Earth's surface. This section describes how radiation reaches the atmosphere and how the atmosphere physically interacts with radiation, specifically in the UV spectral regime.

Matter emits radiation at all times. The total radiant power F of a body is described by Stefan-Boltzmann's law:

$$F = \epsilon \cdot \sigma \cdot T^4 \tag{2.1}$$

where ϵ is the emissivity, $\sigma = 5.67 \cdot 10^{-8} \frac{W}{m^2 K^4}$ is Stefan-Boltzmann's constant and T is the temperature. For sufficiently large bodies, $0 < \epsilon \leq 1$. The actual size of ϵ is determined by Kirchhoff's law that states that emissivity (also $0 < \alpha \leq 1$) of a body equals its absorptivity α:

$$\epsilon = \alpha \tag{2.2}$$

where the absorptivity is defined as

$$\frac{\text{absorbed radiance}}{\text{incident radiance}} \tag{2.3}$$

A so-called "blackbody" has $\alpha = 1$, which, in turn, results in $\epsilon = 1$. Therefore, the emissivity can be read as

$$\epsilon = \frac{\text{radiant power of actual body}}{\text{radiant power of a blackbody}} \tag{2.4}$$

The emissivity and absorptivity depend on wavelength, $\epsilon_\lambda = \alpha_\lambda$.

For a blackbody, the radiance depending on wavelength λ and temperature T, $F(\lambda, T)$, follows Planck's function:

$$F(\lambda, T) = \frac{2hc^2}{\lambda^5} \frac{1}{exp(hc/\lambda k_B T) - 1} \tag{2.5}$$

Here, $h = 6.63 \cdot 10^{-34}$ Joule $\cdot s$ is Planck's constant, $k_B = 1.38 \cdot 10^{-23} \frac{\text{J}}{\text{K}}$ is Boltzmann's constant and c is the speed of light. For a nonblack body, this radiance will be multiplied by its emissivity:

$$F(\lambda, T) = \epsilon_\lambda \cdot F(\lambda, T)_{blackbody} \tag{2.6}$$

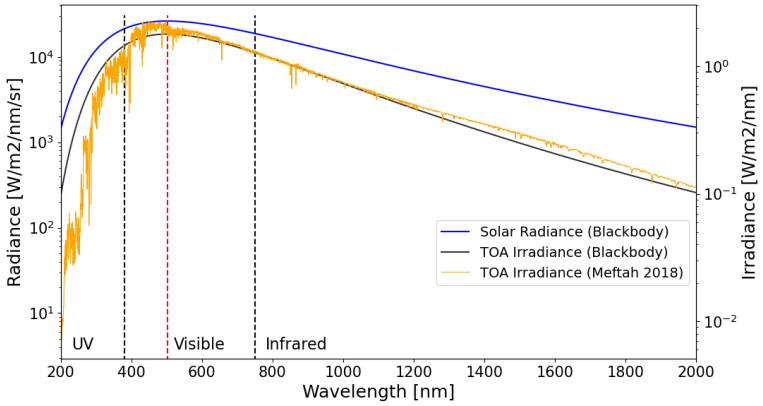

Figure 2.1: Blackbody radiance at the sun's surface (blue), solar blackbody irradiance at top of Earth's Atmosphere (TOA) (black) and measured Solar Spectral Irradiance (SSI) at Top of Atmosphere (orange) on a logarithmic scale. The dashed lines indicate the separation of the spectrum into UV range, visible range and infrared range. The difference between the two idealized blackbody spectra is the switch from radiance to irradiance and the distance between Sun and Earth. When comparing the blackbody TOA spectrum to the measured one, the Frauenhofer absorption lines are visible in addition to the broadband absorption in the UV range due to ionizing particles in Sun's atmosphere. SSI spectrum by Meftah et al. (2018)

When differentiating equation 2.5 for λ and setting it to zero, one can obtain Wien's displacement law for the maximum of the spectrum:

$$\lambda_{max} = \frac{2898\ \mu\text{m K}}{T} \tag{2.7}$$

This law shows that higher temperatures lead to lower peak wavelengths of the radiance spectra. For Earth's atmosphere, the Sun is the most important source of radiation. With an effective surface temperature of the photosphere, the sun's first non-opaque layer of 5772 K (Prša et al. 2016), from Wien's displacement law follows a maximum of the solar spectrum at approximately 502 nm. Figure 2.1 shows the (blackbody) radiance of the sun at its surface. Although a real black body does not exist, the sun can be well approximated as one. The two vertical dashed black lines in the figure mark the borders of the visible area.

2.1.1 Attenuation and Absorption of Radiation

After being emitted in the photosphere, radiation passes the sun's chromosphere and the corona. When radiation passes through space, it is attenuated by the particles within this space which can be described by Lambert's law:

$$F = F_0 \cdot exp(-\kappa x) \tag{2.8}$$

Here, F is the attenuated irradiance of an original irradiance F_0 with an attenuation factor κ which is called absorption coefficient after passing a distance x. In general, κ is dependent on wavelength. It depends on the density and type of particles the radiation passes, which makes it a quantity that varies for every part of the path passed. Therefore, equation 2.8 becomes

$$F = F_0 \cdot exp\left\{ - \int \kappa(x) dx \right\} \tag{2.9}$$

In order to calculate F, the radiation path is separated into areas of similar absorption coefficients. When determining the absorption coefficient, every different type of molecule j and the amount N_j of it in the path needs to be taken into account:

$$\kappa = \sum_j N_j \sigma_{a,j} \tag{2.10}$$

Here, $\sigma_{a,j}$ denotes the absorption cross section of the molecules passed. It is a quantity that is the sum of multiple physical mechanisms within the absorbers. These can be

1. rotational and vibrational excitation of the absorber. These are quantized, discrete energy transitions that will lead to characteristic absorption lines as every excitation state can only be driven by photons of narrowly defined energy levels.

2. electronic excitation of the absorber. Electrons will move to higher energy states, again requiring photons of specific wavelengths. This will also lead to spectral lines.

3. ionization of the absorber. Photons with wavelengths below a molecule-specific threshold can transfer enough energy to the absorber to detach electrons from the molecules. How much energy is deposited in the detached electron can be any value above the threshold, therefore this mechanism leads to a continuous absorption pattern.

4. photodissociation of the molecule. Similar to ionization, energy above a certain threshold can lead to the dissociation of the absorber. This also leads to broadband absorption features.

Further information, e.g. on the discrete energy transition in the absorbers can be found in Bohren and Clothiaux (2006). The rotational and vibrational quantized states lead to characteristic absorption spectra of molecules where narrow lines of absorption can be found at distinct wavelengths. These lines can be super positioned or broadened by the pressure the molecules experience while absorbing radiation or by the Doppler Effect, leading to broadband features. However, the peaks of absorption features always stay at the same wavelengths, allowing for spectroscopy measurements. This allows to record spectra, fit reference absorption spectra of single or multiple molecules to these measurements and subsequently to determine the amount of of molecules of the respective species in the light path via equation 2.8.

2.1.2 From Sun to Earth

Radiation passing the sun's atmosphere is absorbed by several species, causing the so-called Frauenhofer absorption lines. In addition to that, broadband absorption and emission features caused by ionizing particles lead to reduced radiation in the UV range.

When moving away from the point of emission, instead of considering radiance as the amount of radiation emitted by a body, it is more useful to switch to the irradiance that denotes the radiant power of a body emitted onto a surface in units of $\frac{W}{m^2 \cdot nm}$. For this purpose, the radiance is integrated over a hemisphere of points that can emit on the area of interest which evaluates to

$$I_{\lambda,Sun} = F_{\lambda,Sun} \cdot \pi \tag{2.11}$$

After passing the sun's atmosphere, solar radiation on its way to Earth passes the space between the two objects that largely does not affect the radiation. However, the amount of radiation per area decreases with distance. This can be described by considering the surface area of the Sun (a sphere of radius r_{Sun}) emitting radiation according to Planck's radiation law, Equation 2.5. When moving away from the sun, the total amount of radiation stays constant but distributes isotropic on a new surface area corresponding to a sphere with radius $r_{effective} = r_{Sun} + r_{distance}$ where $r_{distance}$ is the distance between Sun's surface and the point of interest. The ratio of the two spheres yields a decrease of radiation so that the radiation at the point of interest becomes

$$I_{\lambda,distance} = I_{\lambda,Sun} \cdot \frac{r_{Sun}^2}{(r_{Sun} + r_{distance})^2} \tag{2.12}$$

When considering the solar radiation reaching the top of Earth's atmosphere (TOA), the attenuation of the radiation in the solar atmosphere and the decrease with distance lead to a TOA radiation spectrum called the Solar Spectral Irradiance (SSI). This quantity and the Total Solar Irradiance (TSI) which is the spectral integral of the SSI are well investigated quantities that are regularly measured by instruments onboard satellites or on ground, e.g. by Meftah et al. (2018) or Chance and Kurucz (2010). Figure 2.1 also includes the SSI given by Meftah et al. (2018).

SSI spectra are important input data for atmospheric radiation modeling, as they provide the initial conditions at the TOA. These spectra are not constant in reality as Earth's rotation around Sun is not circular but rather elliptical. In addition to that, Sun's brightness varies with a periodicity of about 11 years (Fligge, Solanki, and Beer 1999). This variation in brightness is linked to periodically increasing amounts of sunspots on its surface that introduce a variability on the solar irradiance. When assuming an average distance of Sun to Earth of 149.6 million kilometers (the astronomical unit) and a solar radius of 0.696 million kilometers, the spectrally integrated $I_{\lambda,distance}$ can be calculated with Equation 2.12 to approximately 1362 $\frac{W}{m^2}$. This value has an additional variance from the solar cycle of ±0.1% (Solanki, Krivova, and Haigh 2013). For the modeling calculations in this work, this variability is not taken into account as the uncertainties from the model itself (e.g. cloudiness or atmospheric absorber species concentrations) outweigh these variations.

2.1.3 Earth's Atmosphere

When entering Earth's atmosphere, the effects on solar radiation can be explained separately for each of the different layers of the atmosphere shown in Figure 2.2. These layers, from surface to TOA, are the Troposphere, the Stratosphere, the Mesosphere and the Thermosphere. The pressure from surface to TOA decreases according to the barometric height formula:

$$p(z) = p_0 \; exp\left(\frac{-z}{z_0}\right) \tag{2.13}$$

Here, z is the height, p_0 is the surface pressure and

$$z_0 = \frac{m_{air} \cdot g}{k_B \cdot T}[m] \tag{2.14}$$

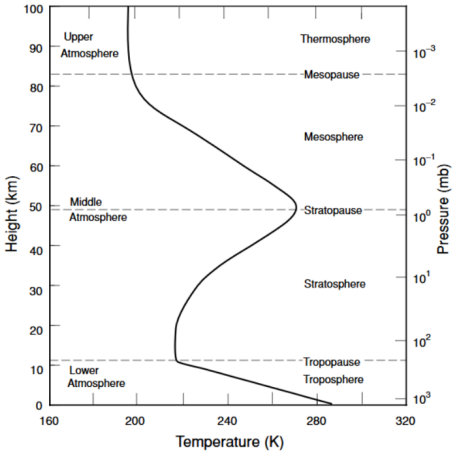

Figure 2.2: Earth's atmospheric layers and temperature profile. In the troposphere, the quasi-linear decrease of temperature with height under idealized circumstances is visible, whereas in the stratosphere, the temperature rises due to radiation absorption, mainly by ozone. Figure taken from Liou (2002).

being the scale height with the molar mass of dry air $m_{air} = 28.97 \frac{g}{mol}$, g Earth's gravity, k_B the Boltzmann constant and Temperature T. Typical values for z_0 are around 8 kilometers. The layers of the atmosphere are separated by their temperature profile, which can also be seen in Figure 2.2. In the troposphere, the temperature decreases almost linear with height under idealized conditions which can be approximated with the dry adiabatic temperature gradient:

$$\frac{dT}{dz} = -\frac{m_{air} \cdot g}{C_p} \tag{2.15}$$

C_p denotes the specific heat at a constant pressure. For $C_p = 1000.3 J/(kg \cdot K)$, $g = 9.81 \frac{m}{s}$ and $m_{air} = 28.97 \frac{g}{mol}$ this formula gives a temperature decrease with height of about $1 \frac{K}{100m}$.

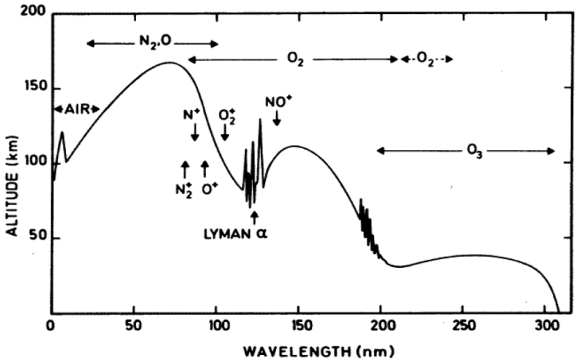

Figure 2.3: Spectral penetration of UV sunlight into the atmosphere. The curve shows the height at which the amount of radiation at the respective wavelength reduces by $\frac{1}{e}$. The figure also shows the main absorbers in the different regimes and the threshold wavelengths for ionization of different atmospheric species. Lyman α denotes prominent absorption lines from hydrogen electron excitation. Though light below approximately 315 nm is largely absorbed before reaching the surface, there are still relevant amounts of radiation at Earth's surface for wavelengths above 280 nm. Figure taken from Brasseur and Solomon (2005).

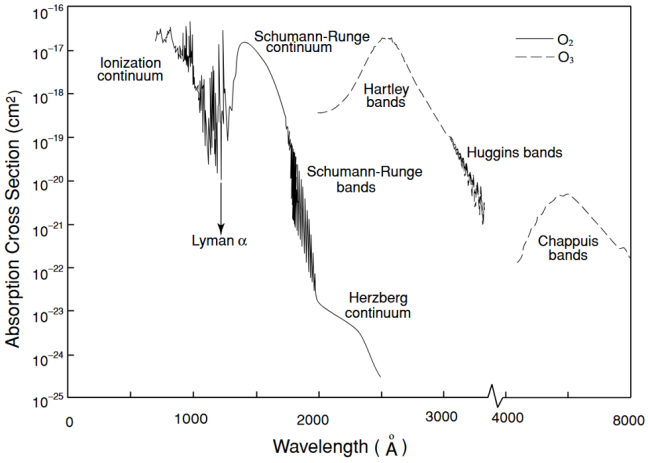

Figure 2.4: Absorption cross section of O_2 (solid line) and O_3 (dashed line) in the UV and visible range. Below 2000 Angstrom (i.e. 200 nm), O_2 is the main absorbing species up to approximately 100 nm where N_2O becomes more important, as can be seen in Figure 2.3. Above this threshold, the Hartley absorption band of O_3 is the main atmospheric absorption feature up to 4000 Angstrom. Figure taken from Liou (2002).

2.1.4 Absorption in the Upper Atmosphere

Figure 2.3 shows the depth of atmospheric penetration of solar radiation for the wavelength region below 300 nm and the main absorbing species at different heights. In the thermosphere, radiation below 100 nm is completely absorbed by N_2, O, O_2 and the ionization of O^+, O_2^+, N^+ and N_2^+. This is also a reason for the steep temperature increase in this atmospheric layer. In the mesosphere, molecular O_2 is the main absorber together with a spectral absorption feature of hydrogen, called the Lyman α lines, which is also visible in Figure 2.3, that absorb almost all radiation below 180 nm before radiation reaches the mesopause. When zooming closer into the absorption spectrum of oxygen in this wavelength area which is shown in Figure 2.4, one can disseminate the so-called Schumann-Runge bands and the Schumann-Runge continuum. The Schumann-Runge bands are absorption lines caused by electron excitement of O_2 molecules that transition to the Schumann-Runge continuum towards lower wavelengths. The Schumann-Runge bands extend to roughly 200 nanometers, the absorption takes place in heights above and reaching into the upper parts of the stratosphere.

For wavelengths below $\approx$ 242 nm, the Schumann-Runge bands are followed by the Herzberg continuum where oxygen absorbs radiation in the stratosphere. This absorption feature corresponds to the rather slow photodissociation of molecular oxygen by radiation. The resulting atomic oxygen will then react fast in comparison to the photodissociation with molecular oxygen to form O_3 molecules. These ozone molecules will again fast absorb radiation at wavelengths between 200 and 400 nm for photodissociation into molecular and atomic oxygen, represented in the broadband Hartley (200-310nm) and Huggins (310-400nm) bands. Since the reactions of O_3 formation and dissociation are faster than the photodissociation of oxygen, O_3 is the main absorber of radiation in the wavelength area of 200 to 400 nanometers in the stratosphere and upper troposphere. This cycle of O_3 creation and destruction is called the Chapman cycle, depicted in Figure 2.5. In addition, ozone has a weaker absorption band between 400 and 850 nm, called the Chappuis band that mainly acts

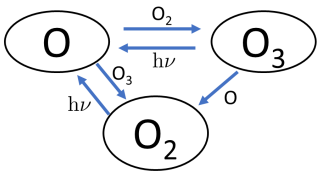

Figure 2.5: Stratospheric Chapman Cycle. The cycle starts with the photolysis and ends with the recombination of O and O_3 to $2O_2$. The different reaction constants govern the equilibrium concentrations of O and O_3. Since the reactions between O and O_3 are faster than the others, they are called the Fast Inner Cycle.

in the lower stratosphere and troposphere. These parts of the O_3 absorption spectrum are also shown in Figure 2.4.

2.1.5 Photolytic Reactions

In the previous paragraph, the characteristics fast and slow were attributed to the chemical reactions of oxygen and ozone. For a simple chemical reaction of second order

$$A + B \rightarrow C + D \tag{2.16}$$

the speed of the reaction $v_{reaction}$ is given as

$$v_{reaction} = -\frac{dA}{dt} = -\frac{dB}{dt} = k[A][B] \tag{2.17}$$

where k is the reaction constant. For a photodissociation reaction

$$AB + h\nu \rightarrow AB* \rightarrow A + B \tag{2.18}$$

with h Planck's constant and ν being the frequency of the photon absorbed in the reaction, k is called the photolysis frequency $J[s^{-1}]$ with

$$\frac{d[AB]}{dt} = -J[AB] \tag{2.19}$$

In general, J depends on the absorption cross section σ_a of the absorber, the quantum yield of the reaction, and the amount of photons with frequency ν, called the actinic flux. The quantum yield is the probability that absorption leads to the dissociation of the molecule and has values between 0 and 1. For the actinic flux, it should be noted that this includes the direct solar irradiance but also contains radiation scattered and reflected within the atmosphere and at Earth's surface. However, as also almost all reflected and scattered light originates from the sun, photolysis rates depend on the solar radiation available, and therefore follow a diurnal cycle for most parts of Earth's atmosphere.

2.1.6 Atmospheric Scattering

The amount of UV radiation that reaches further down than the stratosphere depends on the amount of ozone in the stratosphere. Aside from the above explained Chapman cycle, atmospheric dynamics and catalytic ozone destruction which will be treated in section 2.2.2 influence stratospheric ozone concentrations. This stratospheric ozone causes almost all radiation below 280 nm to be absorbed before passing into the troposphere. There, radiation is affected by Clouds, water vapor (which is also present in the stratosphere, though in much lower concentrations than in the troposphere), atmospheric trace gases, aerosols and man-made pollution. In order to understand these effects, the concept of scattering needs to be considered.

To understand atmospheric scattering, it is useful to distinguish two cases. Scattering of incident radiation with a wavelength that is large in comparison to the geometrical size of the scattering species is called Rayleigh scattering. This is the case e.g. for molecules. When the scatterer cannot be considered small in comparison to the incident radiation wavelength, the process is called Mie scattering. This is the case for larger aerosols, fog or cloud particles.

2.1.6.1 Rayleigh Scattering

Radiation can be interpreted as an electromagnetic oscillating field. When dielectric matter is exposed to this field, positive and negative charges within the field are displaced relative to each other periodically, leading to an oscillation of themselves. This oscillation emits electromagnetic radiation, which is called scattered radiation. Rayleigh scattering is given by the formula

$$\frac{d\sigma_s}{d\Omega} = \frac{\pi^2 \cdot \chi^2}{2 \cdot \epsilon_0^2 \cdot \lambda^4} \cdot (1 + cos^2\psi) \tag{2.20}$$

Here, σ_s is the Rayleigh scattering cross section, Ω is the solid angle, $\chi = \frac{\epsilon_0(\epsilon-1)}{n}$ with $\epsilon = 1.000576$ the dielectric constant is the polarizability of the scatterer, $\epsilon_0 = 8.85 \cdot 10^{-12} As/V$ the electric field constant, λ is the wavelength of the incident radiation, and ψ is the scattering angle. Two things are of special interest in this formula; First, the formula has a dependence of λ^{-4}, meaning that smaller wavelengths of the incident (solar) radiation are far stronger scattered by small particles. This is the reason the sky's color is blue by day and turns to reddish colors during sunrise and sunset (as blue radiation is scattered to an extent it is no longer visible). Second, the $cos^2(\psi)$ implies a polarization of the scattered light that is at maximum when the direction of observation is perpendicular to the incident radiation.

2.1.6.2 Mie Scattering

Mie scattering describes the scattering by spherical particles. Roedel (2000) draws the comparison to a circular hole with a diameter that is not small in comparison to the incident wavelength and that has an additional coherent excitation in the same direction as the incident light. A strong scattering peak forward is visible, for other angles an interference pattern forms. The bigger the hole in comparison to the wavelength, the more pronounced becomes the peak in the same direction as the incident light. The particle size parameter

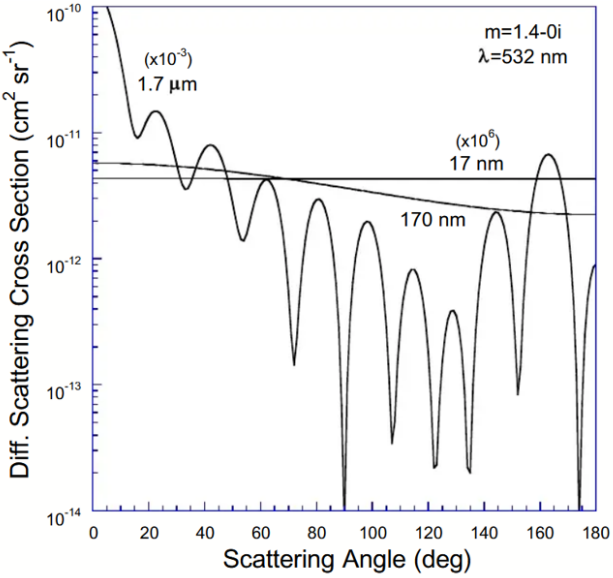

Figure 2.6: Absorption cross sections by Mie scattering angle for different particle sizes at a wavelength of λ = 532 nm and a refractive index of m =1.4. While for small particles (17 nm curve) the scattering becomes Rayleigh scattering, the angular dependence becomes more pronounced with increasing size of the particle with a strong forward peak (scattering angle of 0°). Figure taken from Hahn (2004)

$\alpha = 2 \cdot \pi \cdot r/\lambda$ with r as the radius of the scattering particle and λ as the wavelength of the incident radiation can serve as a measure to determine the shape of the scattering. Figure 2.6 shows the angular absorption cross section for different values of α. When α becomes small in the picture of Mie scattering, the resulting scattering function becomes that of Rayleigh scattering, which is the case for the 17 nm sized particle absorption cross section in Figure 2.6. In comparison to Rayleigh scattering, Mie scattering has no strong dependence on the wavelength. Due to this, the scattering of UV radiation is similar to that of radiation in the visible range.

Clouds scatter radiation via Mie scattering. This is, however, not the reason clouds appear white; For this effect, the requirements are a weakly absorbing,

optically dense medium such as clouds. Weakly absorbing means that the majority of radiation is reflected and scattered and optically dense means that a lot of scattering and reflection processes occur. These requirements are met in clouds both for visible and UV radiation. In the presence of opaque clouds, the UV radiation reaching below them is almost completely scattered and therefore reaches very small quantities, which will later be classified as UV-Index of 0, making cloud cover an important quantity when considering UV radiation at Earth's surface.

While for the UV range only Oxygen and Ozone are major absorbers, the other species play an important role as absorbers at higher wavelengths. Most notably, water vapor has very broad and strong absorption features starting around 400 nm and upwards. When thinking of greenhouse gases, the first that come to mind is CO_2 and the second CH_4, although in reality the strongest greenhouse gas is water vapor. CO_2 and CH_4 mainly absorb at infrared wavelengths.

2.1.7 Aerosols

Another quantity that needs to be taken into account for atmospheric radiant transport are aerosols. They can be of different origin and greatly vary with location. Typical sources are sea salt rising from the transition zone between ocean and atmosphere, volcanic emissions that will form plumes and can reach the stratosphere, desert dust risings and subsequent atmospheric transport, and man-made pollution such as soot or particles of the NO_X family. For Central Europe, Saharan dust events have gained some attention in the previous years as events with increased loads of aerosol in the troposphere. Aerosols mostly interact with radiation via Mie scattering or absorption, which means that their effect on visible and UV light is similar. This can have pronounced effects on the solar radiation reaching the surface and has gained economic importance with the widespread use of solar panels for electricity. The radiation effect of aerosols is usually summarized in a quantity called the Aerosol Optical Depth (AOD) which is given for different wavelengths. When modeling the atmosphere, this

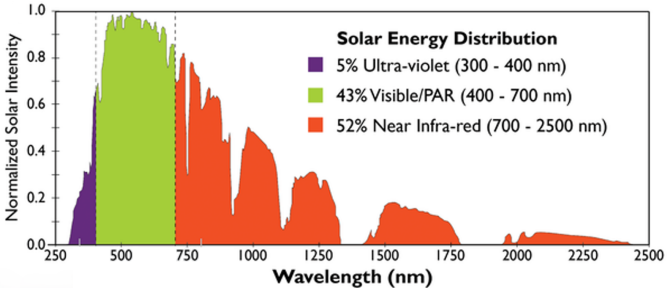

Figure 2.7: Solar irradiance at Earth's surface, normalized. The spectrum is divided into a UV range, the visible range, and the near infrared. In the UV, the absorption of O_3 is clearly visible. Figure adapted from Mishra, Stanghellini, and Hemming (2023).

value is used to take the effect of total aerosol load into account for radiation transport.

2.1.8 Reflection at the Surface

Figure 2.7 shows a surface spectrum of the solar radiation. In it, all previously discussed interactions have taken place, but radiation reflected back from the surface still needs to be taken into account. The reflection depends on the albedo $0 <= A(\lambda) <= 1$ of the surface. Albedo is a parameter that depends on wavelength, meaning that a reflective surface in the visible range is not necessarily reflective in the UV. Figure 2.8 shows broadband (0.58 -1 μm) satellite measurements of surface albedo for April, 2015. The average planetary albedo given for Earth which includes the atmosphere is $A = 0.3$, the average albedo of the surface was estimated by Otterman (1977) to approximately $A = 0.15$. This is the amount of light reflected back into the atmosphere, where it once again will interact according to the descriptions above. It can be scattered back again towards the surface, mainly by clouds, and therefore increase the amount of radiation measured. This can lead to the interesting case that, in the UV, the radiation measured can even reach values above the theoretical solar blackbody irradiance.

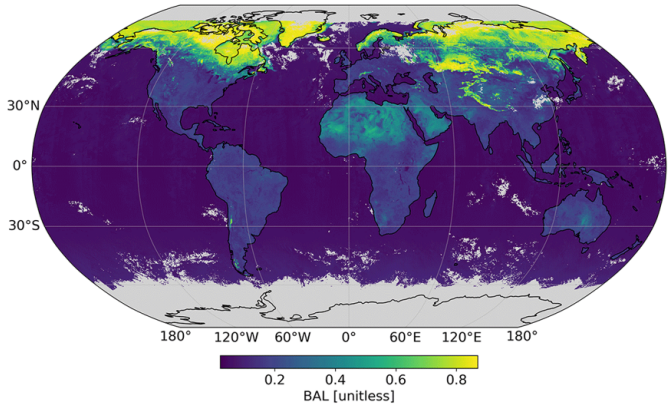

Figure 2.8: Broadband (0.58 - 1 μm) Blue Sky Surface albedo (BAL) as 5-day average starting April 1,2015 from combined satellite observations. The grayed out areas were not illuminated enough to provide values. Areas with snow are brightly visible in the Northern Hemisphere. The Saharan Desert has a high surface albedo as well. Figure taken from Riihelä, Jääskeläinen, and Kallio-Myers (2024).

2.2 Stratospheric Dynamics and Ozone Chemistry

Towards the end of the last century, atmospheric scientists raised public alarm as they had discovered that the stratospheric ozone layer was increasingly damaged by human made atmospheric emissions. As explained in Section 2.1.4, O_3 is the main absorber of UV radiation in the atmosphere. If its concentration decreases, the UV radiation exposure on Earth's surface increases, leading to the health risks for humans detailed in the Introduction. For the case of sufficiently reducing the O_3 layer and therefore allowing a major part of solar UV radiation to reach Earth's surface, it could even affect the habitability of the planet. To prevent this, in 1987 the Montreal Protocol was concluded ("Montreal Protocol on Substances that Deplete the Ozone Layer" 1987) with the goal to reduce the emission of O_3 damaging substances. This section explains the dynamics of the stratosphere, the mechanisms that lead to ozone formation and destruction

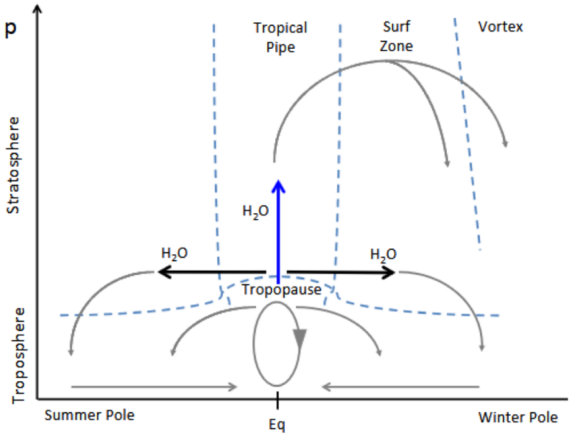

Figure 2.9: Stratospheric Brewer-Dobson circulation. Here, H_2O as representative of tropospheric air masses is depicted rising from the tropical troposphere to the stratosphere. A part of the air masses (solid black arrows) move towards the poles in the lower stratosphere, eventually sinking back into the troposphere. There, the air masses move back toward the tropics to form a circle. The other part of the air masses ejected (blue arrow) into the stratosphere rise higher into the stratosphere before also moving towards the poles and sinking back down. As for H_2O, the process is equivalent for O_3 and other particles. Figure taken from Flury, Wu, and Read (2012).

and which substances are related to these processes. Reaction rates for the processes described can be found in Burkholder et al. (2020).

2.2.1 Stratospheric Dynamics

A key role of stratospheric dynamics is played by the Brewer-Dobson Circulation (Brewer 1949, Dobson and Harrison (1926), Dobson (1956)), which is described in detail by Butchart (2014) and depicted exemplary for H_2O in Figure 2.9. It consists of the upwelling of air masses in the tropics high up into the stratosphere and the subsequent transport toward the poles where the air masses sink down. This is the main mechanism of transport from troposphere to stratosphere. Tropospheric Ozone, water vapor and other atmospheric constituents are transported and distributed into the polar regions of

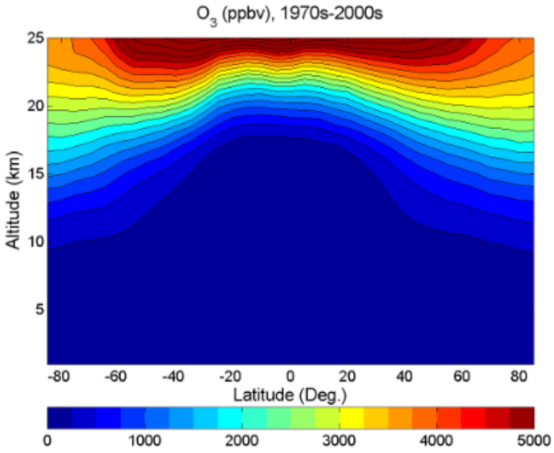

Figure 2.10: Climatological O_3 height profile of the troposphere and lower stratosphere, in ppbv The concentrations in the stratosphere are higher in the stratosphere where UV radiation is available and the Chapman Cycle takes place. Figure taken from Liu et al. (2013).

the stratosphere. This effect leads to an accumulation of O_3 in polar regions. Longer-lived species in the troposphere are transported with the same mechanism into the stratosphere. This includes CH_4 and particles that form catalytic cycles with ozone as will be discussed in Section 2.2.2.

Another distinct feature of stratospheric dynamics is the polar vortex. When the polar night begins in autumn (on either hemisphere), the polar air masses are cooled down in comparison to the air masses closer to the equator that are still heated by the Sun during day. A strong wind is created that is bent by the Coriolis Force to rotate around the poles, creating the polar vortex. This leads to a transport barrier that reduces the mixing of polar air masses during winter with those of lower latitudes.

Figure 2.10 shows the average structure of tropospheric and stratospheric O_3 as climatology for the 1970s to the 2000s. As can be seen, O_3 concentrations are highest in the middle stratosphere. Figure 2.11 shows an overview of the

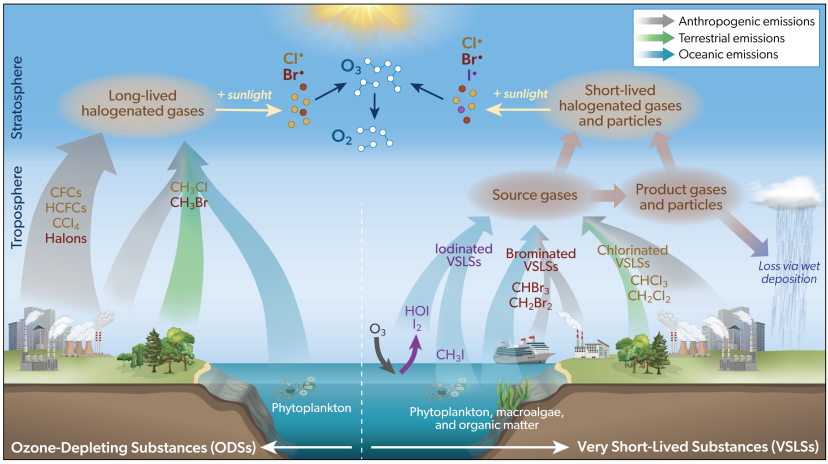

Figure 2.11: Halogene-related stratospheric ozone depletion. On the left side of the graphic, long-lived, mostly anthropogenic sources of ozone depleting substances and their origin are depicted. On the right side of the graph, the much shorter-lived substances with atmospheric lifetimes of < 0.5 years are shown. Figure taken from Laube (2022)

halogen-related mechanisms that lead to ozone depletion in the stratosphere. These mechanisms are discussed in the following parts of this Section. First, the mechanisms linked to the Ozone-Depleting Substances (ODS) will be explained, followed by explanations on the contributions of Very Short-Lived Substances (VSLS).

2.2.2 Catalytic Ozone Destruction

The Chapman Cycle that was introduced in Section 2.1.4 includes photolytic destruction of O_3 via

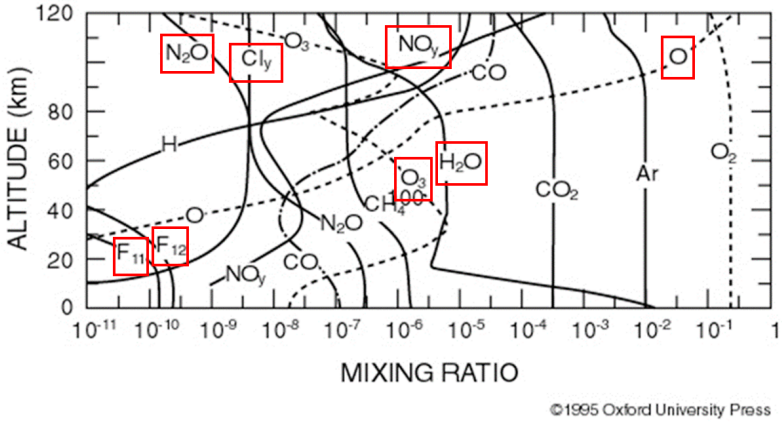

Figure 2.12: Atmospheric chemical constituent mixing ratio height profiles. O_2 is almost constant in the atmosphere, as are CO_2 and Argon. O_3 shows a pronounced peak at approximately 30 kilometers height. Constituents relevant for stratospheric O_3 chemistry are in red boxes. Figure adapted from Goody (1996).

$$\begin{aligned} & O_3 + h\nu_{\lambda<1100nm} \rightarrow O_2 + O(^3P) \\ \text{or} \quad & O_3 + h\nu_{\lambda<310nm} \rightarrow O_2 + O(^1D) \\ & O + O_3 \rightarrow 2\,O_2 \\ \hline \text{net } & 2\,O_3 + h\nu \rightarrow 3\,O_2 \end{aligned} \tag{2.21}$$

Here, $O(^1D)$ is an excited state of atomic oxygen and $O(^3P)$ the ground state of atomic oxygen. The reaction of $O + O_3 \rightarrow 2O_2$ is slow in comparison to the O_3 generating reaction $O + O_2 + M \rightarrow O_3 + M$ where M is a reaction partner. This means that, while a single O_3 atom only lives on the scale of hours, its residuals will likely recombine to a new O_3 molecule. If the Chapman Cycle was the only chemical mechanism of O_3, its concentrations in the stratosphere would be far higher than they are.

Figure 2.12 shows the atmospheric concentration of different chemical constituents. Several of these have the potential to interact with ozone in catalytic cycles which will be explained in the following.

In the presence of water vapor, the excited atomic oxygen state $O(^1D)$ can react with it via

$$O(^1D) + H_2O \rightarrow 2\,\mathrm{OH} \tag{2.22}$$

which forms the OH radical. OH radicals can catalytically destroy O_3 via

$$\begin{aligned} O_3 + OH &\rightarrow O_2 + HO_2 \\ HO_2 + O &\rightarrow OH + O_2 \\ \hline \text{net } O_3 + O &\rightarrow 2\,\mathrm{O_2} \end{aligned} \tag{2.23}$$

At very low concentrations of atomic oxygen, another reaction is

$$\begin{aligned} O_3 + OH &\rightarrow O_2 + HO_2 \\ HO_2 + O_3 &\rightarrow 2\,\mathrm{O_2} + OH \\ \hline \text{net } 2\,\mathrm{O_3} &\rightarrow 3\,\mathrm{O_2} \end{aligned} \tag{2.24}$$

Another catalytic ozone destruction can be triggered in the presence of N_2O:

$$N_2O + O(^1D) \rightarrow 2\,\mathrm{NO} \tag{2.25}$$

This will lead to the reaction

$$\begin{aligned} O_3 + NO &\rightarrow O_2 + NO_2 \\ NO_2 + O &\rightarrow NO + O_2 \\ \hline \text{net } O_3 + O &\rightarrow 2\,\mathrm{O_2} \end{aligned} \tag{2.26}$$

$CFCl_3$ and CF_2Cl_2 are human made Chloro-Fluoro-Carbons (CFC) that are very stable in the troposphere and eventually are transported in the strato-

sphere. There, they can be photolyzed, forming atomic Cl, which, as a halogen, possesses unpaired electrons, making it react radical-like with ozone:

$$\begin{aligned} O_3 + Cl &\rightarrow ClO + O_2 \\ ClO + O &\rightarrow Cl + O_2 \\ \hline \text{net } O_3 + O &\rightarrow 2\,O_2 \end{aligned} \tag{2.27}$$

This reaction requires atomic oxygen to regenerate the Cl atom which is only available in the upper parts of the stratosphere where O_2 is photolyzed into $2\,O$. For lower parts, a longer chain reaction takes place:

$$\begin{aligned} Cl + O_3 &\rightarrow ClO + O_2 \\ O_2H + ClO &\rightarrow HOCl + O_2 \\ HOCl + h\nu &\rightarrow OH + Cl \\ OH + O_3 &\rightarrow O_2H + O_2 \\ \hline \text{net } 2\,O_3 + h\nu &\rightarrow 3\,O_2 \end{aligned} \tag{2.28}$$

Reaction 2.27 can function exactly the same way with the halogen Br instead of Cl. If both Br and Cl are present, they can form the reaction cycle

$$\begin{aligned} O_3 + Cl &\rightarrow ClO + O_2 \\ O_3 + Br &\rightarrow BrO + O_2 \\ ClO + BrO &\rightarrow BrCl + O_2 \\ BrCl + h\nu &\rightarrow Br + Cl \\ \hline \text{net } 2\,O_3 &\rightarrow 3\,O_2 \end{aligned} \tag{2.29}$$

This reaction chain does not require atomic oxygen to take place, which makes it relevant for the lower stratosphere.

The reactions discussed in this section are not to be seen as independent. For example, OH and O_2H appear in Equation 2.24 and Equation 2.28 which means

these reaction cycles can also mix. For simplicity, not all possible reaction chains are shown.

2.2.3 Heterogeneous Ozone Destruction

Taking into account the O_3 accumulation caused by the Brewer-Dobson circulation, the Chapman cycle and the losses from the catalytic O_3 descruction cycles above still do not describe the observed ozone decreases in the polar regions in spring, shown in Figure 2.13. Here, the Total Column O_3 (TCO_3) is given in Dobson Units. This quantity is a O_3 specific unit that gives the amount of the TCO_3 in units of 0.1 mm height if the entire ozone was brought to a temperature of 273.15 K and 1000 hPa pressure. E.g. 300 Dobson Units (DU) mean a 30 mm high ozone column at those conditions for the given location.

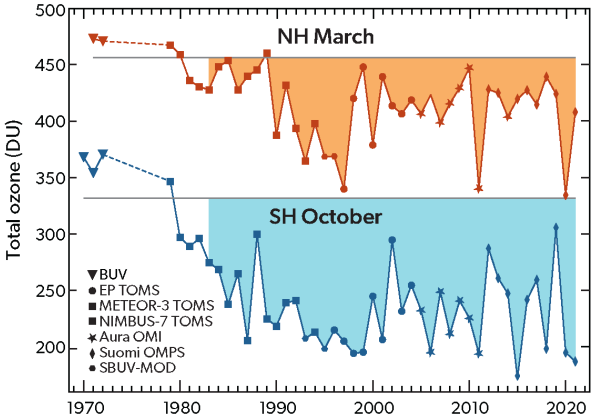

Figure 2.13: Ozone holes in arctic and antarctic spring. The curves show the average Total Column Ozone in Dobson units for latitudes above 63°N and below 63°S with the different markers showing measurements from different satellite instruments. The gray lines mark the average values for the years before 1983. Both curves show an ozone depletion with the start of the respective spring season. These decreases can be attributed to heterogeneous ozone depletion. Figure taken from the Scientific Assessment of Ozone Depletion, 2022, Chapter 4 Chipperfield (2022)

In the arctic and antarctic polar night and spring, temperatures regularly fall below 195 K, allowing for the formation of polar stratospheric clouds (PSC)

in the lower half of the stratosphere (Roedel 2000). Below this temperature threshold, Nitric Acid Trihydrate (NAT, constitutes of $HNO_3 \cdot (H_2O)_3$) condensates and forms PSC. If the temperature decreases below 190 K (Roedel 2000), supercooled and thus liquid Sulfuric Acid (H_2SO_4), originating from volcanic eruptions, can form ternary solutions (STS) with Nitric Acid (HNO_3) and water vapor. Finally, if temperatures decrease below 188 K (Roedel 2000), ice particles can form a third type of PSC.

The temperature thresholds given in the previous paragraph are to be considered as average values as they depend on pressure. Figure 2.14 shows exemplary the PSC composition of a satellite observation over the Antarctic.

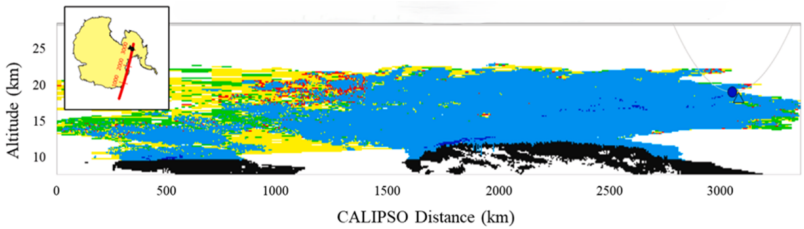

Figure 2.14: Occurrence of different types of PSC in the Antarctic for 2008-09-03. The figure shows the CALIPSO sattellite Lidar data of one overpass (shown in the inlay). The colors show different types of PSC measured: blue is ice, yellow is NAT, green is STS, red are very high NAT concentrations, black are tropospheric data points. In this case, the majority of PSC are ice clouds. Figure adapted from Lavy et al. (2024).

The constituent of PSC HNO_3 forms in the stratosphere via the reaction

$$NO_2 + OH + M \longrightarrow HNO_3 + M \tag{2.30}$$

where M can be any reaction partner. If no sunlight and therefore no OH from photolytic H_2O splitting is present, a longer reaction chain can lead to a similar result:

$$\begin{aligned} NO_2 + O_3 &\rightarrow NO_3 + O_2 \\ NO_2 + NO_3 + M &\rightarrow N_2O_5 + M \\ N_2O_5 + H_2O(+particle) &\rightarrow 2HNO_3(+particle) \\ \hline \text{net } 2NO_2 + O_3 + H_2O &\rightarrow 2HNO_3 + O_2 \end{aligned} \tag{2.31}$$

In both cases, NO_2 is removed from the stratosphere. This reduction of NO_2 is relevant for catalytic ozone destruction as BrO and ClO which are products of an intermediate step in the catalysis reaction chains are deactivated via equation

$$NO_2 + ClO + M \rightarrow ClONO_2 + M, \tag{2.32}$$

where $ClONO_2$ is a nonreactive reservoir gas in terms of catalytic ozone destruction. Condensed HNO_3 in PSC can sediment out of the stratosphere, reducing the NO_2 availability in the stratosphere and thus inhibiting equation 2.32.

The nonreactive reservoir gas $ClONO_2$ can be activated in the presence of PSC and HCL or H_2O via the equations

$$\begin{aligned} ClONO_2 + HCl &\rightarrow Cl_2 + HNO_3 \\ Cl_2 + h\nu &\rightarrow Cl + Cl \end{aligned} \tag{2.33}$$

and

$$\begin{aligned} ClONO_2 + H_2O &\rightarrow HOCl + HNO_3 \\ HOCl + h\nu &\rightarrow OH + Cl \end{aligned} \tag{2.34}$$

where, in both cases in a first step the reservoir gas is activated and in a second step the products are photolyzed to ozone depleting catalysts. The

first parts of the equations require the presence of PSC to meet the necessary activation energy, the second parts require sunlight. This is the reason the mechanism happens in spring, when PSC have formed and sunlight is present. These processes happen in the stratosphere where the sun rises earlier than at Earth's surface, which is why it can happen at solar elevations above 90°, i.e. before sunrise. The consequence is a rapid (timescale of weeks) decrease in ozone concentration. Eventually, the PSC dissolve as the stratosphere warms up and the reservoir gases can no longer be activated, allowing the ozone to regenerate.

2.2.4 Very Short Lived Substances

As can be seen in figure 2.11, there is an additional contribution to stratospheric ozone depletion by so-called Very Short-Lived Substances (VSLS) with atmospheric lifetimes of less than 0.5 years. Their sources are natural and anthropogenic. VSLS amounts measured in the stratosphere have increased from 2000 to 2017 (Hossaini et al. 2019). It is noteworthy that controlling VSLS emissions is not part of the Montreal Protocol ("Montreal Protocol on Substances that Deplete the Ozone Layer" 1987). The 2022 Scientific Assessment of Ozone Depletion states in chapter 1 that "VSLS now contribute about 25% to stratospheric bromine and 3–4% to stratospheric chlorine" (page 80, Laube 2022). Due to their short lifetime and localized emissions, their concentrations show strong local variability. Sinnhuber and Meul (2015) find that 6 ppt of VSLS bromine cause a global mean TCO_3 reduction of 5-10 DU. While brominated VSLS are mainly of natural origin, chlorinated VSLS have a major contribution from anthropogenic emissions (Sinnhuber and Meul 2015).

2.3 The UV-Index

The introduction of this thesis detailed the health related effects of solar UV radiation. In combination with reports of behaviourally increased sun exposure and well-established observations of stratospheric ozone depletion led to a meeting in 1994 organized by the World Health Organization (WHO), the World Meteorological Organization (WMO) and the International Commission on Nonionizing Radiation Protection (ICNIRP). The goal was to define, standardize and harmonize a UV-Index (UVI). This meeting was followed up by a second convention in 1997 (*Report of the WMO-WHO Meeting of Experts on Standardization of UV Indices and their Dissemination to the Public*) that refined the UV-Index to what is displayed nowadays with a fixed color scale and predefined symbols to-be-used, which is summarized in a practical guide (Rehfuess 2002).

2.3.1 Definition

In the preface of WHO's practical guide on the Global Solar UV-Index, the definition of the UV-Index is given as follows:

> *"The Global Solar UV Index (UVI)* [...] *is a simple measure of the UV radiation level at the Earth's surface and an indicator of the potential for skin damage. It serves as an important vehicle to raise public awareness and to alert people about the need to adopt protective measures when exposed to UV radiation."*
>
> Global solar UV index : a practical guide, page IV (Who 2002)

In mathematical terms, the definition of the UVI is

$$\mathrm{UVI} = k_{er} \int_{250nm}^{400nm} I_\lambda \cdot s_{er}(\lambda) d\lambda \tag{2.35}$$

where $k_{er} = 40\frac{m^2}{W}$, $I_\lambda\left[\frac{W}{m^2 nm}\right]$ is the solar spectral irradiance and $s_{er}(\lambda)$ is the so-called spectral erythemal weighting factor. The prefactor k_{er} was defined to make the result of the spectral integral dimensionless and to bring it to a scale that ranges from 1 to approximately 10, although it is not limited towards higher values. s_{er} was designed to weigh I_λ with its harmfulness to humans. It is defined in the norm ISO/CIE 17166 as

$$s_{er}(\lambda) = \begin{cases} 1.0 & \text{for } 250nm \leq \lambda \leq 298nm \\ 10^{0.094(298-\lambda)} & \text{for } 298nm < \lambda \leq 328nm \\ 10^{0.015(140-\lambda)} & \text{for } 328nm < \lambda \leq 400nm \end{cases} \tag{2.36}$$

In subsection 2.1.6, it was mentioned that radiation at lower wavelengths than 280 nm rarely passes into the troposphere and thus the surface, mainly due to the absorption by O_3. Therefore, when calculating the UV-Index, its spectral integral can usually be confined to 280 - 400 nm, this is done e.g. by Deutscher Wetterdienst (DWD) (Staiger and Koepke 2005) for its operational UV-Index forecast. Figure 2.15 shows s_{er} for the spectral range of 280 to 400 nm. The lower end of the wavelength interval at 280 nm is weighted 4 orders of magnitude stronger than the upper end at 400 nm. This means that even small amounts of radiation close to 280 nm at the surface have a pronounced impact on the UV-Index.

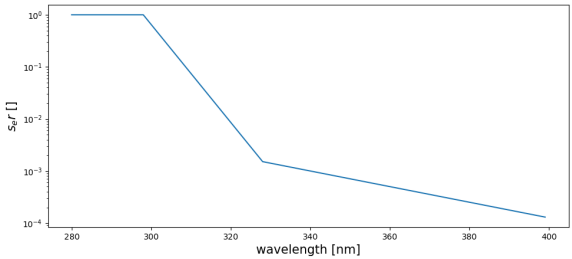

Figure 2.15: Erythemal weighting factor s_{er} for the calculation of the UV-Index. This dimensionless factor weighs radiation in the UV with its harmfulnes to humans. The y axis of this plot is logarithmic. The higher the wavelength, the less harmful the radiation becomes. s_{er} was defined in ISO/CIE 17166.

For each location, the UVI is defined as the maximum value of a day of 30-minute averaged intervals (*Report of the WMO-WHO Meeting of Experts on Standardization of UV Indices and their Dissemination to the Public* 1997).

2.3.2 Influencing Factors

In section 2.1 the factors affecting solar irradiance on its way to Earth's surface were discussed in detail. For the UVI, factors that influence it (and therefore should be taken into account when calculating it) are:

- Solar Zenith Angle (SZA): A higher Sun elevation (i.e. lower SZA) causes a higher UVI
- Cloud Cover: Clouds obscure the surface from solar radiation, lowering the UVI
- Overhead Ozone: O_3 absorbs UV radiation, lowering the UVI
- Aerosol Optical Depth (AOD): Increased AOD increases the scattering of UV radiation, reducing the UVI
- Surface Albedo: Increased surface albedo reflects higher ratios of UV radiation back, increasing the UVI
- Orography: At higher surface altitudes, less radiation is scattered in the atmosphere, increasing the UVI

The estimation of the magnitude of the influence of these factors on the UVI is part of this thesis.

When calculating the solar irradiance on a surface, the cosine of the angle between surface and the Sun needs to be taken into account. Assuming a horizontal surface (which is the case for atmospheric models), this angle is the Solar Zenith Angle (SZA) that is defined as 0° if the Sun is perpendicular to the plane of incidence:

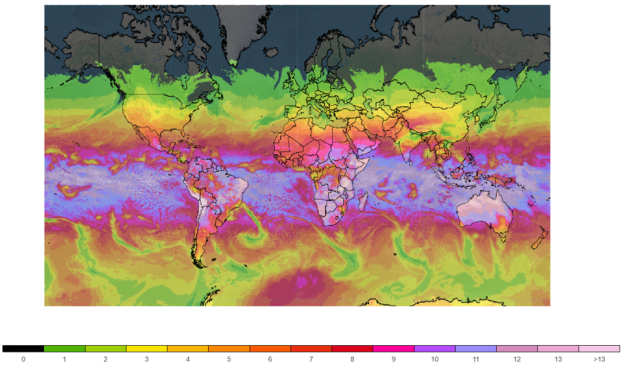

Figure 2.16: Operational global UV-Index forecast by DWD for 31.10.2025. The scale indicates values of UVI. UVI values show the SZA dependent decline following Equation 2.37 towards the polar regions. Areas that are covered by clouds can be seen as areas of reduced UVI values. When looking at the Andes in South America, the UVI increase with altitude can be seen. Figure adapted from the DWD webpage, accessed at 31.10.2025 (*Deutscher Wetterdienst - Tägliche Vorhersagen des UV Index*)

$$I_{\lambda,surface} = I_{\lambda} \cdot cos(SZA) \tag{2.37}$$

If taking no other influencing factors into account, the UVI would be highest at the current subsolar point on Earth's surface, which currently moves throughout the year between 23.4° North and South, and decline radially with cos(SZA) from there. For the calculation of the UVI at Earth's surface, $I_{\lambda,surface}$ is set to 0 for SZA values above 90° as this corresponds to night.

The last influencing factor is the orography of Earth's surface. The higher up, the less atmosphere is above the respective location. This means that less interaction between radiation and atmosphere will occur, thus increasing the amount of UV radiation at the location. Figure 2.16 shows an example daily global UVI forecast as published by DWD (*Cloudy and Clear Sky Turbid UV Index and Dose Forecast: https://kunden.dwd.de/uvi/index.jsp* 2025).

2.3.3 Future UV-Index Development

A recent study by Chatzopoulou et al. (2025) investigated the future UVI development towards the end of the 21^{st} century from the perspective of the different possible socioeconomic pathways defined in the 6th phase of the Coupled Model Intercomparison Project (CMIP6, Eyring et al. (2016)). For the scenario with lowest Greenhouse Gas (GHG) and aerosol emissions, they found an UVI increase of about 20% in Europe and Northern America which was attributed to decreased aerosol loads while decreasing over polar regions by up to 10% due to surface reflectivity changes. For the most extreme radiative forcing scenario with almost a tripling of CO_2 compared to current levels by the end of the century, it found widespread decreases of UVI over the globe with some local exceptions which was attributed to an acceleration of the Brewer-Dobson circulation due to increased GHG amounts and widespread AOD increases. This highlights a common misconception about the UVI; It is often considered to be analogous to temperature, and thus a global warming might be misinterpreted to be accompanied by an increase of UV radiation exposure. But heating the atmosphere does not make it less opaque to UV radiation.

Statements about the future development of UV radiation are to be considered with great care as influencing factors may affect each other and have great uncertainties; Stratospheric O_3 chemistry changes depending on the temperature (Langematz 2018, Karagodin-Doyennel et al. (2023)), and recent satellite evaluations show a decrease of ocean cloud cover (Tselioudis et al. 2024).

2.4 Atmospheric Modeling

The explanations in this section refer to models similar to the ICOsahedral Nonhydrostatic Model (ICON) used in this thesis. There is a large variety in approaches for modeling the atmosphere that will not be covered to full extent in this thesis.

When modeling the atmosphere, the physical processes such as radiation or transport need to be represented adequately accurate in models. Adequately accurate means that the precision of their representation is high enough to ensure validity at the scale of modeling for the processes investigated. An example can be atmospheric scattering of radiation; In models, it needs to be taken into account as a means of radiant energy transport, especially when radiation is to be used for photolysis rate calculations. But going into detail towards the physically correct representation of Mie Scattering would increase the computational cost to unreasonable amounts while improving the accuracy of heat transfer and photolysis rates only marginally.

This section explains the underlying principles of atmospheric modeling which will be followed by a description of the model used in this thesis in the next chapter.

2.4.1 Modeling Principles

The principle of Global Circulation Models like ICON is to separate the atmosphere into a 3-dimensional grid of boxes, or cells. Typically, the resolution of the model is defined as the size of the horizontal grid cells. The lowermost horizontal layer is set to the orographic height of the respective point on Earth's surface that is represented by the grid cell.

For each of the cells, an initial state is defined with respect to its content. This includes the amount of air mass, temperature, pressure, horizontal and vertical wind speed and content of different atmospheric species such as water vapor, ice particles or trace gases. Atmospheric modeling is an initial-value problem, the output depends critically on the input that was given. For this reason, great effort is taken to define the initial state to the best accuracy possible. For Numerical Weather Prediction (NWP) that provides weather forecasts on national, continental and global scales, this means that atmospheric measurement data are assimilated into the initial state of the model as frequently as several times per day.

Once the grid and the input state are defined, the model can propagate forward in time. For this, the atmospheric radiation transfer discussed in section 2.1 is calculated and combined with chemical reactions and equations of motion (or momentum) that describe the movement of air masses. How exactly these equations are implemented is individual to each model. The next chapter will detail the equations of motion as implemented in the ICON model used in this thesis.

2.4.2 Limitations for Models

The accuracy that can be applied to atmospheric models is mainly limited by the computing power available. In the 3rd edition of "Physik unserer Umwelt" published in 2000, Roedel (2000) gave typical horizontal resolutions of "few hundred kilometers" (p. 457) and around 20 vertical levels for atmospheric modeling. For this work, the highest global resolution used was 13 kilometers with 120 height layers. These numbers showcase the increase in computational power availability during the last decades. Increasing the resolution allows for a more accurate depiction of dynamics. In addition, a variety of atmospheric effects can only be resolved when moving to small grid cells in the model, e.g. gravity waves or convection. Effects that cannot be resolved are usually parametrized in the model.

The propagation in time introduces time itself as fourth dimension of the model. When moving ahead in time, the state of the model is calculated by solving the equations of motion and radiation transfer for the given time difference. If the timestep is chosen too coarse with respect to the geometric grid, it can happen that the air masses of one cell are transported so fast they skip one cell and are transported into the second neighbor cell, leading to model errors. To prevent this, the Courant–Friedrichs–Lewy (CFL) criterion is defined to determine the maximum dynamic or transport time step. For one dimension, it is given as

$$\Delta t < \frac{\Delta x}{u}, \tag{2.38}$$

where u in the case of atmospheric modeling is the highest velocity occurring in the cell, t is time and Δx is the horizontal grid size. This means that when increasing spatial resolution, the temporal resolution needs to be increased as well.

Another limitation lies within the complexity of the chemistry to be used in the model. Section 2.2 detailed the most important chemical reactions of O_3 in the stratosphere. Reaction rates are always attributed with errors, listed e.g. in Burkholder et al. (2020). Implementing these reactions requires an online calculation of photolysis rates together with a chemistry scheme which is computationally expensive. This makes it desirable to reduce the complexity by introducing parameterizations for the chemical reactions. For the case of stratospheric ozone, this will be explained in the next chapter.

The implementation of stratospheric ozone calculations in the model allows to couple the resulting atmospheric ozone fields interactively into the radiative transport module of the model, resulting e.g. in a more realistic representation of stratospheric heating.

3 Model Setup

All simulations in this thesis were performed using the ICOsahedral Nonhydrostatic (ICON) model coupled to the module Aerosols and Reactive Trace gases (ART). This chapter describes ICON, its components, and the changes applied to it in this thesis. The changes were applied to optimize ozone forecasting and to allow for the calculation of UVI values. Figure 3.1 shows the setup used for the operational UVI forecast by DWD and the setup presented in this thesis. The most important changes are that ozone can now be coupled interactively to the radiative transport module in ICON and no external ozone data or radiation calculations are required for the UVI calculation.

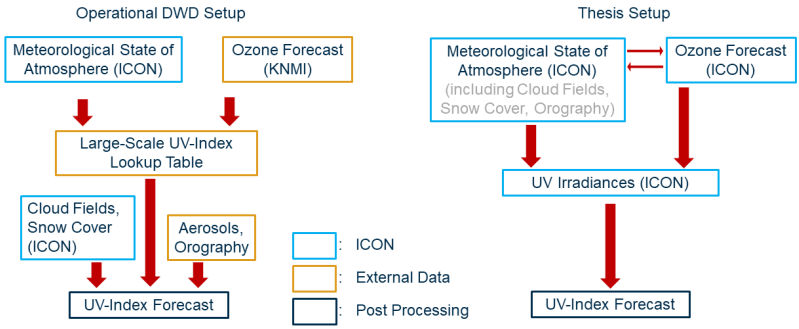

Figure 3.1: Operational DWD setup (left) and thesis setup (right) to calculate UVI values. The operational setup follows Staiger and Koepke (2005).

3.1 ICON Model

3.1.1 Grid Structure

ICON was developed jointly by DWD and the Max Planck Institute for Meteorology. Its fundamentals are explained by Zängl et al. (2015). The major goals in the development of ICON were to create a model that is non-hydrostatic, has easy mass conservation, allows for high resolution nesting of fine local grids in a coarser global grid and at the same time is computationally efficient and scalable to large amounts of computing resources. ICON is used for operational weather forecasting, but can also be used for longer timescales, e.g. until the end of the current century for climate forecasts.

To achieve this, an icosahedral grid depicted in Figure 3.2 is used across the globe. The resolution of the model is not limited towards smaller grids. ICON grids are denoted *RnBk*, where n is the amount of parts the original icosahedral face sides are separated into. k is the amount of separations within each of the so created triangles. The resolution of the solid black grid depicted on the left

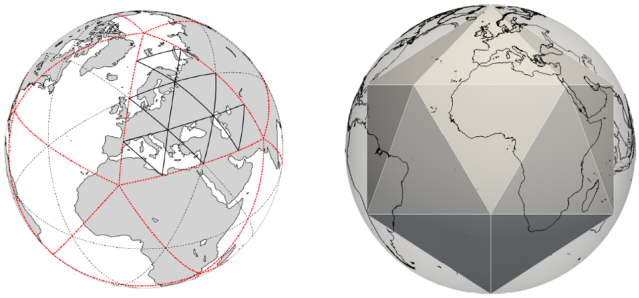

Figure 3.2: ICON grid structure. On the right side, the base icosahedral grid is depicted. Each of its triangular faces can be separated into smaller triangular grid cells. One caveat arises from this; while the smaller triangles will have vertices with 6 adjacent cells, the original icosahedron vertices only have 5 adjacent cells. Figure taken from the ICON Tutorial 2023 (Prill et al. (2023)).

Grid	$\overline{\Delta x}$ [km]
R2B6	40
R3B7	13
R19B7	2

Table 3.1: ICON Grids used in this Thesis.

side of Figure 3.2 thus becomes *R2B1*. The grid size is defined in Prill et al. (2023) as

$$\overline{\Delta x} \approx \frac{5050}{n2^k}[km] \tag{3.1}$$

For the above mentioned *R2B*1 grid, this means a resolution of 1262.5 km. The grids and their respective cell sizes used in this thesis are listed in table 3.1. ICON allows for a custom grid generation. These can be either global or in a restricted area. This can be done via the DWD ICON tools, a suite of command line commands created by DWD. An online wrapper for the creation of custom grids is provided by *Zonda* (2025).

3.1.2 Dynamical Core

The system of equations used in ICON for the movement of air masses is

$$\frac{\partial v_n}{\partial t} + \frac{\partial K_h}{\partial n} + (\xi + f)v_t + w\frac{\partial v_n}{\partial z} = -c_{pd}\theta_v\frac{\partial \pi}{\partial n} + F(v_n) \tag{3.2}$$

$$\frac{\partial w}{\partial t} + v_h \cdot \nabla w + w\frac{\partial w}{\partial z} = -c_{pd}\theta_v\frac{\partial \pi}{\partial z} - g \tag{3.3}$$

$$\frac{\partial \rho}{\partial t} + \nabla \cdot (\boldsymbol{v}\rho) = 0 \tag{3.4}$$

$$\frac{\partial \rho\theta_v}{\partial t} + \nabla \cdot (\boldsymbol{v}\rho\theta_v) = \tilde{Q} \tag{3.5}$$

with the Exner function

Symbol	Description
v_n	horizontal velocity normal to triangle edges
v_t	tangential velocity component
v_h	horizontal wind vector
$\boldsymbol{v}$	three-dimensional wind vector
w	vertical wind component
ρ	density (including liquid and solid hydrometeors)
θ_v	virtual potential temperature
ξ	vertical vorticity component
f	Coriolis parameter
$K_h = \frac{1}{2}(v_n^2 + v_t^2)$	horizontal part of kinetic energy
c_{pd}, c_{vd}	specific heat capacity of dry air at constant pressure (p) and constant volume (v)
$R_d = c_{pd} - c_{vd}$	gas constant of dry air
g	gravitational acceleration
$p_{00} = 1000\text{hPa}$	reference pressure
$\frac{\partial}{\partial n}$	horizontal derivative in edge-normal direction
$F(v_n)$	horizontal momentum source terms
$\tilde{Q}$	diabatic heat-source terms

Table 3.2: Description of symbols in the dynamical core, Equations 3.2 to 3.5.

$$\pi = \left(\frac{R_d}{p_{00}}\rho\theta_v\right)^{R_d/c_{vd}} \tag{3.6}$$

The explanation of the symbols in the equation system is given in Table 3.2. One notable simplification in this equation system is the conservation of mass, expressed in Equation 3.4. This means that mass, including hydrometeors and moisture, is conserved in ICON. Precipitation mass loss and evaporation mass gain as well as pressure changes at the surface levels that would follow from these effects are neglected. A detailed explanation, e.g. on the discretization of these equations, is given in Zängl et al. (2015).

3.1.3 Radiative Transport

For the propagation of radiation and its interaction with atmospheric particles, ICON uses the ecRad scheme developed by the European Centre for Medium-Range Weather Forecasts (ECMWF) with a detailed description given by Hogan and Bozzo (2018). It was adapted in 2019 for the use of ICON (Rieger (2019)) and since then further developed with the correlated k-Method described in Hogan and Matricardi (2022).

ecRad incorporates the physical processes described in section 2.1 and provides radiative fluxes for binned wavelength parts of the solar spectrum. These can then be used to e.g. calculate the heating rate of the atmosphere by radiation or the TOA solar fluxes (depicted in Rieger (2019)). In its current operation mode, ecRad receives meteorological input such as water vapor by ICON and reads in climatological values for O_3, aerosol content and fixed, predefined concentrations of CO_2, N_2O, CH_4, $CFC11$ and $CFC12$. The implementation of ecRad in ICON allows for the replacement of those predefined species fields with interactive tracers such as the ones provided by the ART module (explained in section 3.2).

3.1.4 Vertical Coordinates

In a nonhydrostatic model, pressure does not necessarily decrease monotonically with height. This makes pressure as vertical coordinate unsuitable. Therefore, the height levels are defined in geometric altitudes. The lowermost (surface) level follows a predefined orography and the faces of the triangular cells are tangential to the surface of a sphere. The height levels gradually relax to a horizontally uniform height towards the top layer, which is depicted in Figure 3.3.

The interface of adjacent vertical cells is called half level and the center of the vertical cells is called full level. The amount of height layers can be defined in the model setup. For this thesis, setups with 90 and 120 height layers were

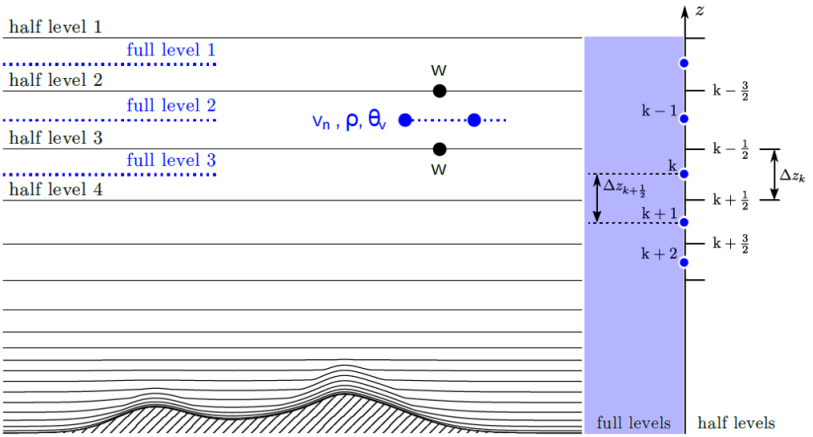

Figure 3.3: Height level structure of ICON. At the surface, the level height is defined by a predefined orography. With ascending height, the levels are gradually equalized to form horizontally uniform height layers. Index 1 is assigned to the TOA layer and index n is assigned to the surface layer (with n height layers defined in the model setup). Figure taken from the ICON Tutorial 2023 (Prill et al. 2023).

used with the latter being the current operational amount of layers used by DWD for their global numerical weather prediction. The explicit height of the individual atmospheric layers cannot be directly set, but the TOA height can be defined in the setup. Towards the top of the atmosphere, ICON uses Smooth Level Vertical (SLEVE) coordinates to achieve model levels of same height for higher altitudes (see Prill et al. (2023)). The squeezing of model layers above mountains is limited to prevent numerical instabilities. SLEVE coordinates can be controlled in the model setup.

3.1.5 Limited Area Operation Mode

It was already mentioned that ICON allows for the nesting of high resolution areas within a coarser grid to allow for small-scale forecasts in a target region while still keeping affordable computational costs. ICON also allows for a

Limited Area Mode (LAM) where no global calculations are performed. For this, the model is periodically provided with lateral boundary data at the edges of the defined area. These boundary data may be from a previous simulation (that encompasses the target domain) of a different grid size. It has to be in a predefined format that can be read in by ICON. As long as this format is kept, it does not matter where the data comes from.

The boundary cells of the LAM area are not just overwritten with the boundary data but a sponge layer of adjustable size is defined that gradually relaxes the boundary data into the domain in order to prevent reflections of the boundary data within the domain. This is done by adding a nudging term to the prognostic variables v_n (horizontal velocity normal to triangle edges), θ_v (virtual potential temperature), ρ (density) and q_v (specific humidity) via

$$\psi(t) = \psi^*(t) + \alpha_{nudge}[\psi_{bc}(t) - \psi^*(t)] \tag{3.7}$$

where ψ is the prognostic variable, ψ^* is the current value of the variable without nudging, ψ_{bc} is its boundary value and α_{nudge} is a coefficient that depends on the distance to the boundary of the LAM domain. Further details on the nudging can be found in the ICON Tutorial (Prill et al. (2023)).

3.2 ART Module

ICON handles the meteorological variables needed for atmospheric forecasting. For chemical processes, aerosols, aerosol microphysics and emissions the Aerosols And Reactive Trace Gases (ART) module can be used. This module was developed and is maintained by the Karlsruher Institut für Technologie in collaboration with Eidgenössische Materialprüfungs- und Forschungsanstalt (EMPA) and DWD.

ART enables the setup of chemical or aerosol tracers that represent specific particles, molecules, or particle classes (e.g. a certain class of pollen or chemical

species). Tracers are three-dimensional variable fields that are assigned an initial value at each grid cell of the host model (ICON) and then handed to ICON to be transported along with the rest of the air mass. The tracer can be initialized from any data source but needs to comply to a predefined structure. In each timestep of the model, the tracer is handed back to ART to be processed according to the chemical or physical description of it in ART. If a chemical tracer requires photolysis rates (J-values) to be calculated, ART contains the submodule Cloud-J that can calculate these online for the current state of the model. Since this is computationally expensive, ART also has implementations that use simplified representations of chemical reactions such as the LINearized OZone (LINOZ) scheme for stratospheric O_3 that will be explained in subsection 3.2.1. The set of tracers that are to be treated in the model simulation are collected and defined in a .xml file.

Some of the current use cases of ART are the operational pollen and Saharan dust forecasts by DWD, chemical and air mass origin forecasts for research aircraft campaigns, volcanic eruption modeling and trace gas emission calculations. In this work, ART is used to forecast O_3 as a chemical tracer using the simplified LINOZ scheme and to calculate solar irradiances at the surface, using an adapted version of Cloud-J.

3.2.1 Linearized Ozone Scheme: LINOZ

LINOZ (LINearized OZone) was developed by McLinden et al. (2000) with the aim to set up a parametrization for stratospheric O_3 processes that is computationally fast enough to be simulated online in atmospheric models. For most of the reactions mentioned in section 2.2, photolysis rates are required that would need to be calculated online if the reactions were to be solved in a full chemistry approach (a model setup that is also available in ART).

The authors of LINOZ sought to replace these full chemistry calculations with a first-order Taylor expansion. The tendency of an initialized O_3 field is expressed

as linear functions of ozone mixing ratio f, temperature T and overhead ozone column c_{O_3}:

$$\frac{df}{dt} = (P-L)^o + \left.\frac{\partial(P-L)}{\partial f}\right|_o (f - f^o) + \left.\frac{\partial(P-L)}{\partial T}\right|_o (T - T^o) + \left.\frac{\partial(P-L)}{\partial c_{O_3}}\right|_o (c - c^o_{O_3}) \tag{3.8}$$

Here, $(P-L)$ denotes the ozone tendency, the superscript "o" denotes climatological values. The partial derivatives are evaluated at f^o, T^o and $c^o_{O_3}$. As LINOZ was designed with stratospheric ozone changes in mind, tropospheric processes are neglected. In the model, this is translated to a fixed barrier at a geometric height of 10 km. Beneath this barrier, LINOZ tendency calculations are switched off, only atmospheric transport is performed and O_3 values are relaxed to 25 ppbv at the surface.

Using Equation 3.8 means for the calculation of O_3 that an initial O_3 field is required in combination with a table that contains climatological ozone tendencies $(P-L)^o$, f^o, T^o and $c^o_{O_3}$. The climatological tables can be created with the Photochemical Box Model, version 8.0 by Michael Prather that was made available through personal communication. A description of its working principles is given in Hsu and Prather (2010). This climatological table implies a major restriction for the use of LINOZ; It requires prior information on the chemical state of the atmosphere for the time to be modeled in order to create O_3 tendencies. For ozone depleting substances, an approximation of this chemical state can be extrapolated from past developments, as given e.g. by Gathen et al. (2021).

The LINOZ version in ART has an additional term that accounts for heterogeneous ozone destruction in the presence of PSC's that can be activated. This addition to LINOZ was first made by Sinnhuber et al. (2003). It can either use a lifetime assumption or an additional "cold" tracer field tr_{cold} with values between 0 and 1 that is initialized with 0 globally and a lifetime lt_{cold} of 10 days. In this thesis, the cold tracer parametrization is used. tr_{cold} represents

the activation of O_3 depleting substances that will remain activated for a time before undergoing deactivation. If the respective air mass is not close to the tropics (latitude > 45° North and South), the SZA is smaller than a predefined threshold of 85° and the temperature falls below 195 K, tr_{cold} is set to 1 and an additional loss term is introduced in Equation 3.8:

$$\left(\frac{df}{dt}\right)_{new} = \left(\frac{df}{dt}\right)_{LINOZ} + \left[f * exp\left(-t * tr_{cold}/864000s\right) - f\right] \tag{3.9}$$

Another modification is a correction of the VSLS amount in the stratosphere according to Hossaini et al. (2019). They reported a growth rate of stratospheric chlorine VSLS of 3.8 ppt/year in the years 2004 to 2017. This growth rate was added in the Photochemical Box Model that calculates the climatological tables by extrapolating this growth to the years modeled, 2022 and 2025. In addition to that, Gathen et al. (2021) reported an offset of 5 ppt for very short-lived bromocarbons that was also added to the calculations.

LINOZ does not conserve the mass of O_3 as it does not represent the reaction of O_3 with other species explicitly.

3.2.2 Cloud-J

Cloud-J is a radiative transport module that was originally designed to provide fast photolysis rate calculations for a 3-dimensional atmosphere for a given set of chemical reactions that could be performed online in atmospheric transport models. Its documentation is given in Bianz and Prather (2002), Prather (2015), Hsu and Prather (2010) and Hsu et al. (2017).

Cloud-J uses an a priori TOA solar spectrum and divides it into discrete, spectrally binned intervals that are chosen according to areas of similar photolysis rates for the main absorbing species of the respective wavelength interval, shown in Figure 3.4.

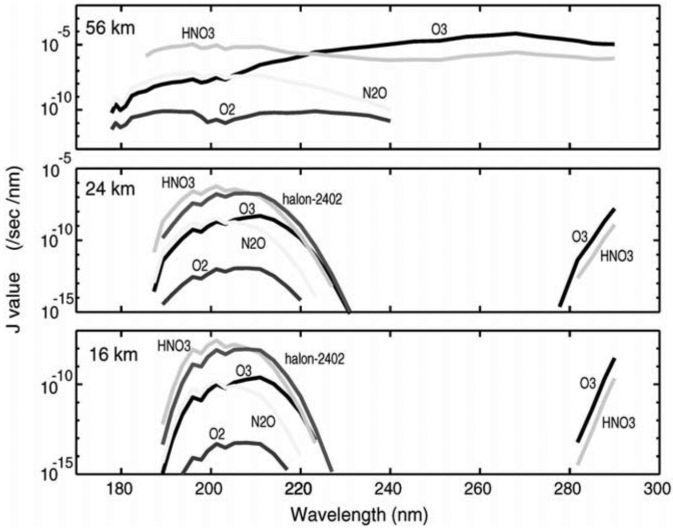

Figure 3.4: Photolysis rates (J values) of selected species in the UV range. The wavelength bins in Cloud-J were originally designed to represent areas of similar J value. For the O_3 Hartley bands ($\approx 190 - 230$ nm), the left and right flanks of the peak are grouped together to form composite bins. Figure taken from Bianz and Prather (2002).

For the UV range, the current standard Cloud-J version (as of 2025-12-01) uses 8 wavelength bins, the total spectral range of Cloud-J is 177 to 850 nm with a total of 18 bins. For each of the bins, it will then perform radiative transport for each atmospheric column that is contained in the host model. From ICON it receives temperature, pressure, SZA, liquid and ice water, relative humidity, O_3, CH_4 (if available) and the cloud fraction of each layer. For the aerosol load of the atmosphere, climatological tables are used.

As the name of the module indicates, a special interest was given to the handling of clouds as they are the main difficulty in modeling atmospheric radiative transport. Prather (2015) give detailed explanations on the treatment of clouds. The module allows for different accuracies (and, consequently, computational cost) on the treatment of clouds.

The calculation of radiative transport itself is done in an 8-stream-approach of Gauss points on a sphere at which the radiative transport is calculated. This ensures a treatment of atmospheric Rayleigh and Mie scattering as detailed in Section 2.1.6 while, again, limiting the computational cost of these calculations. The computational cost mainly originates from Mie scattering treatment.

3.2.3 Cloud-J Adaption

For this thesis, it was necessary to adapt Cloud-J. As mentioned in section 2.3, the calculation of the UV-Index requires the irradiance rather than the actinic flux required for the calculation of J values. The actinic flux A and the irradiance I are given by

$$A = \int_{\phi} \int_{\theta} F(\theta, \phi)\ sin\theta\ d\theta\ d\phi \tag{3.10}$$

$$I = \int_{\phi} \int_{\theta} F(\theta, \phi)\ cos\theta\ sin\theta\ d\theta\ d\phi \tag{3.11}$$

with $F(\theta, \phi)$ the solar radiance, ϕ the azimuth angle and θ the SZA. Cloud-J contains the calculation of the actinic flux, the respective routines were adapted to contain the $cos\ \theta$ to convert them to irradiance.

In addition, the wavelength bins do not match the defined wavelength area of the UV-Index, 280 - 400 nm. Therefore, they had to be adapted and their containing irradiances recalculated. The adaptations to the wavelength bins is shown in Table 3.3. This adaptation means that the code version of Cloud-J used in this thesis is not suitable anymore for the calculation of photolysis rates as the bin ranges do not cover the entire spectrum and no longer represent areas of similar O_3 J-Values.

Bin #	Cloud-J area 1	Cloud-J area 2	UV-Index area
Bin 10	221.5-233.0 nm	275.5-286.5 nm	280.0-286.5nm
Bin 11	215.5-221.5 nm	286.5-291.0 nm	286.5-291.0 nm
Bin 12	291.0-298.3 nm		291.0-298.3 nm
Bin 13	298.3-307.5 nm		298.3-307.5 nm
Bin 14	307.5-312.5 nm		307.5-312.5 nm
Bin 15	312.5-345.0 nm		312.5-345.0 nm
Bin 16	320.3-345.0 nm		320.3-345.0 nm
Bin 17	345.0-412.5 nm		345.0-400.0 nm

Table 3.3: UV range wavelength bins in original Cloud-J code and in the adapted UV-Index code version. The bins for the UV-Index calculation match exactly the range of 280-400 nm for which it is defined. Bins 10 and 11 originally were composite bins of the two flanks of the Hartley absorption bands. As the left flank is outside the UV-Index definition range, they were disentangled. The Cloud-J bin arrangement was originally described by Bianz and Prather (2002).

3.3 UV-Index Calculation

Cloud-J calculates irradiances for each of the defined wavelength bins, I_{bin}. These surface values can be inserted into Equation 2.35 by discretizing the equation into a sum:

$$UV - Index = k_{er} \sum_{bin=10}^{17} I_{bin}\, s_{er,bin} \tag{3.12}$$

with $k_{er} = 40 \frac{m^2}{W}$.

$s_{er,bin}$ is an averaged erythemal weighting factor for the respective Cloud-J bins. It is calculated by using the high-resolution solar spectrum provided by Meftah et al. (2018) which is given in a resolution of 1 nm:

$$s_{er,bin} = \frac{\sum_{\lambda,bin}\ s_{er}(\lambda) \cdot I(\lambda)}{\sum_{\lambda,bin} I(\lambda)} \tag{3.13}$$

The calculation of $s_{er,bin}$ weighs the contained wavelength area of each Cloud-J bin with its TOA spectral irradiance as given in the spectrum by Meftah et al. (2018). This yields UV-Indices for the surface. The calculation is performed offline after the model simulation has finished.

4 Ozone and UV-Index Forecast Results

After considering the theoretical background of atmospheric radiation transport, stratospheric chemistry and after explaining the model setup used in this thesis, this chapter first describes the simulations that were performed and then shows and discusses their results. The aim is to first validate the Ozone and UV-Index (UVI) calculations against similar data products. Then an analysis is performed to determine the dependence of the UVI on its influencing parameters, followed by a comparison to the operational UVI forecast by Deutscher Wetterdienst (DWD) and an analysis of the influence of the model resolution on results. Finally, differences between the ICOsahedral Nonhydrostatic Model (ICON) - Aerosols and Reactive Trace gases (ART) setup on different resolutions and the operational DWD forecast are analyzed with respect to the UVI influencing parameters.

The model simulations performed in the scope of this thesis are listed in Table 4.1. There were coarse resolution simulations at 40 km resolution to test the lon-term stability of the setup and its seasonal performance for the year 2022 and shorter simulations for the first months of 2025 at higher resolutions up to 2 km to resolve orography features and get better comparability to single measurement stations on ground. The years 2022 was chosen to be able to model seasonal timescales and the year 2025 was chosen to have model simulations available for the comparison to an aircraft measurement campaign that was conducted in the first months of 2025.

ICON Grid	Grid size [km]	Timeframe	Usage
R2B6 (global)	40	11.02.2022 - 31.07.2022	Proof of concept, seasonal differences
R2B6 (global)	40	11.02.2022 - 22.11.2022	Long-term stability
R3B7 (global)	13	01.01.2025 - 15.04.2025	Resolution comparison, Aircraft comparison, Boundary Data
R19B7 (Germany)	2	01.01.2025 - 15.04.2025	Resolution comparison, Station comparison, orography analysis,

Table 4.1: Performed ICON model simulations. The Usage column summarizes the applications of the simulations for this thesis. "Boundary Data" means that the R3B7 simulation was used for the generation of the lateral boundary data of the R19B7 simulation.

4.1 Model configurations

All of the simulations were initialized with DWD meteorological data and O_3 was provided by the Global Atmospheric Composition Forecasts data product provided in the Atmosphere Data Store of the Copernicus Atmosphere Monitoring Service (CAMS) (*Copernicus Atmosphere Monitoring Service (2021): CAMS global atmospheric composition forecasts.* 2025) under the CC-BY license. The O_3 fields provided by CAMS are in dry air mass mixing ratio (MMR), but ICON uses moist air volume mixing ratio (VMR). Therefore, the CAMS species need to be converted via

$$Species_{moist} = Species_{dry} \cdot \frac{1}{(1 + (M_{air,dry}/M_{wv}) \cdot RH)} \cdot \frac{M_{air,dry}}{M_{species}} \tag{4.1}$$

Here, $M_{air,dry} = 28.9647 \cdot 10^{-3} \frac{kg}{mol}$, $M_{wv} = 18.01528 \cdot 10^{-3} \frac{kg}{mol}$, RH is the relative humidity taken from the CAMS data set and $M_{species}$ the molar mass of the species, e.g. $M_{O_3} = 48.00 \cdot 10^{-3} \frac{kg}{mol}$.

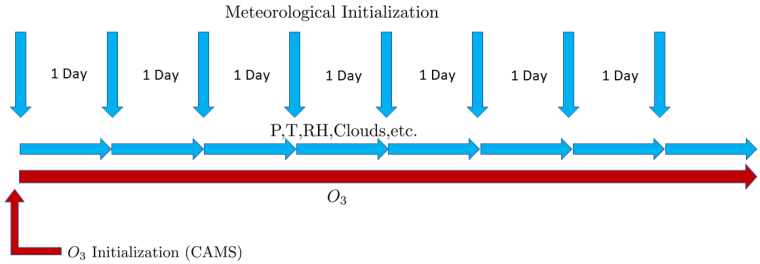

Figure 4.1: Cyclic Reinitialization (CRI) mode. The chemical tracers (here exemplary O_3) are initialized and then transported for the entire duration of the model simulation while the meteorological fields are reinitialized daily. This ensures that the state of the model keeps close to the observed state of the atmosphere.

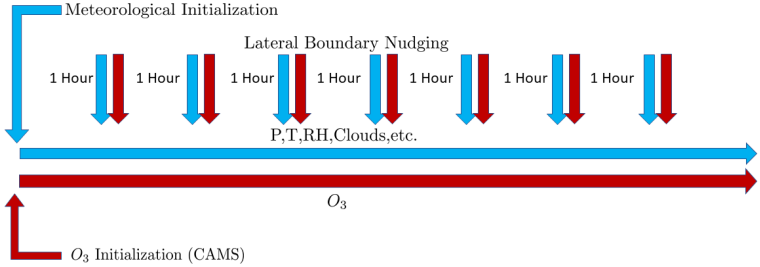

Figure 4.2: Lateral boundary nudging, used for the R19B7 simulation. After initialization, meteorological and chemical tracer fields (here O_3) are updated by lateral boundary data generated from the R3B7 model simulation.

The R2B6 simulations and the R3B7 simulation were performed in a Cyclic ReInitialization (CRI) Mode; the model is initialized every day at 00:00 UTC with external meteorological fields provided by DWD. ART tracers are passed on from the previous modeled day. This ensures that the state of the modeled atmosphere is close to reality and therefore that the model results can be compared to measurement data. It is different to typical routines as the one used for the R3B7 model simulation as it overwrites the field rather than nudging them towards the correct values. The CRI mode is depicted schematically in Figure 4.1.

In all simulations used in this thesis, the prognostic O_3 fields were coupled to ICON's radiation module ecRad to take them into account for the model state. For the CRI model simulations, this only has limited effect on the meteorology as the meteorological fields are reset to external analysis data each day.

4.1.1 R2B6 Model Simulations

Two R2B6 model simulations are evaluated in this thesis. They have the same CRI setup (see Figure 4.1) and both start on 2022-02-11. One of them runs until 2022-07-15 and contains irradiance calculations for the UVI by Cloud-J together with O_3 tendency updates by LINOZ. The second simulation runs until 2022-11-23 and only contains chemical forecasts with the aim to assess long-term stability of O_3. For the UVI simulation, the only chemical tracer used was O_3. The extended simulation until November also included a passive O_3 tracer that does not chemically interact but is only transported. LINOZ is used with its heterogeneous O_3 depletion scheme that uses a cold tracer that is described in Section 3.2.1.

Both simulations used 90 height layers with a Top Of Atmosphere (TOA) height of 75 km. The start date and end date were chosen to be a time frame of that contains stratospheric O_3 depletion in the northern hemisphere spring. The exact dates were chosen according to the availability of initialization data on the DWD server. The model generates output every 1.5 hours.

The DWD meteorological input fields are used as Incremental Analysis Update (IAU). A first guess file and analysis file are read into the model for the initialization with the first guess file shifted 90 minutes backward in time. The model will then simulate for a forward time according to this shift of 90 minutes and afterwards be pulled towards the analysis file at model start time. The intention of this setup is to reduce the noise of the analysis. A detailed explanation can be found in Prill et al. (2023).

4.1.2 R3B7 Model Simulation

The R3B7 simulation was initialized using first guess files for the meteorology provided by DWD. I starts at 2025-01-01 and finishes on 2025-04-15. As this grid is the operational global forecast grid of DWD, the settings for the operational weather forecast were adapted for KIT's HPC system. It simulates on 120 height levels up to a height of 75 km and, as mentioned before, interactive O_3 fields provided by LINOZ are considered in the radiation scheme ecRad. The model generates output files every hour. This setup uses Cloud-J for UV Irradiance calculations and LINOZ with the cold tracer setup for O_3.

The model results of the R3B7 simulation were converted to hourly lateral boundary data using the DWD ICON Tools (see Prill et al. (2023)) for the regional R19B7 LAM simulation. The simulation contains the tracers LINOZ O_3 and passive O_3. LINOZ O_3 is written out every hour, the passive O_3 tracer is only written as output every 8 hours.

4.1.3 R19B7 Model Simulation

The regional ICON-D2 grid is shown in Figure 4.3. The boundaries of the domain are nudged hourly with data from the global R3B7 simulation. Again, the CAMS O_3 are read in in the initial step. After initialization, O_3 values at the boundaries are nudged with the results from the R3B7 model simulation while LINOZ calculates the O_3 tendencies within the domain.

This model simulation is not reinitialized like the R2B6 or R3B7 simulations but continuously simulated for the entire period of the model simulation as depicted in Figure 4.2. As the radiation module requires the entire atmospheric column, the vertical resolution is kept at 120 height layers stretching to a top of atmosphere height of 75 km. This height resolution is different to the operational DWD R19B7 setup.

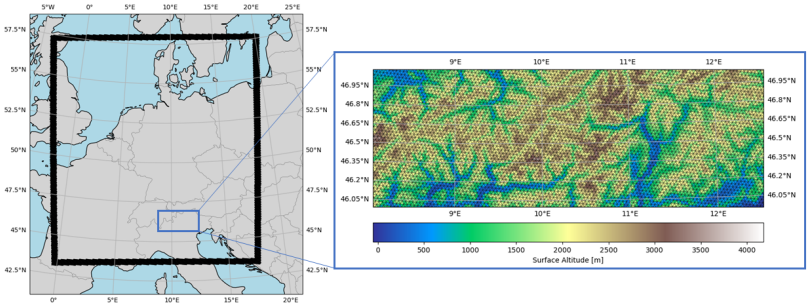

Figure 4.3: ICON-D2 grid with 2km resolution. The black rectangle on the left side of the figure shows the lateral boundary zone that is updated by the global R3B7 simulation every hour. The right side shows a zoom over a region in Northern Italy with the grid cells outlined and the orographic height shown as the color of the grid cells.

This simulation only uses O_3 as chemical tracer. It does not use the heterogeneous O_3 depletion scheme of LINOZ; as this is a regional simulation that is outside the polar region, polar heterogeneous ozone destruction does not need to be implemented in O_3 tendency calculations. The lateral boundary data that are nudged at the domain borders do, however, contain heterogeneous O_3 depletion effects as the previous global R3B7 simulation used the cold tracer LINOZ configuration.

4.2 Ozone Satellite Validation

In the first validation of the O_3 forecasts provided by LINOZ, they are compared to satellite data as this allows for a global estimate of the accuracy of the modeled data. The first modeling month is not considered in the analysis to allow the model to spin up. This pays respect to the fact that LINOZ calculates

O_3 tendencies, not the concentration itself and therefore requires some time to take effect.

The dataset used for validation is provided by the NASA Ozone Watch program (*NASA Ozone Watch: Latest status of ozone* 2025). This dataset consists out of 19 different satellite instruments that have been harmonized into one consistent dataset starting in 1979 up to two days before the present date (as of 2025-12-01). The data can be accessed directly via the website (*NASA Ozone Watch: Latest status of ozone* 2025). Total Column O_3 data in DU are available in a 1°x1° horizontal, 24 hours resolution. A quality assessment of the satellite data is given e.g. in Kroon et al. (2011) who state a Total Column Ozone (TCO_3) agreement for the OMI instrument that is part of the Ozonewatch program of ±20% in comparison to various O_3 measurement sources and even larger differences in the polar regions.

For this validation, the R2B6 simulation until November 2022 was selected as it provides the longest time range. Its resolution (40 km) is higher than that of Ozonewatch except close to the poles. Again, in this simulation, the O_3 field was initialized on 2022-02-11 and then modeled without additional chemical input until 2022-11-22 while the meteorology was reinitialized daily.

Figure 4.4 shows measurement and model data side by side. It demonstrates the capability of LINOZ to capture and reproduce dynamic features of atmospheric ozone as seen in measurement data. For the month of March that typically has a lot of dynamic effects on ozone in the northern hemisphere, the lower panel of Figure 4.4 shows that filaments breaking away from the polar vortex towards Europe can be reproduced in structure and total column values by ICON and LINOZ. Figure 4.4 shows an overestimation of TCO_3 in the second half of the modeled year.

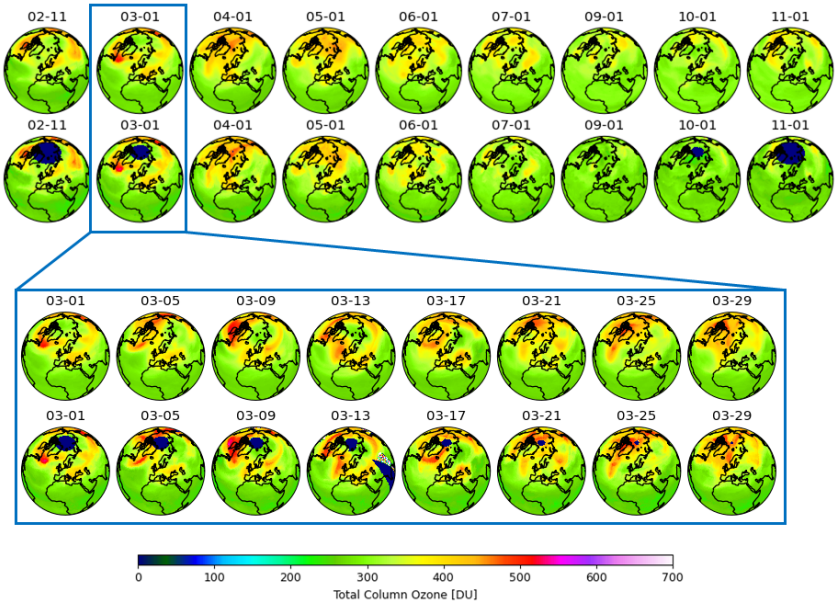

Figure 4.4: Comparison of modeled O_3 to satellite measurements. **Top:** Modelled (first row) and measured (second row) TCO_3 [DU] for the first days of each month (or model start) for February to November 2022. Blue areas are measurement gaps in the satellite data. **Bottom:** Zoom into March 2022 showing every 4th day, again modelled (first row) and measured (second row) TCO_3 [DU]. The first day of August is not shown because there are no satellite data for this date available. Satellite data taken from *NASA Ozone Watch: Latest status of ozone* (2025).

To quantify this overestimation, daily zonal mean differences in TCO_3 between satellite data and model data are shown in Figure 4.5 for the modeling period in 2022. TCO_3 is calculated via

$$\mathrm{TCO}_3 = \sum_{Levels} O_{3,Level} \cdot M_{O_3} \cdot p_{Level} \cdot h_{Level} / (R \cdot T_{Level}) \tag{4.2}$$

Here, $M_{O_3} = 48 \cdot 10^{-3} \frac{kg}{mol}$, $R \approx 8.314 \frac{J}{mol * K}$ is the ideal gas constant, p_{Level} the pressure of the level, h_{Level} the height of the level and T_{Level} is the temperature. The model provides $O_{3,Level}$ in volume mixing ratio.

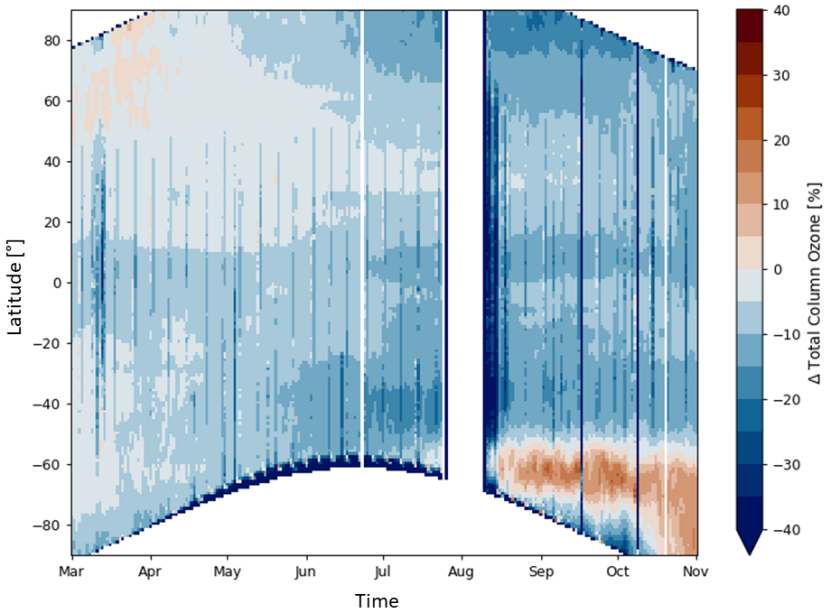

Figure 4.5: Zonally averaged difference of measurement to model TCO_3 for the year 2022 in % of difference. The white areas are measurement gaps in the satellite data. Negative values in the difference mean higher TCO_3 values in the model than in the measurements. Satellite data were accessed via *NASA Ozone Watch: Latest status of ozone* (2025).

Figure 4.5 confirms the overestimation of O_3 in the model compared to the measurement data with exceptions in Antarctic and Arctic spring. The northern hemisphere stays within ±5% agreement until the start of June. The quality of the model degrades with longer modeling time, which is to be expected considering that no new O_3 measurement information is provided to the modeled O_3 after initialization. This causes small errors to accumulate over time. At the start of June, four months after initializing the model, the first large structure with more than 10% deviation becomes visible in zonal mean differences in the southern hemisphere. From this analysis, 4 months of lead time can be taken as an estimate for the time in which the current LINOZ implementation can simulate while still being comparable to measurement data. Since no simulations

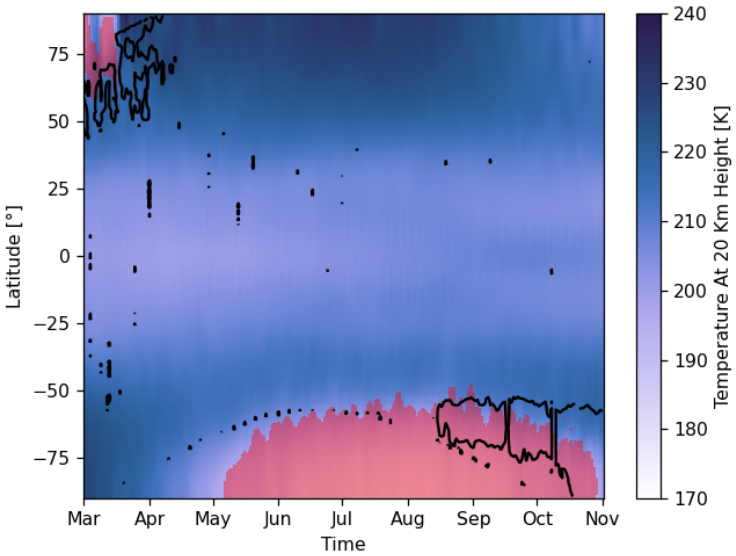

Figure 4.6: Zonal average temperatures of ICON at 20 km height and Δ TCO_3 contours (black lines) for 2022. The contour lines show the areas where the difference between measured and modelled TCO_3 switches signs as shown in Figure 4.5. The red shaded area marks latitudes where temperatures below 195 K occur at this height, at which point the polar chemistry term is applied in the LINOZ module.

were performed for longer than a year in this thesis, this statement cannot be generalized for time scales beyond that.

After the measurement gap in August, a large deviation around the Antarctic becomes prominent. Figure 4.6 shows the modeled averaged zonal temperature at a height of approximately 20 km. The temperature gradient visible in the Figure in the Antarctic from the middle of August to November does not match the area of TCO_3 difference sign change. This hints to an underestimation of the polar vortex area in ICON. The red shaded area indicates that the treatment of heterogeneous ozone destruction in LINOZ was active at all latitudes within the area of discrepancy.

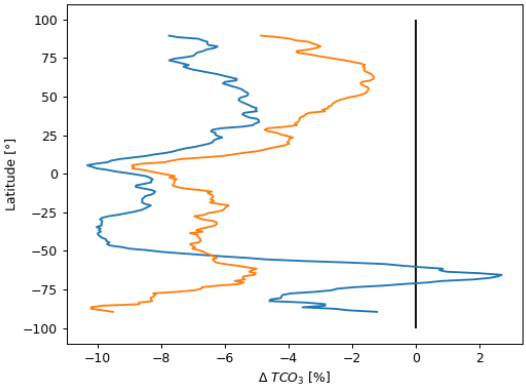

Figure 4.7: Temporally averaged zonal mean difference in TCO_3 between satellite measurements and model. The curves show the temporal mean zonal difference from 2022-03-01 to 2022-11-22 (**blue curve**) and from 2022-03-01 to 2022-05-31 (**orange curve**). This Figure is the temporal average of Figure 4.5. While the northern hemisphere stays within -5% deviations, the southern hemisphere, especially towards the poles, shows greater deviations between satellite data and model.

Figure 4.7 shows the average zonal differences for the two R2B6 model simulations. The switch in sign for the southern hemisphere is a consequence of the model underestimation for latitudes around 65° South after August 2022. For the northern hemisphere, the short term simulation reaches better agreement with the measurements than the simulation until November 2022. All of the zonal average deviations between model and satellite measurements found in this comparison are smaller than the deviations given by Kroon et al. (2011) for the satellite instrument itself with respect to reference data.

The conclusions drawn from the comparison of LINOZ O_3 model calculations to satellite data are:

- ICON captures the dynamic structure of the polar vortex well. This leads to high agreements of TCO_3 values.

- Modeled O_3 reaches an agreement within 5% to satellite data for a forecast lead time of up to 4 months in the northern hemisphere and within 10% for the southern hemisphere

- There is a general overestimation of TCO_3 by the model with exceptions in the Antarctic region.

4.3 Ozone Sonde Validation

The satellite comparison shows a global modeled overestimation of TCO_3. To gain information on the height layers where this overestimation occurs, radio sonde measurements are used. Ozone sonde data was accessed via the Network for the Detection of Atmospheric Composition Change (NDACC) Public Data Access (*NDACC - NASA LaRC* 2025).

Ozone Sondes at Neumayer Station (29.2 m above sea level), Ny Alesund (11 m above sea level) and Hohenpeißenberg (977 m above sea level) were used as reference in this thesis. The first two were used in order to compare polar

Figure 4.8: Ozone sonde stations used for comparison. The stations were selected to allow for a comparison in polar regions and the region of primary interest, Central Europe.

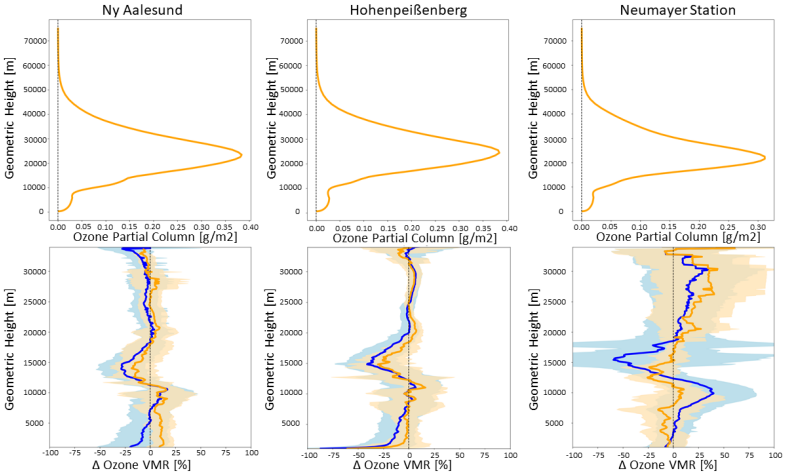

Figure 4.9: Ozone sonde measurement to model comparisons for 2022. The three columns show data for the three sonde locations that were considered for the comparison. **Orange** curves show the temporal mean over March to May 2022, **Blue** curves show the temporal average from March to November 2022. **Top:** Modeled partial O_3 columns in g/m^2 of each model height level. This quantity was chosen to show the contribution of the respective height levels to the total O_3 amount. **Bottom:** Relative differences between measurements and model as temporal mean, with the standard deviation as shaded area. As ozone sondes do not reach the full modeled atmospheric height, these plots end at 34 km height.

air while Hohenpeißenberg, located in the foothills of the Alps in Germany, is a Central European station that lies within the area of main interest. The stations are shown in Figure 4.8. For the comparison with ozone sonde data, again the R2B6 2022 simulation until November was taken for the comparison. The model data were matched temporally and spatially to the ozone sonde data with the nearest neighboring cell.

The comparison to ozone sonde data is shown in Figure 4.9. The top row shows the atmospheric height profile of ICON-ART level O_3 content in g/m^2 to show the contribution of the respective height levels to TCO_3. As can be seen, heights between 15 and 34 km have the largest contributions to TCO_3. Tropospheric

O_3 has only minor contributions. The calculation of the differences used the equation

$$\Delta O_3[\%] = \frac{O_{3,Sonde} - O_{3,Model}}{O_{3,Sonde}} \tag{4.3}$$

For all three measurement sites, the 4-month average is closer to the measurement profiles than the 10-month average. Considering the contribution of the respective heights to the TCO_3 values, this is in accordance to the results from the satellite comparison in the northern hemisphere.

The comparison of model O_3 values to ozone sonde data in Figure 4.9 shows an overestimation of the modeled O_3 around 15 km height for the three stations. The temperature profiles in Figure 4.10 show no differences in this height area. However, this is the height area where Very Short Lived Substances (VSLS) have a prominent role in O_3 depletion, as was explained in Section 2.2.4. Though corrections were applied to the LINOZ table to most recent measurements as explained in Section 3.2.1, there may still be an underestimation of their effect. The area between 13.4 and 17.8 km height (model levels 36-45) contributes $16.7 - 20.1\%$ of TCO_3 in the model simulations. A deviation of 25% as visible in Figure 4.9 in this area would therefore cause a total deviation of 4-5% in TCO_3. This matches the differences found for the northern hemisphere in the satellite TCO_3 comparison shown in Figure 4.7.

For the Antarctic Neumayer Station, the ozone sondes show a pronounced modeled O_3 underestimation at heights above 20 km and around 10 km. This, again, matches with the satellite comparison. Neumayer Station is located at 70.62° South which places it into the region of mismatch identified in Figure 4.6. The TCO_3 mean difference between model data and Ozonewatch satellite data for the time frame 2022-03-01 to 2022-05-31 is $-4.8 \pm 6.1\%$, which is close to the latitudinal mean (see Figure 4.7). It is within the area where temperatures below 195 K occur. This means that the polar chemistry loss term in LINOZ that was described in Section 3.2.1 is activated for parts of the air masses within this region.

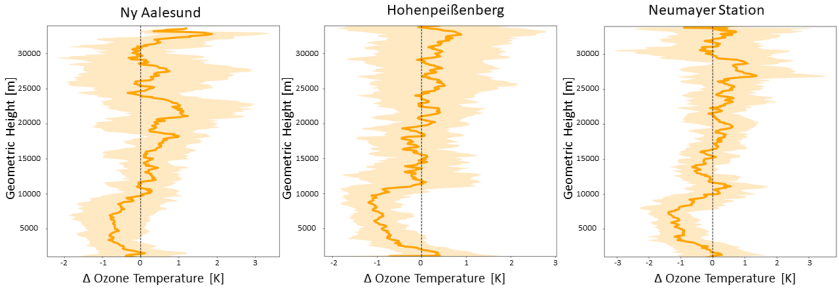

Figure 4.10: Temperature difference between ozone sondes and model. The curves show the differences in Kelvin, averaged over March to May 2022. The average difference between ozone sondes and model stays below ±2 K for all three measurement stations.

This temperature threshold is, however, just a coarse representation of the chemical processes that it represents. The deviations between model and measurement in the Antarctic showcased by the Neumayer Station comparison can be interpreted as proof that the polar chemistry treatment of LINOZ in its current state has only limited validity. One way to increase the accuracy could be to introduce a variable temperature threshold for the polar chemistry term activation. Drdla (2012) propose a variable threshold that depends on H_2O, sulfate aerosol surface area density and altitude. This would represent the O_3 depleting mechanisms described in Section 2.2 more accurate.

The profile comparisons show small deviations between measurements and model results in the troposphere (below 10 km height) with the exception of near-surface comparisons at Hohenpeißenberg. In this height region, no chemical interaction is taken into account, O_3 is only transported and relaxed at the surface to 25 ppbv. Figure 4.9 shows that the contribution to TCO_3 from these heights is small in comparison to the stratosphere, therefore these discrepancies are not relevant for radiation calculations.

From this comparison, the conclusions drawn are

- LINOZ overestimates O_3 at heights from 12-18 km. This error may arise from erroneous VSLS treatment.

- Deviations between modeled and measured TCO_3 of up to 5% may origin from this height area.
- The polar chemistry treatment of LINOZ can only partially represent real polar O_3 chemistry.
- Tropospheric O_3 can be represented well enough for radiation calculation.

4.4 Aircraft Validation: ASCCI Campaign

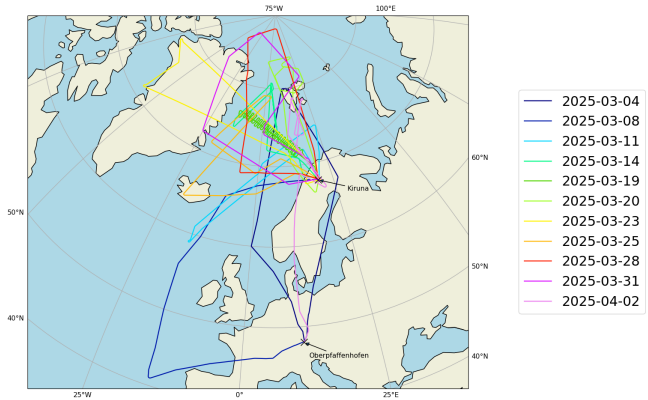

Figure 4.11: Flight paths of ASCCI campaign evaluated in this thesis. The legend shows the date of the flights displayed on the map. The majority of flights were based at Kiruna, Sweden.

Ozone sondes provide only limited horizontal resolution in higher altitudes. To get a better understanding of the O_3 forecast quality in the lower stratosphere and to better understand the validity of LINOZ O_3 forecasts in polar regions, measurements of the ASCCI aircraft campaign were used.

The Arctic Springtime Chemistry Climate Investigations (ASCCI) campaign (see Andreas Engel and Björn-Martin Sinnhuber (2025)) was conducted between

December 2024 and April 2025 using the High Altitude and Long Range Aircraft (HALO) that is operated by Deutsches Zentrum für Luft- und Raumfahrt (DLR).

The scientific topics addressed by the campaign as stated on its webpage (Andreas Engel and Björn-Martin Sinnhuber 2025) were:

- Inter-annual variability of Arctic lower stratospheric ozone depletion and the implications for radiative forcing and surface climate impacts of ozone recovery

- High latitude stratosphere-troposphere exchange and the structure of the high latitude tropopause

- Short-lived climate pollutants (ozone, aerosols) and their precursors in the Arctic mid and upper troposphere

The campaign included flights from Oberpfaffenhofen, Germany and from Kiruna, Sweden where most of the research flights were based from. For this evaluation, a total of 11 flights between March 4, 2025 and April 2, 2025 are considered. The individual flight paths can be seen in Figure 4.11. The majority of the measurement data were taken in the polar lower stratosphere. HALO provides onboard instrumentation that, among other quantities, measure temperature, pressure, speed and position.

For the comparison of O_3, in-situ measurements of the Fast AIRborne Ozone instrument (FAIRO) (documentation under Obersteiner (2025), gitlab repository *FAIROmeta · GitLab* (2025)) onboard HALO were used. This instrument provides measurements in an interval of approximately 4 seconds.

The global R3B7 model simulation from January to April 2025 with a resolution of 13 km was used to compare to the instrument data. For this, the FAIRO measurement data were averaged temporally over 30 seconds. This averaging interval was chosen with respect to the maximum measured horizontal aircraft

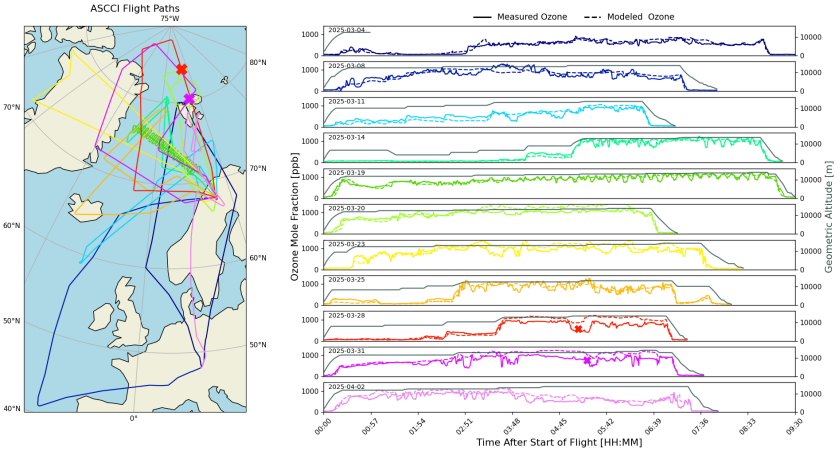

Figure 4.12: Comparison of modeled O_3 to aircraft measurements. **Left:** Flight routes of the HALO aircraft. The colored crosses mark positions of pronounced model O_3 overestimation. **Right:** O_3 measurements (solid colored lines) and modeled values (dashed colored lines) in ppb and geometric height (solid grey) of single flights for time after start of flight. The positions marked with crosses indicate measurements at the flight position with same mark on the left.

velocity of 276 m/s; After 30 seconds, the aircraft has passed a maximum of ≈ 8.3 km. While the temporal resolution of the model output (1 hour) is much bigger, this gives the averaged measurement data a spatial spread that is still smaller than one grid cell. The modeled O_3 data are matched by nearest neighbor in space and time to the measured values.

Figure 4.12 shows the O_3 measurements onboard the aircraft and the model results matched to the flight paths. The height of the airplane is also shown for the flight paths. The aircraft was typically flying between 10 and 14 km height which is at the lower end of the area where modeled O_3 overestimation is visible in Figure 4.9. Overall, a high agreement between the measurements and model results is visible. Looking e.g. at the O_3 flight profile for the flight on March 19 (solid green in Figure 4.12) that had a serpentine flight path, the matched model results are capable to reproduce the O_3 fluctuations due to this flight pattern with few exceptions. The average of the difference between

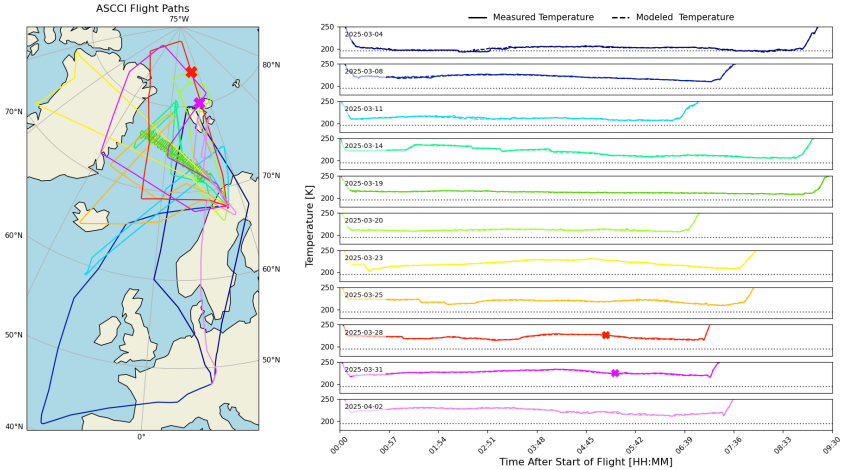

Figure 4.13: Comparison of modeled temperature to aircraft measurements.**Left:** Flights of the HALO aircraft. **Right:** Temperature measurements (solid colored lines) and modeled values (dashed colored lines) in Kelvin. Additionally, a dashed line shows the temperature threshold of 195 K for the activation of the polar chemistry term in LINOZ. This plot contains the same position marks as shown in Figure 4.12.

measurement and model in % for all flight paths combined is $\approx -5.9\%$, an overestimation of the model results. This matches the overestimation found in the previous section.

The marks in Figure 4.12 and Figure 4.13 signify areas of largest disagreement between model and measurement with an average overestimation of the model by $\approx 20\%$ for March 28 and $\approx 23\%$ for March 29. These flights were conducted on routes that reached to latitudes above 80° North, close to the Pole.

In order to assess whether this may have arisen from the heterogeneous polar chemistry treatment in LINOZ, Figure 4.13 shows the temperature of measurements and model for the flight paths. The temperatures of aircraft measurement and model are in very good agreement and constantly above the LINOZ polar chemistry threshold for the aircraft flight heights. Figure 4.14 shows the lowest temperature that occurred during the modeling time from January 1 to April 15,

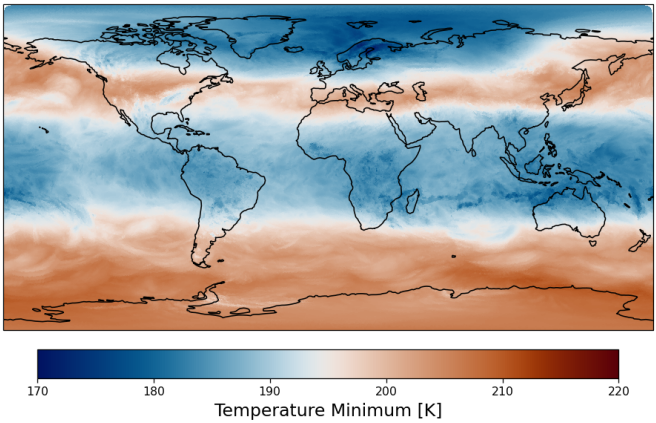

Figure 4.14: Lowest temperatures in the R3B7 model simulation between January and April 2025 between 10.5-35 km height. The color scale was chosen to have the 195 K LINOZ polar chemistry threshold as center values.

2025 for all grid cells and heights in the lower stratosphere between 10.5-34 km. It shows that the polar chemistry threshold is crossed at least once for almost the entire region around the North Pole in the lower stratosphere. This means that the heterogeneous loss of O_3 was active in LINOZ. Again, this is a hint that the representation of polar O_3 chemistry in LINOZ has only limited validity and has to be refined further to consistently model polar O_3 concentrations.

The conclusions from this comparison are:

- The LINOZ setup used here has a good agreement for the lower stratosphere with measurement data with exceptions at high latitudes.
- The modeled temperatures have high agreement to the temperature measurements of the aircraft.
- Ozone concentrations in mid latitudes between 40° North and 80° North consistently agree with measurements in the lower stratosphere. For

higher latitudes, discrepancies occur for parts of the measurements taken.

4.5 UV-Index: Satellite Comparison

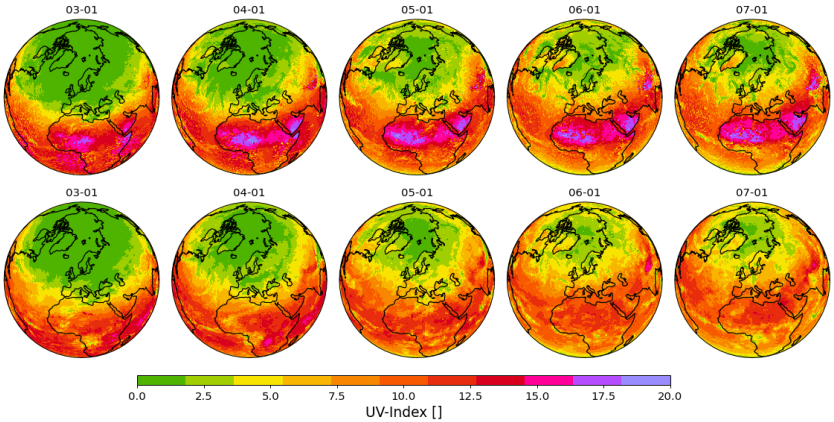

Figure 4.15: Model and satellite measurement UVI values for the first days of each month from March to July 2022, centered over Europe. The UVI is given as maximum value of the day. **Top:** Model data from ICON-ART, **Bottom:** CERES satellite data. Modeled UVI values and satellite data show distinct differences in Northern Africa and the Arabian Peninsula.

After assessing the quality of O_3 forecasts, the analysis of modeled UV-Index (UVI) can be conducted. To get an overview of the modeled UVI accuracy, satellite data provided by the CERES satellite instruments is used. The Clouds and the Earth's Radiant Energy System (CERES) project is described by Loeb et al. (2018) and Wielicki et al. (1996). The project consists of 7 CERES satellite instruments (*Instruments – CERES* 2025) with 6 of them currently active. The instruments have three output channels at 0.3-5 μm (SW), 0.3-200 μm (TOT) and 8-12 μm (WN).

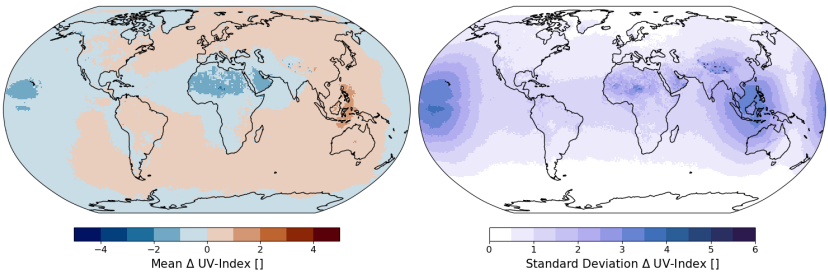

Figure 4.16: Time averaged UVI difference between satellite measurement and model, mean (**left**) and standard deviation (**right**). The measurement values are taken from the Syn1Deg data product of the CERES project. The data is averaged over the time span 2022-03-01 to 2022-06-31.

For this analysis, the Syn1Deg Level 3 data product (Doelling et al. 2016) with spatial resolution of 1° and hourly temporal resolution is used. It contains the surface UVI as data variable. Su, Charlock, and Rose (2005) explain the process of the UVI calculation from the satellite data and give an estimate of its accuracy of -26% to +16%.

For the comparison, the 2022 R2B6 model simulation with 40 km horizontal and 3 hours temporal resolution was used as it offers the longest time frame for validation. The surface UVI from model data was calculated from output by Cloud-J according to the method given in Section 3.3 in post processing. The results were then matched by nearest neighbor to the satellite data.

Modeled UVI values are available for the time period March to July 2022. A first overview over the results is shown in Figure 4.15. It shows the model UVI for the first day of each month in the top row and the corresponding results retrieved from measurements by CERES in the bottom row. The dynamic features of the two datasets show the same patterns, especially over Europe. Considering Northern Africa and the Arabian Peninsula, there is a visible disagreement between model and measurement with model overestimations of the UVI.

This is quantified in Figure 4.16. The plot shows the difference (satellite measurement - model) temporal average over the given time frame with the mean on the left and the standard deviation on the right. This means that first, the data are subtracted from each other and subsequently averaged in time. While the majority of the globe has an average agreement of ±1 with a standard deviation below 1, Northern Africa, the Arabian Peninsula, and single spots in the Himalayan region show greater deviations. These are areas with increased surface albedo, a quantity which together with its representation in the model is discussed in detail in Section 4.6. The standard deviation plot shows the highest values for latitudes close to the equator, which together with mountainous areas is also the region where the UVI is highest on average.

Figure 4.17 shows a separation of Figure 4.16 into the separate months to see whether there is a difference of matching accuracy between model and satellite UVI for different months. While the overestimation of the UVI in the Saharan region stays comparable over time, the underestimation of the UVI in the Indonesian region is reducing throughout the months. Also, the overestimation of the UVI in the Pacific becomes smaller for the later months of the year.

Section 2.3 listed environmental factors that influence the UVI. From the plots shown here, it is not possible to pinpoint the visible deviations to one of these factors, for this the data needs to be separated according to these parameters which will be done in the next section.

It was seen in the previous sections that the O_3 fields provided by LINOZ show the largest differences in polar regions. This does not transfer to a lower UVI agreement of modeled to measurement data in this region. The global and temporal mean difference from CERES measurement to model is -0.03 ± 0.86, meaning that the model overestimates the UV-Indices on average. Limiting this mean to latitudes towards the poles from 35°North/South (excluding the latitudes including the Saharan and Arabian region) gives a value of 0.01 ± 0.45. This would agree with the observed global overestimation of O_3 in the model, though the standard deviation is too large to assert a trend. Considering that the UVI is given in integer numbers, these values suggest that for latitudes

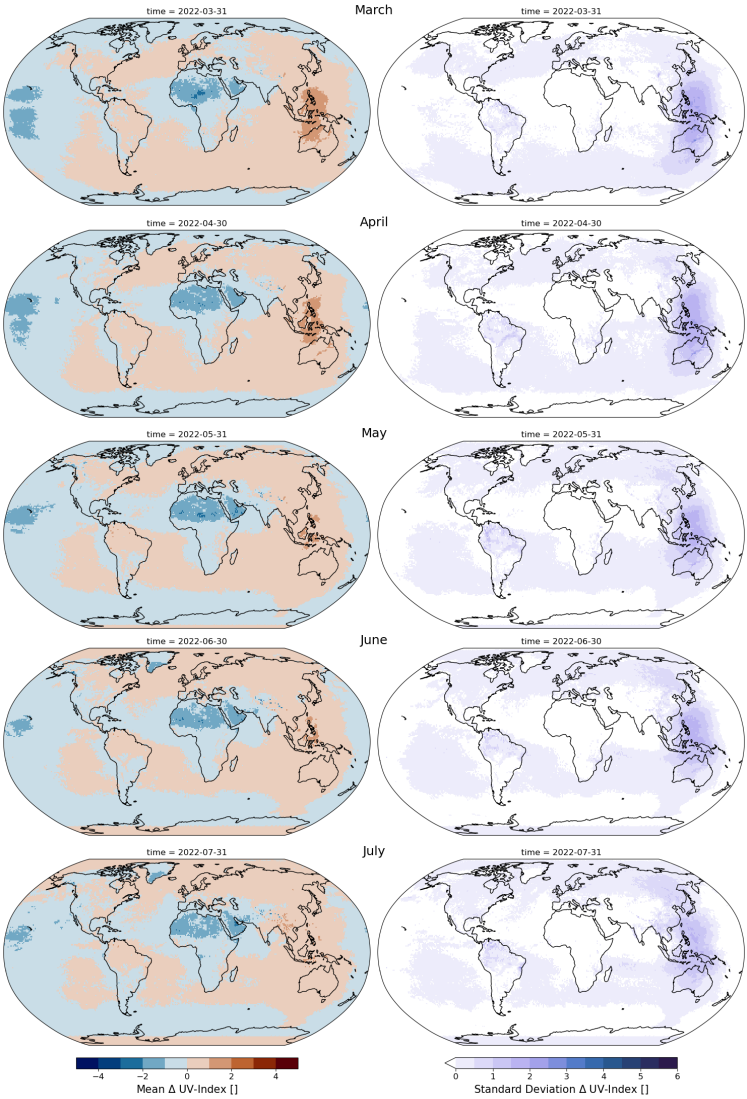

Figure 4.17: UVI difference of CERES satellite - model, mean (**left**) and standard deviation (**right**), averaged by month for the modeled time March to July 2022.

above 35°North/South the average UVI value is in agreement and for the entire globe, the average has an accuracy of ±1.

From the comparison to CERES satellite data, the conclusions drawn are:

- The overall structure and values of the modeled UVI agree with satellite measurements
- The majority of UVI data points have an agreement of ±1
- For low latitudes, the differences are larger than for higher latitudes

4.6 UV-Index Parameter Analysis

Figure 4.18 shows the total amount of data points used for the comparison between CERES satellite measurements and R2B6 2022 model simulation with 3-hourly output, separated into areas of UVI values. It shows the agreement of satellite and model data in a two-dimensional histogram that is colored logarithmically according to the amount of data points that have the respective agreement. This plot contains the same data as Figure 4.16. Summing up the plot yields that $\approx 70.3\%$ of the data are within ±1 agreement.

In order to assess the quality of the modeled UVI forecast with respect to the parameters that influence it, the modeled data are separated into intervals of parameter quantity and analyzed for trends. The parameters analyzed are:

- Solar Zenith Angle
- Cloud Cover
- TCO_3
- Aerosol Optical Depth
- Surface Albedo
- Surface Height

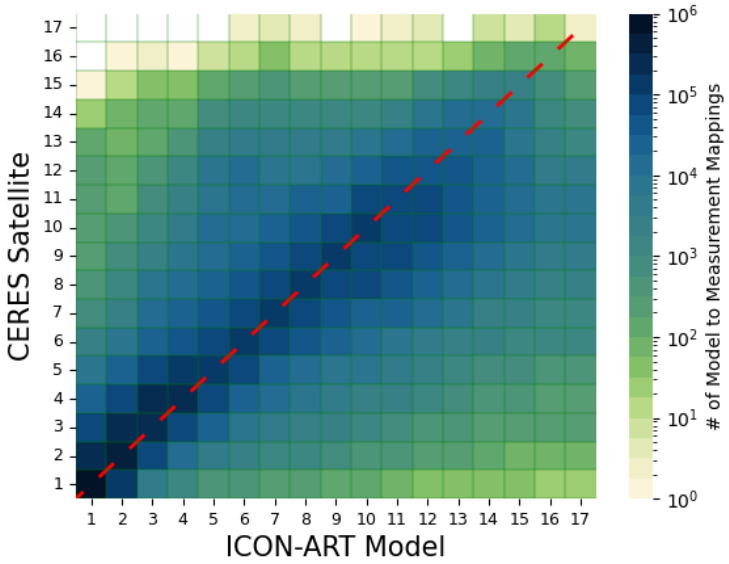

Figure 4.18: CERES satellite to model UVI comparison for March to July 2022. The modeled and measured UV-Indices are matched by nearest neighbor in space and time and aggregated by their agreement. If model and measurement have the same UVI value for a location, the result would be added to the diagonal entry of the respective UVI value. The colorscale for the aggregation is chosen logarithmic.

For the parameter analysis, the parameters are divided into six equidistant areas between the lowest and highest parameter value that occurs. Solar Zenith Angle (SZA), Cloud cover, TCO_3 and surface height values are taken from the model itself. The model simulations do not calculate Aerosol Optical Depth (AOD) or surface Albedo values within the model but rather use climatological input adjusted to the meteorological state, therefore the data used for the analysis are taken from the Global Atmospheric Composition Forecasts data product provided in the Atmosphere Data Store of CAMS (*Copernicus Atmosphere Monitoring Service (2021): CAMS global atmospheric composition forecasts.* 2025). If the difference of modeled UVI values to satellite UVI data depends on one of

the parameters, this indicates a misrepresentation of the respective influencing parameter in the model.

4.6.1 Solar Zenith Angle

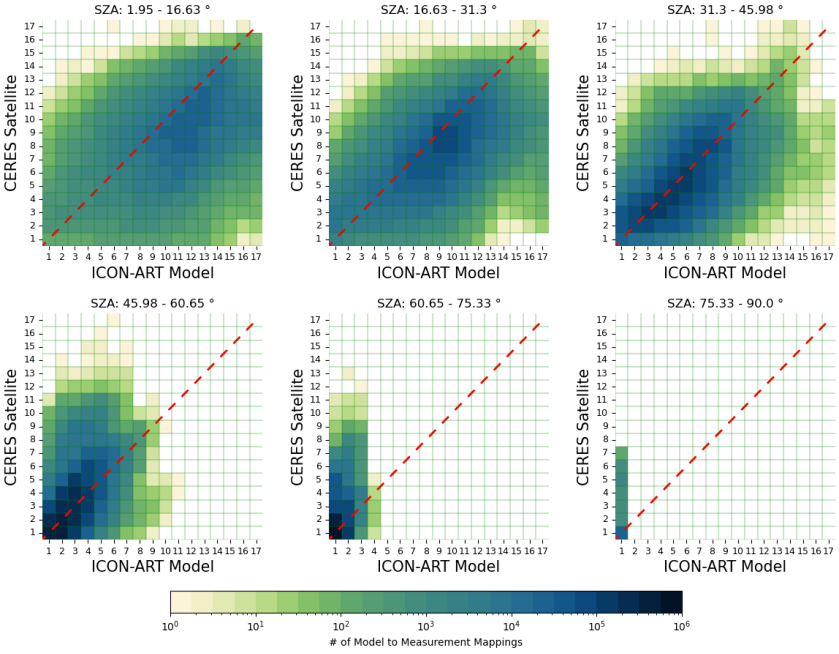

Figure 4.19: Solar Zenith Angle dependence of UVI: CERES satellite to model values comparison. The UVI calculation includes the cosine of the Solar Zenith Angle.

The dependence of the UVI on the Solar Zenith Angle (SZA) is shown in Figure 4.19. The calculation of Irradiance (and therefore the UVI) contains the cosine of direct solar radiation. Therefore, a reduction of UVI values with increasing SZA can be expected. Figure 4.19 shows this together with a slight overestimation of UVI values by the model for low SZA. This overestimation is also quantified

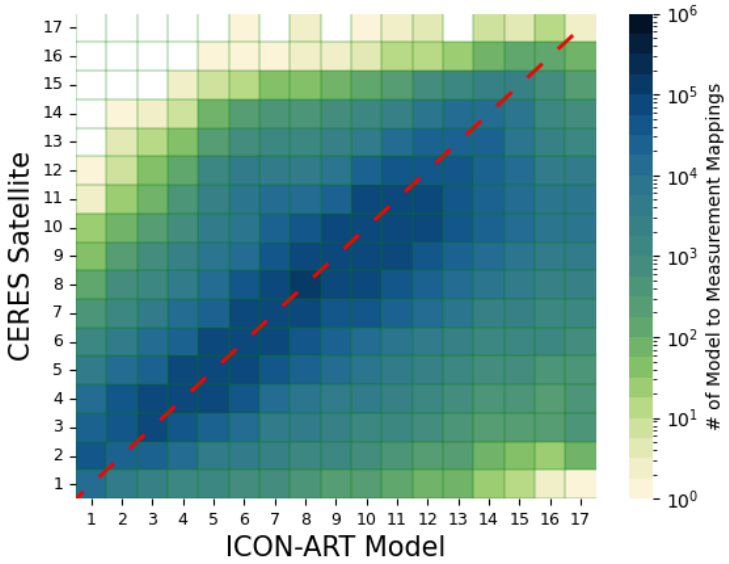

Figure 4.20: CERES satellite to model UVI comparison for March to July 2022, restricted to SZA < 45°.

in Figure 4.26 via the mean values of model and satellite data per bin and is less visible for higher SZA values. For very high values, the model is restricted to low UVI values while the CERES measurements still show a spread up to values of 7 for SZA values above 75.33°. These differences could arise from the fact that CERES has a pixel size of 1°x1° which is significantly larger than the 40 km resolution of the model except close to the poles. This causes solar illumination differences between the CERES data pixels and the respective model cells, especially at times and areas of low illumination, i.e. close to sunset or dawn.

This parameter dependence of the UVI on SZA introduces the spread along the 1:1 line in Figure 4.18. Restricting the analysis to SZA values below 45 (i.e. the first row of Figure 4.19) changes Figure 4.18 to Figure 4.20. For the

following parameter analyses, this restriction is applied in order to highlight the dependence of the UVI on other parameters.

4.6.2 Cloud Cover

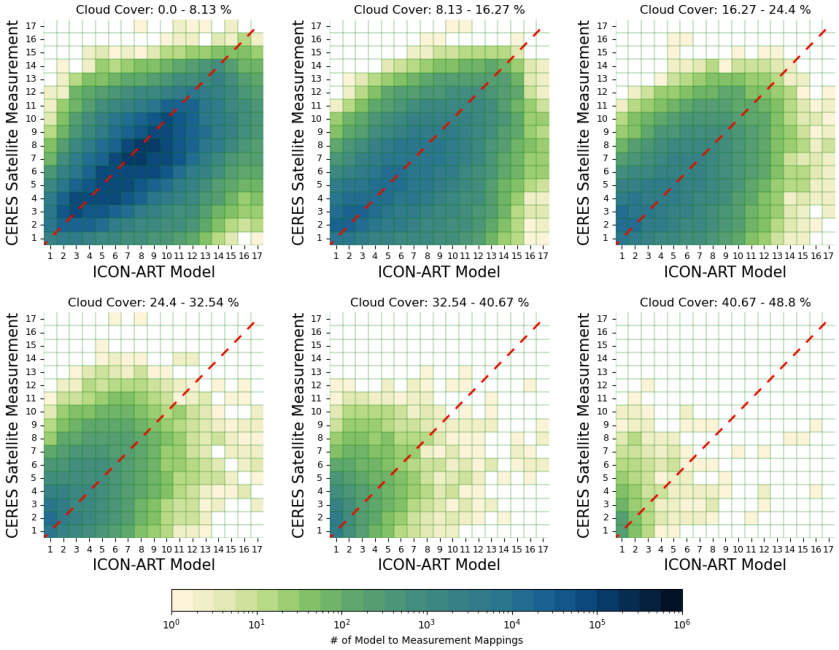

Figure 4.21: Separation of CERES satellite to model UVI data by cloud cover.

Figure 4.21 shows the UVI dependence on cloud cover. Here, cloud cover denotes the mean percentage of cloud coverage of all vertical grid cells above the respective surface location. For low cloud cover, modeled UVI values show a slight overestimation which is not visible for higher cloud cover. As expected, UVI values become smaller with increasing cloud cover.

This figure demonstrates that small mismatches of cloud cover forecasts can have a pronounced effect on the UVI forecast; If the model assumes a grid cell to be only slightly clouded (top left of Figure 4.21) but in reality it is strongly clouded (bottom right of Figure 4.21) or vice versa, the UVI forecast values will show strong differences to measurement data. For a resolution of 40 km in the model, these cloud cover differences between measurement and model can average out but going to higher resolutions can cause a stronger mismatch as cloud field mismatches cannot be prevented in models. This thesis aims to assess the overall UVI forecast accuracy of the ICON-ART setup, therefore these mismatches are not filtered out in the analysis.

4.6.3 Total Column Ozone

Figure 4.22 shows the dependence of the UVI model and measurement data on TCO_3 in Dobson Units. As expected, an increase of TCO_3 leads to a decrease of UVI at the surface.

From the previous comparison, an TCO_3 overestimation of around 5% was noted. This should lead to reduced UVI values in comparison to measurement data. As this does not show in the data, it is likely that the effect of this O_3 overestimation on UVI values is a small deviation in comparison to e.g. albedo mismatches which will be explained below or mismatches in cloud cover between model and measurements.

4.6.4 Aerosol Optical Depth

Figure 4.23 shows the dependence of measured and modeled UVI values on Aerosol Optical Depth (AOD) at 550 nm. The wavelength chosen here is not within the UV range of light, but for larger particles, scattering only has a weak wavelength dependence (see Section 2.6).

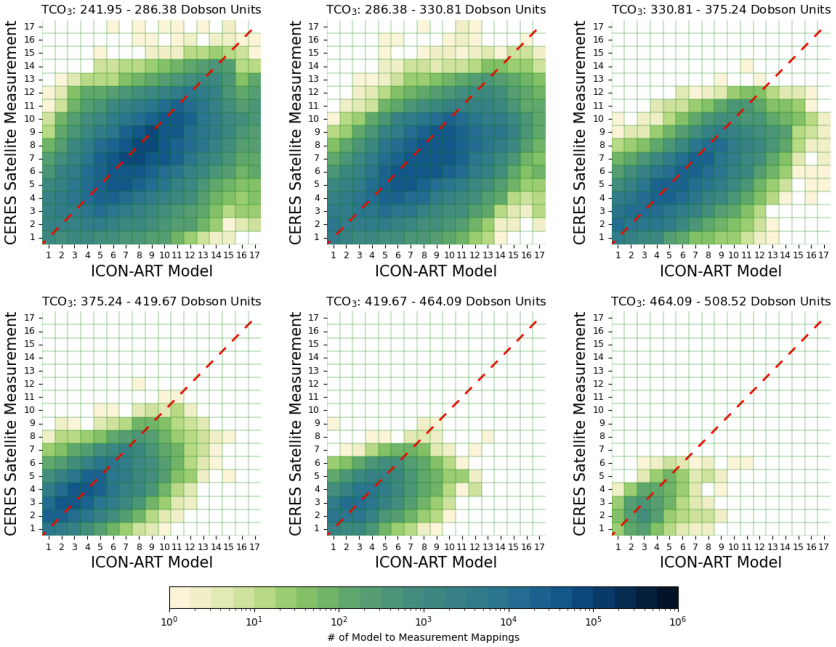

Figure 4.22: Separation of CERES satellite to model UVI data by TCO_3.

For low AOD values, model and measurement show a good agreement that turns towards an increasingly stronger overestimation of UVI values with increasing AOD. Cloud-J, the radiation module used to calculate the modeled UVI values, does not use interactive AOD but relies on climatological values. Cases in which the real AOD of the atmosphere deviates from climatological values, e.g. during Saharan dust events in Europe, cannot be caught in the model. This can be seen by the increasing mismatch between measurements and model for higher AOD values in Figure 4.23.

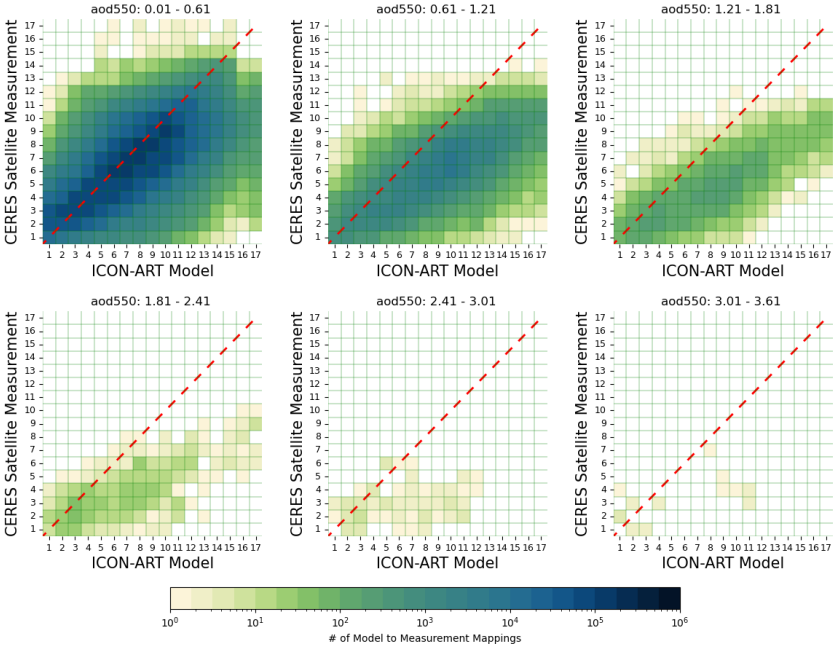

Figure 4.23: Separation of CERES satellite to model UVI data by AOD.

4.6.5 Surface Albedo

Figure 4.24 shows the dependence of the model and measurement UVI values on surface albedo. Separating data by albedo introduces a separation by location of the data points; High values occur in the Saharan Region, the Arabian Peninsula, in polar regions and in mountainous regions.

The first box contains areas with an albedo of 0.19. This includes low land areas and ocean surface. Figure 4.23 shows a separation of data points for higher albedo values in the bottom row. This is an example of selection of data points by region. As will be confirmed later by the comparison to ground measurement

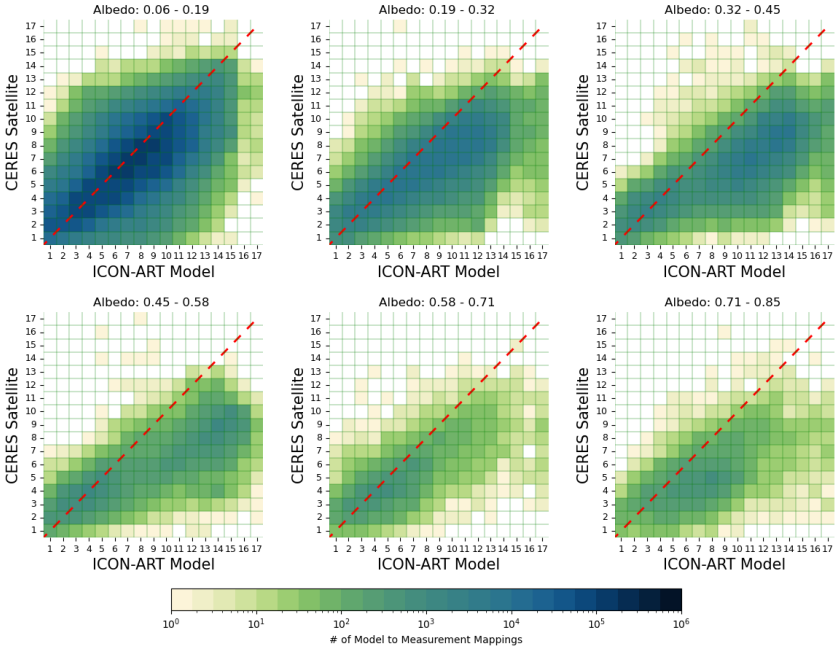

Figure 4.24: Separation of CERES satellite to model UVI data by surface albedo.

stations, UVI model forecasts display larger deviations for mountainous areas and Figure 4.15 shows a mismatch in areas with desert soil type.

Section 2.1 explains that albedo is a quantity that depends on the wavelength. However, UV albedo is normally not provided separately from visible albedo and the majority of data sets does not distinguish between different areas of wavelength, like the one presented by Riihelä, Jääskeläinen, and Kallio-Myers (2024). The albedo available in ICON has the range of 0.3-0.7 μm (Prill et al. 2023). Switching to a UV albedo could help clarify the dependence of the UVI on Albedo and decrease the UVI differences to measurement data for high albedo values.

4.6.6 Surface Height

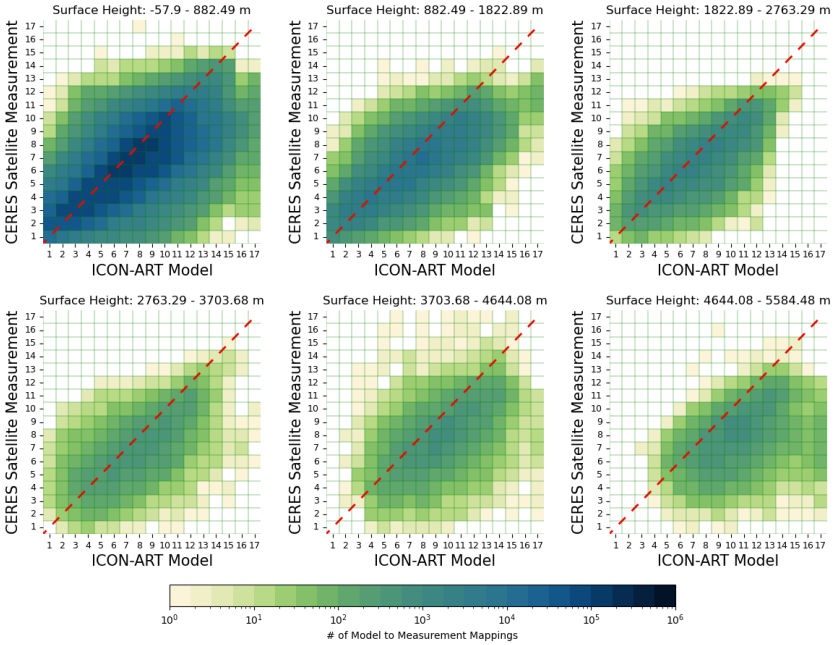

Figure 4.25: Separation of CERES satellite to model UVI data by surface height.

The separation of model and measurement UVI data by surface height is shown in Figure 4.25. UVI values increase with higher altitude. This effect is stronger for the modeled UVI values than for CERES satellite data which can be seen by the shift of the data for high altitudes in the bottom right of Figure 4.25 towards higher model values. The resolution of 1°x1° horizontally by the satellite data is likely too large to show the expected UVI increase with height accurately as this resolution is not well suited to resolve the steep orography in mountainous areas. This is, to a smaller degree, also true for the 40 km resolution of the model.

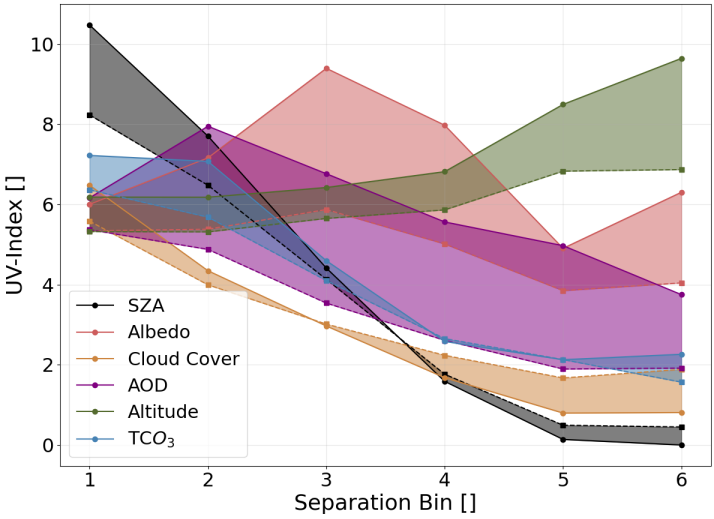

Figure 4.26: Summary of UVI parameter analysis. Each data point is the mean of ICON (solid lines) or CERES (dashed lines) UVI values for each of the 6 separated bins of parameter. The parameter edge values for each bin are listed in Table 4.2. These plots are a summary of the parameter analysis plots in this section to show trends of the mean UVI values along the parameter variations. When looking at the means when dividing the data by Solar Zenith angle (SZA, black curves), the curves both for ICON and CERES show the cosine dependency of the UVI values on this parameter. The size of the shaded area between solid and dashed lines indicates the difference between CERES and ICON.

4.6.7 Parameter Analysis Summary

Figure 4.26 summarizes the parameter analysis from the previous sections. For each of the six separations of the UVI data by equidistant ranges of influencing parameter, the average UVI values for ICON-ART and CERES data are plotted. The size of the shaded areas indicates the average agreement between ICON (solid lines) and CERES (dashed lines). Smaller shaded areas mean better agreement between CERES satellite data and ICON-ART. Again, for this analysis the data (except for the SZA comparison itself) were prefiltered for SZA<45°.

Parameter	Bin 1	Bin 2	Bin 3	Bin 4	Bin 5	Bin 6
SZA [°]	1 - 16	16 - 31	31 - 45	45 - 61	61 - 75	75 - 90
Cloud Cover [%]	0 - 8	8 - 16	16 - 24	24 - 33	33 - 41	41 - 49
TCO_3 [DU]	241 - 286	286 - 330	330 - 375	375 - 419	419 - 464	464 - 508
AOD []	0.01 - 0.61	0.61 - 1.21	1.21 - 1.81	1.81 - 2.41	2.41 - 3.01	3.01 - 3.61
Albedo []	0.06 - 0.19	0.19 - 0.32	0.32 - 0.45	0.45 - 0.58	0.58 - 0.71	0.71 - 0.85
Altitude [m]	-57 - 882	882 - 1882	1882 - 2673	2673 - 3703	3703 - 4644	4644 - 5584

Table 4.2: Parameter separation bin edges of the UVI parameter analysis shown in Figure 4.26. SZA, cloud cover, TCO_3 and surface altitude were rounded to integer numbers for better readability.

For SZA, TCO_3, cloud cover and altitude, clear dependencies of UVI values can be seen in Figure 4.26. For albedo and AOD, these trends are less pronounced and the differences between model and satellite UVI value are larger. Both of these quantities are external fields from CAMS data.

Cloud-J uses climatological tables for AOD, so it does not take into account single AOD events such as Saharan dust events. Implementing prognostic AOD into Cloud-J radiation forecasts could improve its validity and show a more definite dependency of UVI on AOD.

Table 4.3 shows the mean UVI values and their standard deviation for each separation bin shown in Figure 4.26. The separation bins had an uneven distribution of data points per bin. This arises from choosing equidistant separation bins, extreme values of e.g. albedo are only reached for small amounts of data points. However, as the standard deviations in Table 4.3 have similar values also for bins that contain small data samples, they can be assumed to be of similar stability.

Table 4.3 allows to define a variability of UVI values introduced by each of the influencing parameters as the difference between the maximum and minimum mean UVI value within separation bins for each parameter. The result values are shown in Table 4.4. They allow for an estimation of the importance of the respective parameter for the calculation of UVI values. The largest UVI variability is introduced by the SZA with an average variability of 9.2 ± 1.9, making it the most important influence quantity for the UVI. TCO_3, cloud cover

Bin #	SZA		Albedo		Cloud Cover	
	ICON	CERES	ICON	CERES	ICON	CERES
Bin 1	10.5 ± 2.8	8.3 ± 2.5	6.0 ± 2.8	5.3 ± 2.4	6.5 ± 2.8	5.6 ± 2.3
Bin 2	7.7 ± 2.7	6.5 ± 2.4	7.2 ± 3.2	5.4 ± 2.2	4.3 ± 3.1	4.0 ± 2.5
Bin 3	4.4 ± 2.2	4.1 ± 2.3	9.4 ± 3.6	5.9 ± 2.3	3.0 ± 2.7	3.0 ± 2.3
Bin 4	1.6 ± 1.2	1.8 ± 1.7	8.0 ± 4.7	5.0 ± 2.6	1.7 ± 2.1	2.2 ± 2.0
Bin 5	0.1 ± 0.4	0.5 ± 1.0	4.9 ± 3.1	3.8 ± 2.1	0.8 ± 1.5	1.7 ± 1.8
Bin 6	0.0 ± 0.0	0.4 ± 1.2	6.3 ± 3.1	4.0 ± 2.0	0.8 ± 1.8	1.9 ± 2.1
Bin #	**AOD**		**Altitude**		**TCO_3**	
	ICON	CERES	ICON	CERES	ICON	CERES
Bin 1	6.2 ± 3.0	5.4 ± 2.4	6.2 ± 3.0	5.3 ± 2.4	7.2 ± 2.6	6.4 ± 2.2
Bin 2	8.0 ± 3.3	4.9 ± 2.1	6.2 ± 2.9	5.3 ± 2.2	7.1 ± 2.7	5.7 ± 2.1
Bin 3	6.8 ± 3.7	3.5 ± 2.2	2.4 ± 2.6	5.7 ± 2.1	4.6 ± 2.4	4.1 ± 1.9
Bin 4	5.6 ± 3.7	2.6 ± 1.8	6.8 ± 2.7	5.9 ± 2.3	2.6 ± 1.7	2.7 ± 1.3
Bin 5	5.0 ± 3.2	1.9 ± 1.3	8.5 ± 2.6	6.8 ± 2.3	2.1 ± 1.4	2.1 ± 1.1
Bin 6	3.8 ± 3.2	1.9 ± 1.4	9.6 ± 2.5	6.9 ± 2.0	2.3 ± 1.1	1.7 ± 1.0

Table 4.3: Mean and standard deviation values for each separation bin value for ICON-ART and CERES data in units of UVI. The means were also shown in Figure 4.26. All values were rounded to one decimal.

Parameter	ICON-ART	CERES	Average
SZA	10.5 ± 2.8	7.9 ± 2.8	9.2 ± 1.9
TCO_3	5.1 ± 2.9	4.7 ± 2.4	4.9 ± 1.9
Cloud Cover	5.7 ± 3.1	3.7 ± 2.9	4.7 ± 2.1
AOD	4.2 ± 5.1	4.0 ± 2.7	4.1 ± 2.9
Albedo	4.5 ± 4.8	2.1 ± 3.1	3.3 ± 2.9
Altitude	3.4 ± 3.9	1.6 ± 3.0	2.5 ± 2.5

Table 4.4: Variability as maximum difference between two parameter bin UVI means for ICON-ART and for CERES in units of UVI. The last row shows the mean of the two variabilities. Values are calculated from the rounded values shown in Table 4.3

and AOD have similar variabilities. For albedo and altitude, the errors are almost the same size as the variablilities themselves.

The variability values allow for an interpretation of the low UVI mean of the first AOD separation bin in Figure 4.26. When considering Figure 4.23, it can be seen that the majority of data points is accumulated in this bin of lowest AOD

values. Three of the influencing UVI influencing parameters introduce a higher or similar variability on UVI values in comparison to AOD, therefore the mean value of this bin is forced towards the average UVI value of all data points. The influence of AOD on UVI values is superimposed by the other parameter influences.

A similar argument can explain the impact of the observed overestimations of 5% in TCO_3 by ICON-ART on UVI values. Table 4.3 shows that the mean UVI values of ICON-ART and CERES are within their respective error margins for each separation bin, which means that there is no significant increase in UVI values due to the TCO_3 overestimation. SZA, cloud cover and AOD variabilities on UVI values superimpose the variability introduced by TCO_3 and therefore its effect on UVI values.

The results presented in this thesis were derived from a data set in the time frame March to July 2022. In order to derive a more general validity of the parameter variability values presented here, other, longer time frames that include atmospheric phenomena that were not captured in the presented time frame could be combined with the results shown in this section. Regarding the size of the errors in Table 4.3, a larger model analysis time would also be desirable to achieve more robust variabilities.

The conclusions drawn from this comparison are:

- The variabilities on UVI values introduced by its influencing parameters in units of UVI are for SZA 9.2 ± 1.9, for TCO_3 4.9 ± 1.0, for cloud cover 4.7 ± 2.1, for AOD 4.1 ± 2.9, for albedo 3.3 ± 2.9 and for altitude 2.5 ± 2.5.
- The UVI effect of the overestimation in TCO_3 is superimposed by the variabilities of other UVI influencing parameters.

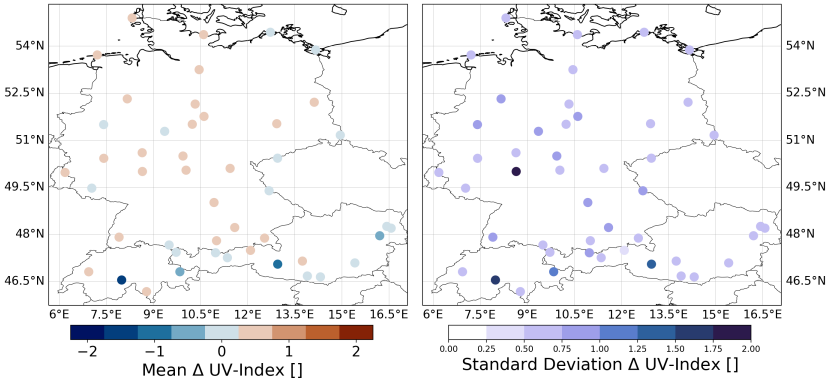

Figure 4.27: Comparison of model data to ground stations for January 01 to April 15, 2025. The graphs show the difference of ground station measurement to model UVI values, mean (**left**) and standard deviation (**right**) over the modeled time frame.

4.7 Ground Measurement Comparison

So far, only satellite UVI data was used for the comparison. With respect to the forecasting capability of ICON-ART, a comparison to individual ground measurement stations allows for an assessment of how accurate the UVI at single locations can be forecasted.

For this comparison, measurement data of stations by Bundesamt für Strahlenschutz (BFS) were accessed via the BFS Geoportal (*GEOPORTAL | Bundesamt für Strahlenschutz* 2025). The data is distributed under the "Datenlizenz Deutschland – Namensnennung – Version 2.0" license. In addition to that, measurement data for Austria were provided by Institut für Biomedizinische Physik, Medizinische Universität Innsbruck under the CC BY 4.0 license. These data from Austrian measurement stations were accessed via *Data access - WOUDC - World Ozone and Ultraviolet Radiation Data Centre* (2025). For four additional measurement stations in Switzerland, the data was made available by per-

Station Name	Station Altitude	Model Altitude	Model Albedo	UVI Difference
Jungfraujoch	3582 m	3396 m	0.699	−1.43 ± 1.64
Sonnblick	3106 m	2618 m	0.086	−1.12 ± 1.49
Zugspitze	2656 m	2233 m	0.044	0.11 ± 0.99

Table 4.5: Mountain peak station data. Model Altitude is the height of the respective model grid cell, Model Albedo is the albedo used for the calculation of UVI values and UVI deviation is the temporal mean and standard deviation of the difference between measurement and model for 2025-01-01 to 2025-04-15.

sonal communication with Laurent Vuilleumier, Federal Office of Meteorology and Climatology (MeteoSwiss), Payerne, Switzerland (see also Vuilleumier et al. (2021)). In total, 48 measurement stations were used for this comparison.

These measurement data were compared to the R19B7 model simulation from January to April 2025 that has a 2 km horizontal resolution, 120 height layers and hourly output. The model data were matched via nearest neighbour to the measurement station locations. The BFS measurement data contain daily maximum UVI values which is also the quantity communicated to the public. Therefore, this comparison uses daily maximum UVI values. For data from Switzerland, 30 minute interval averages were computed and then, as with the provided 30 minute averaged UVI data from Austria, daily maxima were computed.

The comparison between measurement stations and model data is shown in Figure 4.27. With the exception of the two measurement stations Jungfraujoch (46.55°N, 7.99°E, 3582 m altitude) in Switzerland and Sonnblick (47.05°N, 12.95°E , 3106 m altitude) in Austria that are located on mountain peaks, every station has a mean measurement to model difference between -0.75 and +0.75. Taking all measurement stations except Jungfraujoch and Sonnblick into account, the average difference between measurement and model is 0.27 ± 0.77, a positive value means a higher average in measurement data. 59.5% of the data points show exact agreement between measurement and model, 94.9% have an agreement of ±1 and 98.7% of ±2.

For the mountain peak measurement stations at Jungfraujoch, Sonnblick and a third station at Zugspitze (47.42°N,10.98°E, 2656 m height) in Germany that is included in the measurement data, the UVI influencing parameters that are specific to the locations are listed together with the difference between measurement and model for the specified time frame in Table 4.5. The model surface altitude at these locations is lower than the real height of the measurement stations. This is due to the size of the model grid cells that have a horizontal resolution of 2 km. Since the model height is lower than the real height, this parameter cannot account for the overestimated UVI values in the model. Both stations have higher albedo values in the model in comparison to Zugspitze, which could explain the UVI overestimations. Another possible explanation could be a systematic bias in modeled meteorological parameters, e.g. cloud cover due to the exposed position of the measurement stations.

Laurent Vuilleumier (MeteoSwiss) confirmed via personal communication that reproducing measurement results at Jungfraujoch station poses a major difficulty in models as they cannot represent the complex topography and albedo effects around exposed measurement stations adequately. For this reason, the mountain peak stations of Jungfraujoch and Sonnblick will not be taken into account for the following evaluation parts.

From this comparison, the conclusions drawn are:

- Excluding the Jungfraujoch and Sonnblick mountain peak stations, the model agrees within a daily maximum UVI of ±1 to measurement data for 94.9% of the data points.
- Exposed measurement stations at mountain peaks show the largest deviations with an average of -1.43 ± 1.64 as the highest maximum UVI model overestimations compared to measurement stations for the time frame 2025-01-01 to 2025-04-15.

4.8 DWD Operational Comparison

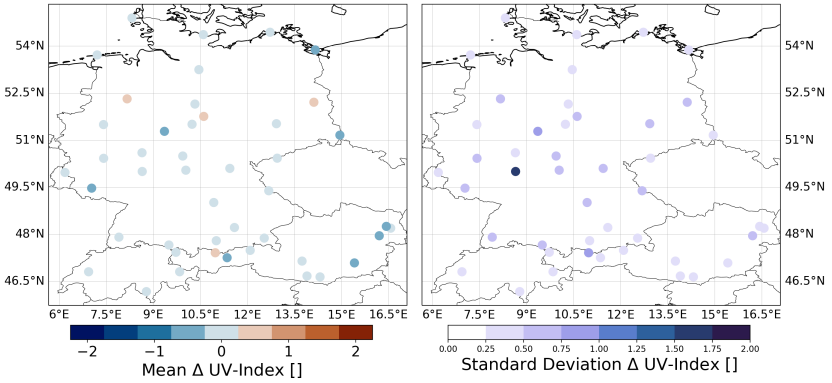

Figure 4.28: Comparison of operational DWD UVI forecast to ground station measurements. The two panels show the temporal mean UVI difference (**left**) and standard deviation (**right**) for 2025-01-01 to 2025-04-15. Negative values mean a UVI overestimation of the DWD forecast.

In order to classify the accuracy of the UVI forecast of the ICON-ART setup of this thesis, the comparison to measurement sites is repeated for the operational UVI forecast of DWD. The operational forecast is based on the setup described by Staiger and Koepke (2005) and provides daily maximum UVI values. It uses meteorological forecasts by ICON in combination with O_3 forecasts by the Royal Netherlands Meteorological Institute (KNMI) and aerosol climatology tables. The UVI and TCO_3 data used for the DWD operational forecast were made available for the time frame 2025-01-01 to 2025-04-15 by Gudrun Laschewski from DWD via personal communication. It is the data product that is also displayed for the current day at *Wetter und Klima - Deutscher Wetterdienst - Leistungen - UV-Gefahrenindex* (2025).

The comparison of mean UVI difference between measurements and model as shown in Section 4.7 is performed with the set of 46 ground stations for the

Data Set	Mean [Δ UVI]	Agreement:	±0	±1	±2
DWD	−0.04 ± 0.60		72.6%	97.9%	99.6%
ICON-ART	0.27 ± 0.77		59.5%	94.9%	98.7%

Table 4.6: Comparison of UVI forecast by operational DWD setup and by ICON-ART setup. The mean and agreements are drawn to 46 measurement sites (excluding the mountain peak stations Jungfraujoch and Sonnblick) for 2025-01-01 to 2025-04-15. The percentages denote the amount of measurement to forecast comparison data points that have the stated UVI difference.

operational DWD forecast. The results are shown in Figure 4.28. All stations have a mean difference between -0.75 and +0.75. The average difference for all considered measurement sites for this time frame is −0.04 ± 0.60. 72.6% of the data have an exact agreement to the measurement stations, 97.9% have an agreement of ±1 and 99.6% have an agreement of ±2.

The comparison of the DWD operational forecast and the ICON-ART forecast is summarized in Table 4.6. Both data sets are using the meteorological output generated by ICON. The setups differ in the prognostic calculation of TCO_3 and the treatment of radiation.

Figure 4.29 shows the mean difference in percent between the DWD operational TCO_3 data used for the UVI forecast and the ICON-ART TCO_3 forecast for the time frame from 2025-01-01 to 2025-04-15. The operational forecast has higher O_3 values for the majority of measurement stations than the ICON-ART forecast, the mean difference over all measurement stations is 1.97 ± 4.51% of TCO_3. Here, a positive number means that the DWD operational forecast has higher TCO_3 values than the ICON-ART setup. As an increase of TCO_3 would mean a decrease of UVI values, this difference cannot explain the higher UVI values of the operational DWD setup. A detailed analysis of the parameters influencing the UVI difference between the operational DWD setup and the ICON-ART model simulations is given after assessing the influence of the model resolution

The conclusions drawn from this comparison are:

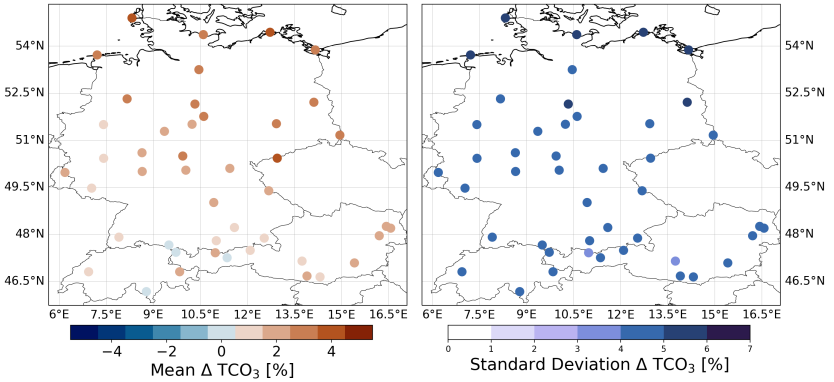

Figure 4.29: 2025-01-01 to 2025-04-15 TCO_3 mean **left** and standard deviation **right** of difference between operational DWD TCO_3 forecast and ICON-ART setup in percent. Positive values mean that the operational DWD setup has higher values than the ICON-ART setup.

- The operational DWD forecast has a closer overall agreement to ground measurement data than the ICON-ART setup.

- For the time frame 2025-01-01 to 2025-04-15, it has an exact agreement to measurement station data for 72.6% of the measurement points in comparison to an exact agreement of 59.5% for the ICON-ART forecast. 97.9% of the operational DWD UVI forecasts match within ±1 to the station data in comparison to 94.9% for the ICON-ART forecast.

4.9 Resolution Analysis

In order to assess the influence of the model resolution on UVI values, the regional R19B7 2 km resolution simulation and the global R3B7 13 km resolution

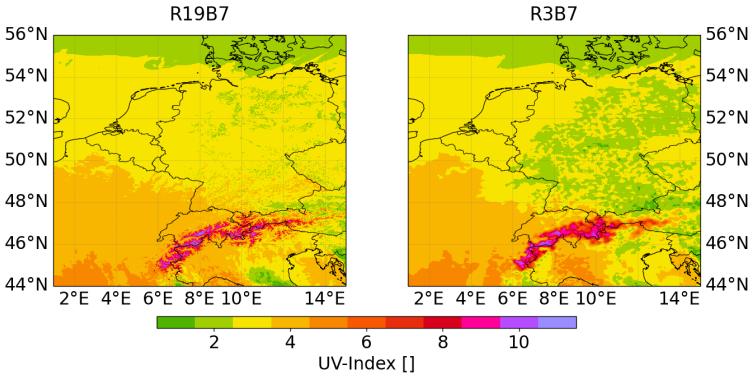

Figure 4.30: Resolution comparison of daily maximum UVI between R19B7 and R3B7 model simulation for 2025-04-01. Looking at the Alps region, the difference in resolution of the two simulation setups can be seen.

simulation were compared for the month of April, 2025. The high resolution R19B7 simulation is nudged hourly with O_3 and meteorological data by the R3B7 simulation on its lateral boundaries. Figure 4.30 showcases the difference in resolution between the two simulations for one day. The differences become evident when looking at the Alps region where steep orography on km-scale occurs.

Figure 4.31 shows the difference between the R19B7 and the R3B7 simulation as mean and standard deviation over the time frame 2025-04-01 to 2025-04-15. The average difference is nonzero only close to the Alps region. This means that for areas without steep terrain, the effect of model resolution between 2 km (R19B7) and 13 km (R3B7) on UVI calculation can be neglected.

For steep terrain, a comparison of the two model simulations with measurement station data described in Section 4.7 is performed by restricting the comparison to measurement stations between 44° and 48° N (Alpine Region). The mean results for each of the measurement stations in this area are listed in Table 4.7. For the R19B7 simulation, the mean difference to measurement stations is -0.15 ± 1.29 and for R3B7 the mean difference to measurement stations is

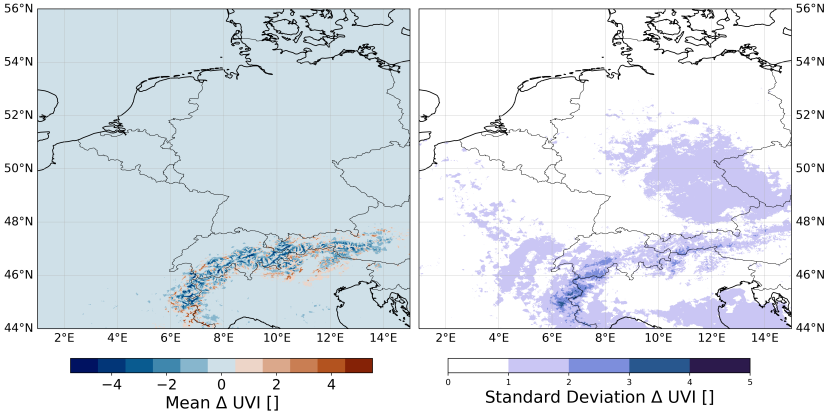

Figure 4.31: Resolution analysis of model data. The plots show the temporal mean (**left**) and standard deviation (**right**) of the difference between the R19B7 2 km and the R3B7 13 km resolution simulation UVI daily maximum values for 2025-04-01 to 2025-04-15. The mean shows no differences differences between the two different resolutions for the majority of the simulated domain, only the region around the Alps shows differences.

-0.15 ± 0.60. While the mean is the same, the higher standard deviation of the R19B7 comparison marks these values as less reliable. This leads to the conclusion that increasing the resolution does not necessarily increase the quality of UVI forecasts.

With the assessment of the influence of model resolution on results, the R3B7 and the R19B7 resolution model simulations are compared to DWD operational UVI values. The difference between DWD operational and ICON-ART UVI forecasts is shown in Figure 4.32 where the data is regarded for each of the UVI influencing parameters. Both resolutions show similar results. Cloud cover and AOD averages mostly stay within a ±0 agreement, the SZA and TCO_3 are almost entirely encompassed within the ±1 agreement. This means that on average, these parameters do not cause differences larger than the given values between operational DWD and ICON-ART forecast.

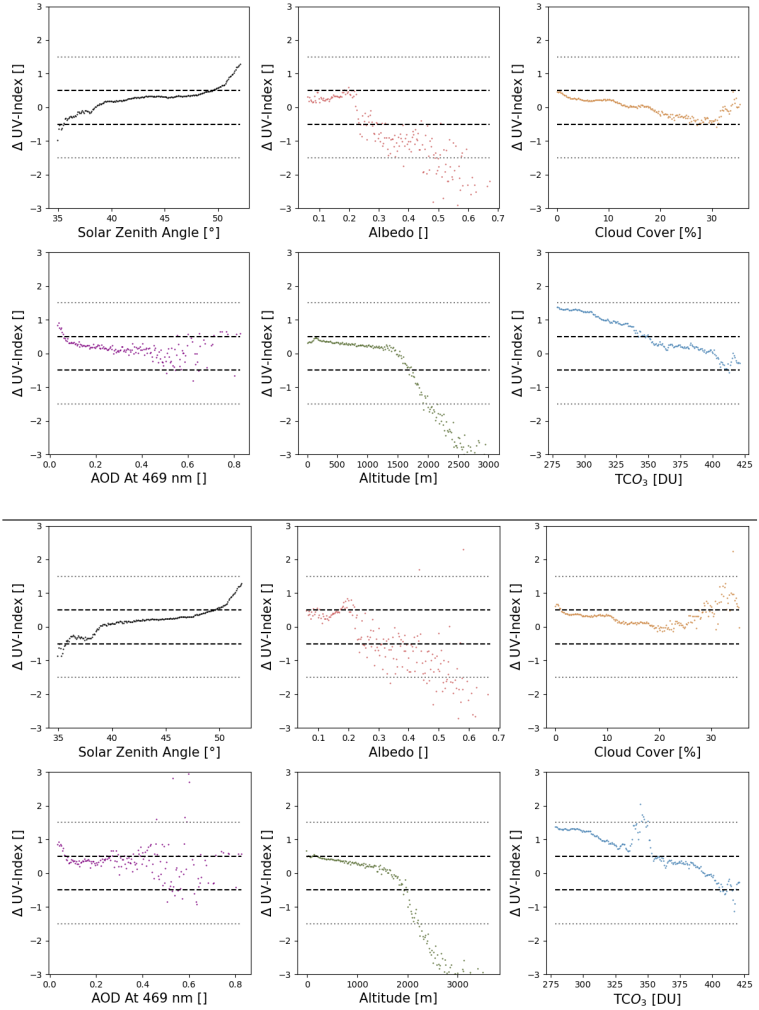

Figure 4.32: Δ UVI (daily maxima, operational DWD to ICON-ART forecast) in ICON-D2 region for April 2025. Positive values mean higher UVI values in the operational DWD forecast. Each panel shows the binned and averaged Δ UVI according to one of the parameters influencing the UVI as shown in Figure 4.26. Albedo and AOD@469 nm were taken from CAMS (*Copernicus Atmosphere Monitoring Service (2021): CAMS global atmospheric composition forecasts.* 2025), the other parameters are from ICON-ART simulations. SZA is the highest daily solar elevation, Cloud cover denotes the highest cloud cover of any model layer. The top two rows show the parameter analysis for the R3B7 simulation, the bottom two rows show it for R19B7. The black dashed lines encompass the area of average agreement within ±0 integer units of UVI, the grey dotted lines encompass the area of a ±1 average agreement.

Location, Height	Measurement UVI []	R19B7 UVI []	R3B7 UVI []
46.18°N, 8.78°E, 366 m	4.1 ± 0.8	4.1 ± 0.9	3.9 ± 1.0
46.65°N, 14.31°E, 4584 m	3.9 ± 0.9	4.0 ± 0.7	4.0 ± 0.6
46.68°N, 13.90°, 1472 m	3.6 ± 1.0	4.1 ± 0.6	3.6 ± 0.9
46.81°N, 6.94°E, 491 m	4.4 ± 0.7	4.1 ± 0.4	4.0 ± 0.4
46.83°N, 9.84°E, 1610 m	5.5 ± 0.5	7.1 ± 0.7	8.1 ± 0.7
47.09°N, 15.41°E, 359 m	3.5 ± 0.9	3.8 ± 0.7	3.7 ± 0.9
47.15°N, 13.74°E, 1127 m	4.3 ± 0.9	4.2 ± 0.5	4.1 ± 0.8
47.26°N, 11.35°E, 576 m	4.2 ± 0.5	4.1 ± 0.4	4.2 ± 0.7
47.43°N, 9.72°E, 415 m	4.3 ± 0.5	4.0 ± 0.3	4.1 ± 0.3
47.49°N, 12.09°E, 520 m	4.2 ± 0.6	3.9 ± 0.6	3.9 ± 0.6
47.42°N,10.98°E, 2656 m	5.8 ± 0.8	5.0 ± 1.5	3.9 ± 0.9
47.96°N, 16.20°E, 269 m	3.0 ± 0.7	3.5 ± 0.8	3.4 ± 0.9

Table 4.7: Mean UVI at Alpine measurement stations of station instruments, R19B7 simulation and R3B7 simulation for 2025-04-01 to 2025-04-15.

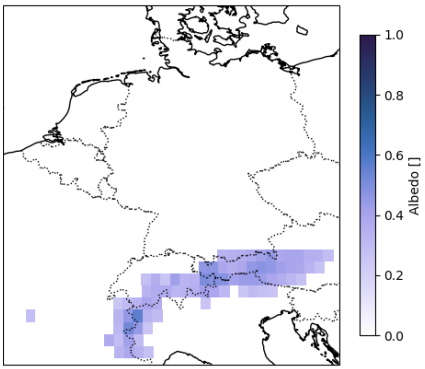

Figure 4.33: Locations in April 2025 with albedo values above 0.25. Albedo values were taken from CAMS Global Atmospheric Composition Forecast, *Copernicus Atmosphere Monitoring Service (2021): CAMS global atmospheric composition forecasts.* (2025)

For locations with albedo values above ≈ 0.25, ICON-ART increasingly overestimates UVI values in comparison to the operational forecast. For the time frame in April, albedos >0.25 only occur in the Alps region, as can be seen in Figure 4.33. The same overestimation of ICON-ART UVI forecasts happens for

locations with altitudes above ≈ 1500 m. This means that for mountainous areas, the differences between operational DWD and ICON-ART forecast become most prominent.

The conclusions drawn from this comparison are:

- Increasing the resolution from 13 km to 2 km does not necessarily increase the quality of UVI forecasts.
- With respect to UVI forecasts, changing the resolution of model simulations mostly affects mountainous areas. For less structured regions, the differences are small.
- Revisiting the comparison to operational UVI forecasts by DWD and analyzing the differences for each UVI influencing parameter, the 13km resolution and 2km resolution simulations both show the largest differences for albedo values above 0.25 and altitudes above 1500 m. Both occur almost exclusively in the Alps region that was encompassed in both modeled regions.

5 Summary and Outlook

The aim of this thesis was to design a way to reliably forecast atmospheric ozone concentrations and to calculate UV-Index (UVI) values by only using the modeling framework ICON (ICOsahedral Nonhydrostatic model) with its module Aerosols and Reactive Trace Gases (ART).

To do so, the LINearized OZone scheme (LINOZ) and the radiation calculation scheme Cloud-J that are part of the module ART were adapted to provide surface irradiances in the wavelength area from 280 to 400 nm. The climatological reference table used in the ozone scheme LINOZ was modified to contain the correct amounts of Very-Short-Lived Substances (VSLS) and stratospheric halogen concentrations that affect stratospheric ozone. LINOZ was also configured to account for heterogeneous polar ozone chemistry.

Cloud-J was adapted to the defined wavelength of the UV-Index. As the scheme was originally designed to calculate actinic flux values for photolysis calculations, it was also modified to calculate irradiances that are required for the UVI calculation. For the required wavelengths in the UV range, the adapted version now has 8 discrete wavelength intervals for which UV radiation is calculated separately and then combined in post-processing to UVI values.

The ozone and UVI forecasts were then validated against satellite data, ozone sonde data, aircraft measurements, ground station measurements and finally compared to the operational UVI forecast provided by Deutscher Wetterdienst (DWD).

For ozone, the comparisons to satellite measurements show agreement in shape of Total Column ozone (TCO_3) on a synoptic scale. The model overestimates TCO_3 values by approximately 5% in the northern hemisphere. The comparison to ozone sonde height profiles shows over-estimations by the model in the lower stratosphere region of 12-18 km height that can explain this difference. Comparisons to aircraft measurements below this height show a close agreement. Simulated polar TCO_3 shows the most prominent differences to measurement data up to 10% difference. The TCO_3 comparisons with satellite data were also included in the recent ICON-ART overview paper by Hoshyaripour et al. (2025).

Validating modeled UVI values against CERES satellite data displays an agreement of dynamical structures on synoptic scales. The average difference between simulated and measured UVI values over a time frame of five months is ±1.

The analysis of the parameters that influence the UVI show a clear dependency of UVI values for altitude, Solar Zenith Angle (SZA), TCO_3 and cloud cover. For albedo and Aerosol Optical Depth (AOD), the dependencies are less clear. The variabilities on UVI values that are introduced by the parameters are largest for the SZA with 9.2 ± 1.9, followed by TCO_3 with 4.9 ± 1.0, cloud cover with 4.7 ± 2.1, AOD with 4.1 ± 2.9, surface albedo with 3.3 ± 2.9 and altitude with 2.5 ± 2.5. Due to the large error margins, repeating this analysis for other time frames would be desirable.

The parameter analysis shows that replacing any of the UVI influencing quantities with pre-calculated values limits the UVI forecasting capabilities of the setup. This is also true for the setup presented in this thesis that used climatological albedo and AOD tables.

The comparison to UVI ground station measurements in the time frame from 2025-01-01 to 2025-04-15 shows that for the modeled forecast, 59.5% of the data agreed exactly to integer rounded UVI measurement values and 94.9% agreed within ±1. Repeating the same comparison for the operational DWD UVI

forecast, the exact agreement to measurement stations is 72% and 97.9% of the data are within a ±1 range. While conducting the comparison to the operational UVI forecast, it should be noted that the calculation method presented in this thesis contains no model bias corrections and was not derived from an ensemble forecast but only from one deterministic simulation. Performing these two additional steps likely will improve the quality of the UVI forecast.

In order to assess the difference in forecast accuracy between the ICON-ART UVI forecast and the DWD operational forecast, a resolution analysis of the model simulation was conducted. It showed no improvement of accuracy in comparison to measurement stations when changing from 13 km to 2 km model resolution. The comparison between UVI data from the operational DWD forecast and modeled values by ICON-ART is repeated for the two model resolutions and separated by UVI influencing parameters. The analysis shows that for albedo values above 0.25 and altitudes above 1500 m, the ICON-ART setup overestimates UVI values in comparison to the operational DWD forecast, which was also seen in measurement station comparisons. For all other atmospheric conditions and locations, the differences between model and measurement stayed almost entirely in a ±2 range.

With respect to the recent increase of machine learning applications, the high computational cost of the UV radiation calculation shown in this thesis raises the question whether the radiation calculation could be replaced by a machine learned parametrization. First steps towards this direction were undertaken during this work using a multi-linear Ridge Regression setup. For this, all data including the UVI were taken from *Copernicus Atmosphere Monitoring Service (2021): CAMS global atmospheric composition forecasts.* (2025). The results showed a strong potential of machine learning methods for UVI forecasting. Changing to more complex, nonlinear methods could increase the forecast accuracy of machine learning methods towards the level of the ICON-ART or the operational forecast while maintaining a low operational computational cost and not relying on external input data. For this, the UVI calculation method and the parameter variabilities presented in this thesis can be used in the training

process of such a setup. The prognostic ozone scheme presented in this thesis can then be used to generate the necessary data for UVI forecasting.

Bibliography

Andreas Engel and Björn-Martin Sinnhuber. 2025. *ASCCI – HALO.* https://halo-research.de/sience/previous-missions/ascci/.

Arnold, Melina, Esther de Vries, David C. Whiteman, Ahmedin Jemal, Freddie Bray, Donald Maxwell Parkin, and Isabelle Soerjomataram. 2018. "Global burden of cutaneous melanoma attributable to ultraviolet radiation in 2012." *International Journal of Cancer* 143, no. 6 (September): 1305–1314. ISSN: 10970215. https://doi.org/10.1002/ijc.31527.

Bianz, Huisheng, and Michael J. Prather. 2002. "Fast-J2: Accurate simulation of stratospheric photolysis in global chemical models." *Journal of Atmospheric Chemistry* 41 (3): 281–296. ISSN: 01677764. https://doi.org/10.1023/A:1014980619462.

Bohren, Craig F., and Eugene E. Clothiaux. 2006. *Fundamentals of Atmospheric Radiation.* Wiley, January. ISBN: 9783527405039. https://doi.org/10.1002/9783527618620.

Brasseur, Guy., and Susan. Solomon. 2005. *Aeronomy of the middle atmosphere : chemistry and physics of the stratosphere and mesosphere.* 644. Springer. ISBN: 1402032846.

Brewer, A. W. 1949. "Evidence for a world circulation provided by the measurements of helium and water vapour distribution in the stratosphere." *Quarterly Journal of the Royal Meteorological Society* 75, no. 326 (October): 351–363. ISSN: 1477-870X. https://doi.org/10.1002/QJ.49707532603. https://onlinelibrary.wiley.com/doi/full/10.1002/qj.49707532603%20https://onlinelibrary.wiley.com/doi/abs/10.1002/qj.49707532603%20https://rmets.onlinelibrary.wiley.com/doi/10.1002/qj.49707532603.

Burkholder, J B, S P Sander, J P D Abbatt, J R Barker, C Cappa, J D Crounse, T S Dibble, et al. 2020. "Chemical Kinetics and Photochemical Data for Use in Atmospheric Studies Evaluation Number 19 NASA Panel for Data Evaluation."

Butchart, Neal. 2014. "The Brewer-Dobson circulation." *Reviews of Geophysics* 52, no. 2 (June): 157–184. ISSN: 8755-1209. https://doi.org/10.1002/2013RG000448.

Chance, K., and R. L. Kurucz. 2010. "An improved high-resolution solar reference spectrum for earth's atmosphere measurements in the ultraviolet, visible, and near infrared." *Journal of Quantitative Spectroscopy and Radiative Transfer* 111, no. 9 (June): 1289–1295. ISSN: 00224073. https://doi.org/10.1016/j.jqsrt.2010.01.036.

Chatzopoulou, Anthi, K. Tourpali, A. F. Bais, and P. Braesicke. 2025. "Twenty-first century surface UV radiation changes deduced from CMIP6 models. Part II: effects on UV index and plant growth weighted irradiance." *Photochemical and Photobiological Sciences* 24, no. 1 (January): 113–130. ISSN: 14749092. https://doi.org/10.1007/S43630-024-00676-6/FIGURES/7. https://link.springer.com/article/10.1007/s43630-024-00676-6.

Chipperfield, Martyn P. 2022. "Scientific Assessment of Ozone Depletion: 2022. CHAPTER 4 Polar StratoSPheric ozone: PaSt, PreSent, and Future."

Cloudy and Clear Sky Turbid UV Index and Dose Forecast: https://kunden.dwd.de/uvi/index.jsp. 2025.

Copernicus Atmosphere Monitoring Service (2021): CAMS global atmospheric composition forecasts. 2025. https://doi.org/10.24381/04a0b097.

Data access - WOUDC - World Ozone and Ultraviolet Radiation Data Centre. 2025. https://woudc.org/en/data/data-access/.

Deutscher Wetterdienst - Tägliche Vorhersagen des UV Index. https://kunden.dwd.de/uvi_de/index.jsp.

Dobson, Gordon Miller Bourne. 1956. "Origin and distribution of the polyatomic molecules in the atmosphere." *Proceedings of the Royal Society of London. A. Mathematical and Physical Sciences* 236, no. 1205 (August): 187–193. ISSN: 0080-4630. https://doi.org/10.1098/RSPA.1956.0127. https://dx.doi.org/10.1098/rspa.1956.0127.

Dobson, Gordon Miller Bourne, and D. N. Harrison. 1926. "Measurements of the amount of ozone in the earth's atmosphere and its relation to other geophysical conditions." *Proceedings of the Royal Society of London. Series A, Containing Papers of a Mathematical and Physical Character* 110, no. 756 (April): 660–693. ISSN: 0950-1207. https://doi.org/10.1098/RSPA.1926.0040. https://dx.doi.org/10.1098/rspa.1926.0040.

Doelling, David R., Moguo Sun, Le Trang Nguyen, Michele L. Nordeen, Conor O. Haney, Dennis F. Keyes, and Pamela E. Mlynczak. 2016. "Advances in Geostationary-Derived Longwave Fluxes for the CERES Synoptic (SYN1deg) Product." *Journal of Atmospheric and Oceanic Technology* 33, no. 3 (March): 503–521. ISSN: 0739-0572. https://doi.org/10.1175/JTECH-D-15-0147.1.

Drdla, K. 2012. "Temperature thresholds for chlorine activation and ozone loss in the polar stratosphere." 30:1055–1073. https://doi.org/10.5194/angeo-30-1055-2012. www.ann-geophys.net/30/1055/2012/.

Eyring, Veronika, Sandrine Bony, Gerald A. Meehl, Catherine A. Senior, Bjorn Stevens, Ronald J. Stouffer, and Karl E. Taylor. 2016. "Overview of the Coupled Model Intercomparison Project Phase 6 (CMIP6) experimental design and organization." *Geoscientific Model Development* 9, no. 5 (May): 1937–1958. ISSN: 19919603. https://doi.org/10.5194/GMD-9-1937-2016.

FAIROmeta · GitLab. 2025. https://gitlab.kit.edu/FObersteiner/FAIROmeta/-/blob/main/science/FAIRO_Description.md.

Fligge, M, S K Solanki, and J Beer. 1999. "Determination of solar cycle length variations using the continuous wavelet transform." *Astron. Astrophys* 346:313–321.

Flury, T, D L Wu, and W G Read. 2012. "Atmospheric Chemistry and Physics Discussions Variability of the Brewer-Dobson circulation's meridional and vertical branch using Aura/MLS water vapor." *Atmos. Chem. Phys. Discuss* 12:21291–21320. https://doi.org/10.5194/acpd-12-21291-2012. www.atmos-chem-phys-discuss.net/12/21291/2012/.

Gathen, Peter von der, Rigel Kivi, Ingo Wohltmann, Ross J. Salawitch, and Markus Rex. 2021. "Climate change favours large seasonal loss of Arctic ozone." *Nature Communications* 12, no. 1 (December): 3886. ISSN: 20411723. https://doi.org/10.1038/S41467-021-24089-6. https://pmc.ncbi.nlm.nih.gov/articles/PMC8222337/.

GEOPORTAL | Bundesamt für Strahlenschutz. 2025. https://www.imis.bfs.de/geoportal/.

Goody, Richard M.. 1996. *Principles of atmospheric physics and chemistry.* 324. Oxford University Press. ISBN: 0195093623.

Hahn, David. 2004. "Light Scattering Theory" (November).

Hogan, Robin J., and Alessio Bozzo. 2018. "A Flexible and Efficient Radiation Scheme for the ECMWF Model." *Journal of Advances in Modeling Earth Systems* 10, no. 8 (August): 1990–2008. ISSN: 19422466. https://doi.org/10.1029/2018MS001364.

Hogan, Robin J., and Marco Matricardi. 2022. "A Tool for Generating Fast k-Distribution Gas-Optics Models for Weather and Climate Applications." *Journal of Advances in Modeling Earth Systems* 14, no. 10 (October). ISSN: 19422466. https://doi.org/10.1029/2022MS003033.

Hoshyaripour, Gholam Ali, Andreas Baer, Sascha Bierbauer, Julia Bruckert, Dominik Brunner, Jochen Foerstner, Arash Hamzehloo, et al. 2025. "The Atmospheric Composition Component of the ICON modeling framework: ICON-ART version 2025.04." *EGUsphere* (September): 1–54. https://doi.org/10.5194/EGUSPHERE-2025-3400. https://egusphere.copernicus.org/preprints/2025/egusphere-2025-3400/.

Hossaini, Ryan, Elliot Atlas, Sandip S. Dhomse, Martyn P. Chipperfield, Peter F. Bernath, Anton M. Fernando, Jens Mühle, et al. 2019. "Recent Trends in Stratospheric Chlorine From Very Short-Lived Substances." *Journal of Geophysical Research: Atmospheres* 124, no. 4 (February): 2318–2335. ISSN: 21698996. https://doi.org/10.1029/2018JD029400.

Hsu, Juno, and Michael J. Prather. 2010. "Global long-lived chemical modes excited in a 3-D chemistry transport model: Stratospheric N2O, NOy, O3 and CH 4 chemistry." *Geophysical Research Letters* 37, no. 7 (April). ISSN: 00948276. https://doi.org/10.1029/2009GL042243.

Hsu, Juno, Michael J. Prather, Philip Cameron-Smith, Alex Veidenbaum, and Alex Nicolau. 2017. "A radiative transfer module for calculating photolysis rates and solar heating in climate models: Solar-J v7.5." *Geoscientific Model Development* 10, no. 7 (July): 2525–2545. ISSN: 19919603. https://doi.org/10.5194/gmd-10-2525-2017.

Instruments – CERES. 2025. https://ceres.larc.nasa.gov/instruments/.

Karagodin-Doyennel, Arseniy, Eugene Rozanov, Timofei Sukhodolov, Tatiana Egorova, Jan Sedlacek, and Thomas Peter. 2023. "The future ozone trends in changing climate simulated with SOCOLv4." *Atmospheric Chemistry and Physics* 23, no. 8 (April): 4801–4817. ISSN: 16807324. https://doi.org/10.5194/ACP-23-4801-2023.

Kroon, M., J. F. De Haan, J. P. Veefkind, L. Froidevaux, R. Wang, R. Kivi, and J. J. Hakkarainen. 2011. "Validation of operational ozone profiles from the Ozone Monitoring Instrument." *Journal of Geophysical Research: Atmospheres* 116, no. D18 (September): 18305. ISSN: 2156-2202. https://doi.org/10.1029/2010JD015100. https://onlinelibrary.wiley.com/doi/full/10.1029/2010JD015100%20https://onlinelibrary.wiley.com/doi/abs/10.1029/2010JD015100%20https://agupubs.onlinelibrary.wiley.com/doi/10.1029/2010JD015100.

Langematz, Ulrike. 2018. "Future ozone in a changing climate." *Comptes Rendus Geoscience* 350, no. 7 (November): 403–409. ISSN: 1631-0713. https://doi.org/10.1016/J.CRTE.2018.06.015.

Laube, Johannes C. 2022. "Scientific Assessment of Ozone Depletion: 2022. Chapter 1: Update on ozone-depleting SUbStanceS (odSS) and other gaSeS of intereSt to the Montreal protocol."

Lavy, Léo, Peter Bernath, Michael Lecours, and Dylan English. 2024. "Antarctic polar stratospheric cloud composition as observed by ACE, CALIPSO and MIPAS." *Journal of Quantitative Spectroscopy and Radiative Transfer* 324 (September): 109061. ISSN: 0022-4073. https://doi.org/10.1016/J.JQSRT.2024.109061.

Liou, Kuo-Nan. 2002. *An introduction to atmospheric radiation.* 583. Academic Press. ISBN: 0124514510.

Liu, J, D W Tarasick, V E Fioletov, C Mclinden, T Zhao, S Gong, C Sioris, J J Jin, G Liu, and O Moeini. 2013. "Atmospheric Chemistry and Physics A global ozone climatology from ozone soundings via trajectory mapping: a stratospheric perspective." *Atmos. Chem. Phys* 13:11441–11464. https://doi.org/10.5194/acp-13-11441-2013. www.atmos-chem-phys.net/13/11441/2013/.

Loeb, N. G., W. Su, D. R. Doelling, T. Wong, P. Minnis, S. Thomas, and W. F. Miller. 2018. "Earth's Top-of-Atmosphere Radiation Budget." *Comprehensive Remote Sensing* 1-9 (January): 67–84. https://doi.org/10.1016/B978-0-12-409548-9.10367-7.

McLinden, C. A., S. C. Olsen, B. Hannegan, O. Wild, M. J. Prather, and J. Sundet. 2000. "Stratospheric ozone in 3-D models: A simple chemistry and the cross-tropopause flux." *Journal of Geophysical Research: Atmospheres* 105, no. D11 (June): 14653–14665. ISSN: 2156-2202. https://doi.org/10.1029/2000JD900124. https://onlinelibrary.wiley.com/doi/full/10.1029/2000JD900124%20https://onlinelibrary.wiley.com/doi/abs/10.1029/2000JD900124%20https://agupubs.onlinelibrary.wiley.com/doi/10.1029/2000JD900124.

Meftah, M., L. Damé, D. Bolsée, A. Hauchecorne, N. Pereira, D. Sluse, G. Cessateur, et al. 2018. "SOLAR-ISS: A new reference spectrum based on SOLAR/SOLSPEC observations." *Astronomy and Astrophysics* 611 (March). ISSN: 14320746. https://doi.org/10.1051/0004-6361/201731316.

Mishra, Kshiti, Cecilia Stanghellini, and Silke Hemming. 2023. "Technology and Materials for Passive Manipulation of the Solar Spectrum in Greenhouses." *Advanced Sustainable Systems* 7, no. 5 (May). ISSN: 23667486. https://doi.org/10.1002/ADSU.202200503. https://www.researchgate.net/publication/369340531_Technology_and_Materials_for_Passive_Manipulation_of_the_Solar_Spectrum_in_Greenhouses.

"Montreal Protocol on Substances that Deplete the Ozone Layer." 1987 (September).

NASA Ozone Watch: Latest status of ozone. 2025. https://ozonewatch.gsfc.nasa.gov/.

NDACC - NASA LaRC. 2025. https://www-air.larc.nasa.gov/missions/ndacc/data.html#.

Obersteiner, Florian. 2025. "FAIROmeta," https://doi.org/10.5281/ZENODO.15863569. https://zenodo.org/records/15863569.

Otterman, J. 1977. "Monitoring surface albedo change with Landsat." *Geophysical Research Letters* 4, no. 10 (October): 441–444. ISSN: 0094-8276. https://doi.org/10.1029/GL004i010p00441.

Parkin, D. M., D. Mesher, and P. Sasieni. 2011. "Cancers attributable to solar (ultraviolet) radiation exposure in the UK in 2010." *British Journal of Cancer* 105 (December): S66–S69. ISSN: 15321827. https://doi.org/10.1038/bjc.2011.486.

Prather, M. J. 2015. "Photolysis rates in correlated overlapping cloud fields: Cloud-J 7.3c." *Geoscientific Model Development* 8, no. 8 (August): 2587–2595. ISSN: 19919603. https://doi.org/10.5194/gmd-8-2587-2015.

Prill, F, D Reinert, D Rieger, G Zängl, Daniel Rieger, and Florian Prill. 2023. "Working with the ICON Model ICON Tutorial," https://doi.org/10.5676/DWD{_}pub/nwv/icon{_}tutorial2023. www.dwd.de.

Prša, Andrej, Petr Harmanec, Guillermo Torres, Eric Mamajek, Martin Asplund, Nicole Capitaine, Jørgen Christensen-Dalsgaard, et al. 2016. "NOMINAL VALUES FOR SELECTED SOLAR AND PLANETARY QUANTITIES: IAU 2015 RESOLUTION B3*†." *The Astronomical Journal* 152, no. 2 (August): 41. ISSN: 1538-3881. https://doi.org/10.3847/0004-6256/152/2/41. https://iopscience.iop.org/article/10.3847/0004-6256/152/2/41%20https://iopscience.iop.org/article/10.3847/0004-6256/152/2/41/meta.

Rehfuess, Eva. 2002. *Global solar UV index : a practical guide.* 28. World Health Organization. ISBN: 9241590076.

Report of the WMO-WHO Meeting of Experts on Standardization of UV Indices and their Dissemination to the Public. 1997. Technical report.

Report of the WMO-WHO Meeting of Experts on Standardization of UV Indices and their Dissemination to the Public. https://library.wmo.int/records/item/39882-report-of-the-wmo-who-meeting-of-experts-on-standardization-of-uv-indices-and-their-dissemination-to-the-public.

Rieger, Daniel. 2019. "ecRad in ICON Implementation Overview Issue 004 Reports on ICON," ISSN: 2628-4898. https://doi.org/10.5676/DWD. www.dwd.de.

Riihelä, Aku, Emmihenna Jääskeläinen, and Viivi Kallio-Myers. 2024. "Four decades of global surface albedo estimates in the third edition of the CM SAF cLoud, Albedo and surface Radiation (CLARA) climate data record." *Earth System Science Data* 16, no. 2 (February): 1007–1028. ISSN: 18663516. https://doi.org/10.5194/ESSD-16-1007-2024.

Roedel, Walter. 2000. *Physik unserer Umwelt: Die Atmosphäre.* https://doi.org/10.1007/978-3-662-09325-2.

Sadeq, Mohammed Ahmed, Mohamed Hady Ashry, Reem Mohammed Farouk Ghorab, and Abdelrahman Yousry Afify. 2023. "Causes of death among patients with cutaneous melanoma: a US population-based study." *Scientific Reports 2023 13:1* 13, no. 1 (June): 1–11. ISSN: 2045-2322. https://doi.org/10.1038/s41598-023-37333-4. https://www.nature.com/articles/s41598-023-37333-4.

Sinnhuber, Björn Martin, and Stefanie Meul. 2015. "Simulating the impact of emissions of brominated very short lived substances on past stratospheric ozone trends." *Geophysical Research Letters* 42, no. 7 (April): 2449–2456. ISSN: 19448007. https://doi.org/10.1002/2014GL062975.

Sinnhuber, Björn Martin, Mark Weber, Abraham Amankwah, and John P. Burrows. 2003. "Total ozone during the unusual Antarctic winter of 2002." *Geophysical Research Letters* 30, no. 11 (June). ISSN: 1944-8007. https://doi.org/10.1029/2002GL016798. https://onlinelibrary.wiley.com/doi/full/10.1029/2002GL016798%20https://onlinelibrary.wiley.com/doi/abs/10.1029/2002GL016798%20https://agupubs.onlinelibrary.wiley.com/doi/10.1029/2002GL016798.

Solanki, Sami K, Natalie A Krivova, and Joanna D Haigh. 2013. "Solar Irradiance Variability and Climate," https://doi.org/10.1146/annurev-astro-082812-141007. www.annualreviews.org.

Staiger, Henning, and Peter Koepke. 2005. "UV index forecasting on a global scale." *Meteorologische Zeitschrift* 14, no. 2 (April): 259–270. ISSN: 09412948. https://doi.org/10.1127/0941-2948/2005/0029.

Su, Wenying, Thomas P. Charlock, and Fred G. Rose. 2005. "Deriving surface ultraviolet radiation from CERES surface and atmospheric radiation budget: Methodology." *Journal of Geophysical Research: Atmospheres* 110, no. D14 (July): 1–17. ISSN: 2156-2202. https://doi.org/10.1029/2005JD005794. https://onlinelibrary.wiley.com/doi/full/10.1029/2005JD005794%20https://onlinelibrary.wiley.com/doi/abs/10.1029/2005JD005794%20https://agupubs.onlinelibrary.wiley.com/doi/10.1029/2005JD005794.

Taylor, Hugh R., Sheila K. West, Frank S. Rosenthal, Beatriz Muñoz, Henry S. Newland, Helen Abbey, and Edward A. Emmett. 1988. "Effect of ultraviolet radiation on cataract formation." *The New England journal of medicine* 319, no. 22 (December): 1429–1433. ISSN: 0028-4793. https://doi.org/10.1056/NEJM198812013192201. https://pubmed.ncbi.nlm.nih.gov/3185661/.

Tselioudis, George, William B. Rossow, Frida Bender, Lazaros Oreopoulos, and Jasmine Remillard. 2024. "Oceanic cloud trends during the satellite era and their radiative signatures." *Climate Dynamics* 62, no. 9 (September): 9319–9332. ISSN: 14320894. https://doi.org/10.1007/S00382-024-07396-8/FIGURES/8. https://link.springer.com/article/10.1007/s00382-024-07396-8.

Vuilleumier, Laurent, Todd Harris, Athanasios Nenes, Claudine Backes, and David Vernez. 2021. "Developing a UV climatology for public health purposes using satellite data." *Environment International* 146 (January): 106177. ISSN: 0160-4120. https://doi.org/10.1016/J.ENVINT.2020.106177.

Wetter und Klima - Deutscher Wetterdienst - Leistungen - UV-Gefahrenindex. 2025. https://www.dwd.de/DE/leistungen/gefahrenindizesuvi/gefahrenindexuvi.html.

Who. 2002. "Global Solar UV Index A Practical Guide." *World Health,* 18.

WHO: Ultraviolet radiation. 2025. https://www.who.int/news-room/fact-sheets/detail/ultraviolet-radiation.

Wielicki, Bruce A., Bruce R. Barkstrom, Edwin F. Harrison, Robert B. Lee, G. Louis Smith, and John E. Cooper. 1996. "Clouds and the Earth's Radiant Energy System (CERES): An Earth Observing System Experiment." *Bulletin of the American Meteorological Society* 77, no. 5 (May): 853–868. ISSN: 0003-0007. https://doi.org/10.1175/1520-0477(1996)077<0853:CATERE>2.0.CO;2.

Zängl, Günther, Daniel Reinert, Pilar Rípodas, and Michael Baldauf. 2015. "The ICON(ICOsahedral Non-hydrostatic) modelling framework of DWDand MPI-M : Description of the non-hydrostatic dynamical core." *Quarterly Journal of the Royal Meteorological Society* 141, no. 687 (January): 563–579. ISSN: 0035-9009. https://doi.org/10.1002/qj.2378.

Zonda. 2025. https://zonda.ethz.ch/.

6 Acknowledgements

Usage of generative Artificial Intelligence (AI): For this thesis, Microsoft Copilot was used to help speed up processing and plotting data presented in this thesis.

Zuerst möchte ich mich bei Peter Braesicke für die Übernahme des Referats und bei Michael Höpfner für die Übernahme des Korreferats bedanken, als Referenten meine Arbeit angenommen zu haben. Peter hat mich im Verlauf meiner Doktorarbeit mit vielen Ratschlägen und Ideen unterstützt. Ich schätze es sehr dass er mir immer auf Augenhöhe begegnet und gleichzeitig viel Wert auf meine Vorschläge legt.

Die größte Unterstützung für meine Doktorarbeit wurde mir durch Roland Ruhnke zuteil. Deine kategorische Hilfsbereitschaft in Kombination mit einem reichhaltigen Wissen und einem (sehr!) scharfen Auge für kleinste Details hat mir diese Doktorarbeit ermöglicht. Es ist absolut nicht selbstverständlich wie entgegenkommend du meine Arbeitsbedingungen um die Geburt meines Sohnes und die darauf folgende Zeit herum angepasst hast! Ich werde unsere Gespräche in sehr guter Erinnerung behalten!

Ein genauso großes Dankeschön möchte ich an Stefan Versick aussprechen. Ich kann hier nahezu alles vom vorherigen Absatz wiederholen, inklusive der Tatsache dass ich mir nicht sicher bin ob ich ohne dich hierhin gekommen wäre (das nahezu habe ich hinzugefügt weil ich weiß dass du ansonsten darauf hinweisen würdest dass du nicht mein Vorgesetzter bist und dementsprechend nicht über meine Arbeitsbedingungen bestimmen kannst). Ich bin mir dessen

vollkommen bewusst wieviel Glück ich mit deiner Unterstützung hatte und habe.

Ich habe mich während der gesamten Doktorarbeit immer sehr glücklich mit meiner Arbeitsgruppe und der MSK-Gruppe geschätzt. Wir hatten immer einen hervorragenden Umgang der reibungslos zwischen wissenschaftlichen Themen und guter Unterhaltung wechselt. Insofern vielen Dank Lena Feld (für die sehr schönen gemeinsamen Konferenzen!), Philipp Dietz, Yiling Ma, Achraf Qor-El-Aine, Stefanie Falk, Khompat Satitkovitchai, Björn-Martin Sinnhuber, Christian Scharun, Miriam Sinnhuber, Andreas Bartenschlager, Monali Borthakur, Alexander Siebelts, Florian Haenel und Alexandra Laeng. Jeder in dieser Aufzählung hat mehr als einmal eine gute Idee für meine Arbeit beigesteuert.

Ich bedanke mich bei den Korrektoren dieser Arbeit, Roland Ruhnke, Stefan Versick, Lena Feld, Philipp Dietz, Marvin Knapp, Tom Wickenhäuser, Paul Warkentin, Tobias Kneuer, Maximiliane Hanft und Nicole Büttner für eure Bereitschaft, diese Arbeit durchzulesen.

Vielen Dank an meine Eltern Michael Hanft und Monika Bandorf-Hanft dafür dass ihr mich mein Leben lang begleitet und unterstützt habt. Ich wusste immer dass ich durch euch einen festen Halt habe.

Ich bedanke mich bei Samuel Hanft dafür dass er existiert und damit mir und seiner Mutter unendliche Freude bereitet. Und zuletzt danke ich dir, Nicole, für das Leben mit dir.